THE CONTROL OF INTERIOR CABIN NOISE DUE TO A TURBULENT BOUNDARY LAYER NOISE EXCITATION USING SMART FOAM ELEMENTS

by
Jason R. Griffin

Thesis submitted to the Faculty of the
Virginia Polytechnic Institute and State University
in partial fulfillment of the requirements for the degree of

Masters of Science
in
Mechanical Engineering

Dr. Chris R. Fuller, Chairman
Dr. Ricardo A. Burdisso
Dr. Martin E. Johnson

May 2006
Blacksburg, Virginia

Keywords: Smart Foam, Active noise control, Passive noise control, Interior cabin noise, Turbulent Boundary Layer

THE CONTROL OF INTERIOR CABIN NOISE DUE TO A TURBULENT BOUNDARY LAYER NOISE EXCITATION USING SMART FOAM ELEMENTS

By
Jason R. Griffin
Committee Chairman: Chris R. Fuller, Mechanical Engineering

(ABSTRACT)

In this work, the potential for a smart foam actuator in controlling interior cabin noise due to a turbulent boundary layer excitation has been experimentally demonstrated. A smart foam actuator is a device comprised of sound absorbing foam with an embedded distributed piezoelectric layer (PVDF) designed to operate over a broad range of frequencies. The acoustic foam acts as a passive absorber and targets the high frequency content, while the PVDF serves as the active component and is used to overcome the limitations of the acoustic foam at low frequencies. The fuselage skin of an aircraft was represented by an experimental test panel in an anechoic box mounted to the side of a wind tunnel. The rig was used to simulate turbulent boundary layer noise transmission into and aircraft cabin. An active noise control (ANC) methodology was employed by covering the test panel with the smart foam actuators and driving them to generate a secondary sound field. This secondary sound field, when superimposed with the panel radiation, resulted in a reduction in overall sound in the anechoic box. An adaptive feedforward filtered-x Least-Mean-Squared (LMS) control algorithm was used to drive the smart foam actuators to reduce the sound pressure levels at an array of microphones. Accelerometers measured the response of the test panel and were used as the reference signal for the feedforward algorithm. A detailed summary of the smart foam actuator control performance is presented for two separate low speed wind tunnel facilities with speeds of Mach 0.1 and Mach 0.2 and a single high speed tunnel facility operating at Mach 0.8 and Mach 2.5.

Acknowledgements

I would like to thank my research advisor, Dr. Chris R. Fuller, for giving me the opportunity to explore the field of acoustics and for guiding me throughout the course of my project. I also must thank Dr. Ricardo A. Burdisso and Dr. Marty E. Johnson for serving on my advisory committee. I must express a deep gratitude to Marty for all the effort that he put forth on my behalf. I appreciate the expert guidance he provided when helping me conduct experiments, his patience with my lack of understanding, and his enthusiasm for knowledge, particularly in the field of acoustics.

I am indebted to NASA Langley Research Center for funding this work. I would like to thank especially Dr. Gary Gibbs and Dr. Richard Silcox for their efforts in coordinating various phases of the project.

There are several members of the Vibrations and Acoustics Laboratories team who have assisted me in various ways. Thanks to Dawn Bennett for her patients and effort in assisting me with many administrative tasks. Thanks to Steve Booth and Chad Burchett for helping me build my test rig.

Finally, I would like to express my sincere thanks to my loving wife Denise for her always positive attitude and words of encouragement in her support of my many endeavors.

Table of Contents

List of Figures

List of Tables

Chapter 1

Introduction

Mankind since creation has been obsessed with overcoming the physical limitations of our human bodies to get from one place to another quickly. Automobiles, rail systems, and aircraft are common transportation methods utilized daily to satisfy the perceived need we have for constant relocation. Advances in these technologies now make it possible for individuals to reach almost any destination on earth in a matter of hours and conduct business during travel. Since travel times have become a significant portion of each day for many people, recent focus has been directed on maximizing travel comfort. One such focus has been on controlling the level of background noise present in the interior cabins of both automobiles and aircraft.

Suppression of an aircraft's interior noise can be appreciated by anyone who has spent a long time in continuous flight. Continuous flight subjects both passengers and crew to constant background noise that can result in communication difficulties and fatigue. Although this may only create a level of discomfort to passengers, greater consequences exist should the noise impede a pilot's ability to communicate and control the aircraft with maximum efficiency and attentiveness.

1.1 AIRCRAFT INTERIOR NOISE

Noise generated by air traffic is a significant byproduct of the world's growing air transportation network. Knowing that noise reduction technology is slow to mature, it was necessary to develop a program plan for the future before a critical need for the technology existed. Thus the National Aeronautics and Space Administration (NASA),

Federal Aviation Administration (FAA), and U.S. industry (manufacturers, operators and airport/community planners) have developed joint noise reduction technology programs that have application to virtually all classes of subsonic and supersonic aircraft envisioned to operate far into the 21st century [1]. The Advanced Subsonic Technology (AST) noise reduction program was initiated in 1992 and focused efforts on the development of new technologies for the U.S subsonic aircraft community and their subsequent environmental impact. The AST noise reduction program contained five subprograms, one of which targeted aircraft interior noise reduction. A goal established by the program is to achieve 6 dB overall reduction in cabin and cockpit noise of commercial and general aviation aircraft by the year 2000 with no increase in treatment weight [1]. Technology is also being developed by NASA and industry partners to bring about a High Speed Civil Transport (HSCT) early in the 21st century as part of the High Speed Research (HSR) program. This program proposes the HSCT will be capable of flying at Mach 2.4 with 300 passengers and a range of 6000 miles [1]. The HSCT will also be required to satisfy the same noise criteria established for the subsonic transports.

Aircraft interior cabin noise is a product of several sources dependent upon the form of aircraft. The first of these sources is propeller noise and can be characterized by discrete tones at the fundamental blade passage frequency (BPF) of the engines and their subsequent harmonics. These tonal excitations are usually dominant in the low frequency region (below 400 Hz) and are typically difficult to control with passive treatments, mainly due to the treatment weight required for control of this region. The advent of the jet engine changed the form of acoustic excitation of an aircraft's interior. The airborne transmission of jet noise is mainly associated with aircraft that have wing-mounted engines, and it affects cabin regions aft of the engine exhaust, particularly when the engines are mounted close to the fuselage [2]. This excitation differs from the propeller driven aircraft excitation since it is primarily a broadband excitation. The influence of jet noise was demonstrated in the aft passenger cabin of a Convair 880 aircraft in which the jet noise was the dominant noise source by 4 – 10 dB during climb conditions [3]. Another source of cabin noise is structureborne noise caused by out-of-balance forces within the engines. These forces induce vibrations into the aircraft structure that subsequently radiate acoustic energy into the interior cabin. This problem has prompted

recent efforts due to the large numbers of jet-powered aircraft with engines mounted directly on the rear fuselage wall. The structurally excited noise components of the aircraft occur at the rotating frequencies of the fan and compressor and typically lie in the range of 75 – 200 Hz [2].

The third primary source of cabin noise is due to aerodynamic noise, or more specifically turbulent boundary layer noise. Again the advent of turbojet-powered commercial aircraft with increased flight speeds has caused this cabin noise problem to become the focus of recent effort. Initially, the primary effort was on understanding and characterizing this disturbance. It has been recognized since the 1940's that aerodynamic noise can be a significant noise problem at speeds greater than 200 mph [4] and more recently that aerodynamic noise is a significant contributor to the mid and high frequency cabin sound pressure levels [5]. Flight tests have been conducted as an effort to characterize the turbulent boundary layer pressure field, fuselage vibration, and interior sound pressure levels [6–11]. These tests have shown that the interior acoustic cabin pressure is a function of flow speed due to the coupling that exists between the boundary layer pressure field and the aircraft structure. Wilby *et al.* [11] demonstrated that the flexural waves induced in the fuselage skin panel by the turbulent boundary layer are subsonic when flight speeds are subsonic and low-supersonic, however, at higher supersonic flight speeds the flexural waves become supersonic and therefore more effective acoustic radiators.

1.2 NOISE CONTROL TECHNIQUES

Noise can be defined as any undesirable or disagreeable sound. Unfortunately, the definition of what is and what is not desirable differs between individuals. For example, noise could be the desired end for those staging a rock concert and at the same instance an extreme irritation to a nearby community. However, regardless of what specifically defines the existence of a noise problem, clearly a need for the control of noise exists. The existence of so many noise control problems has prompted substantial effort into the development and implementation of many new and innovative noise control strategies. These control methods are too numerous to list, however, all of them can be categorized into one of three categories: passive control, active control, and active/passive control.

In general, passive noise control methods require no input power to reduce noise and/or vibration but do so through the inherent material and dimensional properties of the device. Typically, passive control approaches are used because they are inexpensive and easy to implement, however, their performance is limited to the mid and high frequency range. This limitation is based on the restraint most systems have for the addition of excess mass and volume, which is necessary for improving the performance of many passive devices.

Advances in digital computer technology have enabled active control methods to emerge as practical alternatives to passive control treatments. Unlike passive treatments, active control methods require additional energy to be introduced into a system through a series of control inputs or secondary sources. These sources are used to create a secondary field that couples with the primary disturbance such that the total system response is minimized or altered as desired. The implementation of active control systems, regardless of the application, consists of several key components: sensors, control actuators, and a control algorithm. In many control systems error sensors are used to provide the controller with an estimate of the behavior (or performance) of the system. If the desired goal of the control system is to reduce vibration, structural transducers (e.g. accelerometers) are often implemented as error sensors, however, the control of radiated sound would usually utilize acoustic transducers (e.g. microphones) as error sensors. The control actuators, typically loudspeakers or force input devices, are used to generate and project a secondary sound field into a system and the control algorithm generates the control signals necessary to minimize the response from the error sensors. In addition, these control algorithms can be adaptive so that a control system adjusts to account for the changes in disturbance characteristics over time.

Many noise problems exist as a result of structural vibrations and, consequently, two primary control approaches have emerged. Active Noise Control (ANC) is the first technique, which focuses effort on the reduction of the radiated sound pressure from a system [12]. This control approach involves the generation of an “anti-sound” field [13] by exciting the acoustic medium with secondary noise sources (typically loud speakers). An alternative to this approach takes advantage of the close coupling between the structural vibration and the radiated sound field and involves applying a mechanical input

directly to the vibrating structure. This methodology is referred to as Active Structural Acoustic Control (ASAC) and was first introduced by Fuller [14,15]. This idea of modifying the vibration characteristics of a system to reduce far-field radiation has prompted investigation into modal restructuring. Modal restructuring is the process of adding secondary inputs such that efficiently radiating modes are suppressed [16,17]. It has been demonstrated that global far-field attenuation can often be achieved with fewer actuators than similar ANC approaches [18,19] and in some cases reduction in radiated sound power can be achieved with an increase in system vibration [20]. Most often active noise control systems are implemented for the control of low frequency noise, since the signal processing speed demands are less and it is within this frequency range where passive approaches typically fail.

Recently, a new form of noise control methodology has immerged that couples both passive and active control strategies into a single hybrid control actuator. This active/passive control strategy relies on the passive component of the actuator to attenuate the high frequency noise content and an embedded active component to overcome the low frequency shortcomings of the passive material. The resulting actuator can therefore operate effectively over a broader range of frequencies than the individual actuator components acting independently.

1.3 CONTROL OF AIRCRAFT INTERIOR NOISE

Aircraft interior noise has been recognized as a potential problem and has been the focus of noise control research since the 1930s [21]. In 1946 it was recognized that airplane designers could not afford to add more sound proofing material to existing designs [4], however, redistribution of existing acoustic treatment or reduction of the noise at the source would be the required for future noise reduction improvements. Various parameters such as cabin configuration, engine speed, and propeller tip clearance were suggested as parameters that could be modified to help control the interior cabin noise.

Much of the early cabin noise research involved passive control methods that introduced acoustic treatments throughout the aircraft [22]. The early analysis of aircraft interior noise relied heavily on architectural acoustic methods, however, it was later realized that these methods were not adequate since the excitation type and resulting

modal response of both the aircraft structure and interior play significant roles [2]. The choice of porous or non-porous materials for use as a trim panel was an example of an early debate that attempted a balance between the transmission loss and absorption properties of the treatment [2].

The achievable attenuation of aircraft interior noise due to the addition of passive noise control treatments is limited due to the restricted mass and volume constraints within an aircraft. Consequently, effort has been focused on active control methods of reducing interior cabin noise due to the various sources of excitation. The majority of the control effort has been focused on the control of engine noise, which propagates itself through two distinct paths. There is an airborne path in which engine noise is transmitted directly through the fuselage walls and a structureborne path that arises from vibrating panels induced by rotating imbalances within the engines. Several summary and review papers have been published on the extensive research that has been conducted on the active control of these two noise sources [2,23,24]. This work will present a few of the more recent efforts.

The control of structureborne noise in an aircraft cabin was demonstrated through research conducted in the Douglas Aircraft Company Fuselage Acoustic Research Facility [1]. These experiments utilized a fully furnished 34 ft. aft section of a DC-9 aircraft as a test cabin. These tests focused on the control of the structureborne noise from pylon-transmitted engine vibrations that excite the fuselage and subsequently radiate acoustic energy into the cabin interior. The vibration inputs were applied as single frequency sine tones at the forward and aft engine mount locations using 50-lb. shakers. Two 25-lb. shakers were positioned as close as possible to the two source shakers and mounted to the fuselage sidewall and to be used as control actuators. Seven microphones were positioned 4 in. above the seat-back height at select locations throughout the cabin interior. In addition, five accelerometers were positioned on the fuselage and used to monitor vibration levels during the experiments. Various parameters were varied and evaluated throughout the experiments including: the frequency of the excitation source, the forward or aft location of the source, the forward or aft location of the control actuators, and the number and type of error sensors used for control. It was concluded that global control of both radiated sound pressure level and

fuselage vibration could be achieved with relatively few control sources. Also, global reduction of the radiated sound pressure levels could be achieved using either microphones or accelerometers as error sensors. The minimum averaged global attenuation in sound pressure level was 4.6 dB when one accelerometer was used as an error sensor whereas the maximum attenuation was 13.3 dB when four microphones were used as error sensors. A suggested challenge for future work was to develop small lightweight actuators that could be easily installed to the fuselage wall to take the place of the heavy shakers used in these experiments.

Fuller *et al.* [26] performed a similar set of experiments in which four actuator arrays, each consisting of four G1195 piezoceramic patches were wired in series, mounted to the aft section of the interior fuselage skin of a Cessna business jet, and used as control actuators. The disturbance was transmitted to the fuselage through the rear engine mount by a mechanical shaker. A multi-channel filtered-x control algorithm was implemented that targeted reduction at four error microphones positioned on the left and right sides of the head rests in the aft most seats of the aircraft. Seven additional microphones were positioned throughout the aircraft to monitor the global nature of the control effect. The frequency of excitation was chosen to be 250 Hz, which corresponded to an acoustic resonance of the interior cabin cavity. The results showed global attenuation at all but a single microphone with attenuations of 20 – 30 dB at the four error sensors. An additional excitation frequency of 195 Hz was chosen, which corresponded to an off-resonance of both the fuselage structure and the acoustic cavity. Attenuation of 2 – 10 dB was observed at the error microphones, however, there was an increased level at all other microphone locations within the cabin. Global attenuation could be achieved for off-resonance frequencies by introducing more actuator arrays and, consequently, more control channels.

Elliott *et al.* [27] performed in-flight experiments to demonstrate the active control of propeller-induced passenger cabin noise in a British Aerospace 748 twin turboprop aircraft. The experiments were conducted under straight and level flight conditions at a cruise altitude of 10,000 ft with a normally pressurized cabin. The engine speed was 14,200 rpm, which, due to engine gearing resulted in a fundamental blade passage frequency (BPF) of 88 Hz. Second and third harmonics occur at 176 Hz and 264

Hz respectively. The passenger cabin of the aircraft was fully trimmed and furnished with the front nine rows of seats and the last three seat rows were removed to make room for experimental equipment. Thirty-two error microphones were positioned to the outboard side of the headrests on the outboard seats and the inboard side of the headrests on the inboard seats approximately 1.1 m above the floor. Eight loudspeakers were positioned on the floor in front of the seats and eight were positioned in the overhead luggage racks. A total of twenty-six different loudspeakers and microphone positions were investigated in these experiments. The controller performance was evaluated by comparing the change in the sum of the pressure squares of the 32 control microphones. Reductions of 13 dB were observed for the fundamental BPF, 9 dB for the second harmonic, and 6 dB for the third harmonic. The attenuation of the second and third harmonic was improved to 12 dB by concentrating the majority of the loudspeakers in the plane of the propellers.

Saab has developed a commercially available active noise control system for the Saab 340 and Saab 2000 propeller driven aircraft [28]. The systems typically are comprised of 24 – 36 loudspeakers used as secondary sources that mount in the overhead locker trim panels and at foot level. An array of 48 – 72 microphones are positioned throughout the interior cabin and used as error sensors. The disturbance is referenced by the controller through synchronization signals taken directly from the propeller shafts. The total weight of the implemented control system is around 70 kg with power consumption approximately equal to 300 Watts. This configuration yields tonal reduction in sound pressure level around 10 dB at the fundamental BPF.

The active control of turbulent boundary layer noise, due to the broadband nature of the excitation, presents a more difficult control problem than the control of tonal engine noise excitation. In addition, it is difficult to obtain a good reference signal for control since turbulent boundary layer noise has such poor spatial correlation. For these reasons, most of the work regarding turbulent boundary layer noise excitation involved its characterization [6–11]. Additional work has been recently conducted to develop analytical models to predict the acceleration response and sound transmission of plates exposed to random acoustic or turbulent boundary layer excitation [29,30]. Graham's model [30] has been extended to more realistically represent the fuselage skin of an

aircraft by adding two dissipative layers [31]. These layers representing the presence of an insulating layer and a trim panel.

The control of broadband interior noise, similar to that induced by turbulent boundary layer flow, was demonstrated in the cockpit of a Cessna Citation III fuselage [32]. The flow noise was simulated by a band-limited random noise excitation (500 – 1000 Hz) produced by three loudspeakers mounted above the crown of the aircraft. The control signal was provided by piezoelectric actuators mounted to the aircraft interior cockpit crown trim panel. Sixteen microphones were used to evaluate global control, several of which were used as error sensors. A 2 dB reduction was achieved over the entire frequency range at the pilot's ear level using a two-input two-output configuration. It was concluded that controller speed was a limiting factor in control performance.

1.4 PREVIOUS WORK ON SMART FOAM

Porous sound-absorbing materials (e.g. acoustic foams) are often used as passive noise control treatments for control of sound propagation and transmission in a large number of applications [33,34]. Bolton *et al.* [35] presented analytical results demonstrating that the absorption properties of a finite-depth porous layer could be enhanced at low frequency by applying an appropriate force to the surface of the layer. It was shown that at any angle of incidence, the solid phase of the porous layer could be forced to match the impedance of a plane wave causing the sound to be completely absorbed. This was demonstrated experimentally by Fuller *et al.* [36] in which an adaptive foam actuator (i.e. Smart Foam) was used to minimize the intensity of a low frequency reflected plane wave. The smart foam device consisted of a thin 28μm Ag metallized PVDF layer embedded in partially reticulated foam. The device was formed into a circular cross section and positioned at one end of a standing wave tube while a speaker source was positioned at the other end of the tube. A spectrum analyzer provided the frequency domain estimates of the reflected wave intensity as well as the driving input signal to the noise source. An error signal was generated using an analog wave deconvolution circuit based on the two-microphone technique outlined by Elliott [37]. This error signal was proportional to the reflected sound and served as the minimization parameter for the filtered-x LMS algorithm used for control. The passive attenuation of the foam alone proved negligible

below 300 Hz, however the active/passive attenuation of the smart foam was 10 dB between 150 and 300 Hz and up to 40 dB at frequencies greater than 600 Hz. This work demonstrated experimentally that adaptive foams are effective in reducing reflected sound energy.

Gentry *et al.* [38] demonstrated that adaptive foam can be effective in reducing the radiated sound power of a vibrating structure. A circular smart foam device was built consisting of a thin 28μm Ag metallized PVDF layer embedded in partially reticulated foam. The smart foam was manufactured to be approximately 2 in. thick and 6 in. in diameter and was mounted directly to the top of a piston. The piston was mounted in a rigid baffle inside an anechoic chamber and excited using a mechanical shaker driven by an external generator. A single error microphone was mounted at a radius of 5 ft. directly perpendicular to the top surface of the piston (i.e. the location of maximum directivity). Although only a single error microphone was used, the sound attenuation was global and monitored using a microphone traverse swept from –90º to 90º. A filtered-x LMS algorithm implemented with a personal computer mounted DSP board was used to determine the control signal necessary to minimize the sound radiation at the error microphone. The ability of smart foam to attenuate noise at both low and high frequencies was demonstrated by the harmonic control of the noise radiating from the piston excited at 290 Hz and 1000 Hz. At the 290 Hz excitation frequency the smart foam provided no passive attenuation, however contributed a global sound reduction of nearly 20 dB. At the 1000 Hz excitation frequency the passive properties of the smart foam contribute more than 10 dB of attenuation while a further 10 dB global reduction was attributed to the active smart foam component. In addition, the smart foam actuators were also used to control broadband piston radiation. In this control case, the same test configuration was used, however, the piston was excited with band-limited random noise between 0 and 1600 Hz. Also, a 15 ms delay was added to the disturbance path to enable the controller time to adapt the control filter coefficients. At frequencies below 350 Hz, where the passive sound absorbing properties of the foam were poor, about 10 dB of global noise attenuation was attributed to the active component of the smart foam. At frequencies above 350 Hz, the passive smart foam component achieved 15 dB attenuation and the active component achieves an additional 10 dB. These experiments demonstrated

that smart foam can successfully modify the resistive radiation impedance of a vibrating source yielding global noise cancellation. The active component (PVDF layer) was able to compensate for the poor sound attenuation characteristics of the acoustic foam at low frequencies thus demonstrating how the active and passive components complement one another.

In later experiments, smart foam actuators were used to minimize the radiation of a multiple degree-of-freedom, clamped, aluminum plate measuring 6.75 x 5.87 x 0.016 in. [39]. The plate was mounted in a rigid baffle within an anechoic chamber and surrounded by a steel baffle meant to simulate the ribbed stiffeners one might find on an aircraft fuselage wall. A piezoelectric ceramic actuator was bonded to the rear surface of the plate and used to excite the plate up to and including the (3,3) mode of the plate. Due to the increased complexity of the radiating source, a multiple input multiple output (MIMO) feedforward filtered-x LMS controller was used with the error signals provided by close proximity microphones located within the nearfield of the actuators. The smart foam actuators were again constructed from a partially reticulated polyurethane foam and measured 3 in. long, 2 in. wide, and 2.25 in. thick. The active layer included an embedded 28μm Ag metallized PVDF layer configured as a half-cylinder with a 2.0 in. diameter. A lightweight rigid wood frame was wrapped around the periphery of the each smart foam module to promote independent controllability of each module and to prevent cross-coupling. A hemispherical frame with a 2 ft. radius and 10 microphones was used to calculate the radiated sound power and compare control cases. Minimization of the radiated sound power of the vibrating plate was first demonstrated at a discrete frequency. The plate was excited at 545 Hz, which corresponds to the (3,1) structural mode of the bare plate. Six independent smart foam control modules were mounted to the plate, each with a corresponding error microphone mounted 1 in. from the surface of the actuator. An internal reference signal was used as input to the 6I6O LMS controller. The active/passive sound reduction at each of the error microphones was an average of 15 dB while an average sound reduction of 10 dB was realized at each of the observation microphones on the hemispherical frame. In addition, 8 dB attenuation in sound power was achieved by both the active and passive smart foam elements yielding a total sound power attenuation of 10 dB. Similarly, control was demonstrated using the same plate

excited with band-limited random noise from 250 – 1600 Hz. The passive properties of the foam contributed approximately 5 dB passive attenuation in radiated sound power from 500 – 1000 Hz. The active component contributed an additional 5 – 15 dB reduction in the same frequency range. Above 1000 Hz, the passive foam contributed about 10 dB sound power reduction.

Control of aircraft interior broadband noise has also been demonstrated using smart foam by Guigou *et al.* [40]. A band-limited random excitation was produced by a loudspeaker mounted outside of a Cessna Citation III fuselage simulating the broadband characteristics of aerodynamic flow noise. The smart foam actuators used in these experiments were constructed from a partially reticulated polyurethane foam and measured 3 in. long, 2 in. wide, and 2 in. thick. The active layer consisted of a 28μm Ag metallized PVDF layer configured as a half-cylinder with a 1.5 in. diameter. Again, the smart foam cells were encased in a thin balsa wood frame for improved radiation efficiency. Four crown panels lined the fuselage interior each comprised of three smart foam cells driven in phase. The four control channels were used to reduce the radiated sound pressure level at four error microphones located at the pilot's ear level (about 7 in. below the cockpit fuselage ribs). A twelve-microphone traverse was used to monitor the global performance of the controller at both ear and shoulder levels. The Cessna fuselage was first excited with a 200 Hz bandwidth from 500 – 700 Hz and the average attenuation for the four error microphones was 15 dB. The global noise levels were also measured with the traverse where the average active attenuation was 12.5 dB in the pilot's ear plane and 10 dB in the pilot's shoulder plane. These results represent an ideal control case since the disturbance signal sent to the speaker was used as an internal reference. Two additional control cases were examined where a more realistic reference was used utilizing a fuselage-mounted accelerometer and a microphone mounted in close proximity to the exterior surface of the fuselage. Using the accelerometer as a reference yielded an average attenuation at the error microphones of 6 dB and an active global attenuation of 6.5 dB at ear level and 5.5 dB at shoulder level. Similarly, the microphone mounted near the fuselage wall yielded an average attenuation of 10 dB at the error microphones and a global active attenuation of 9.0 dB and 7.5 dB at the ear and shoulder levels respectively. In addition, the passive properties of the foam contributed an additional 4 dB of

attenuation. The fuselage was also excited with an 800 Hz bandwidth from 250 – 1050 Hz where the global active/passive attenuation of 7 dB was realized when using the microphone as the reference. These results demonstrated that broadband global noise control is possible in a realistic environment using a practical control methodology.

1.5 ORGANIZATION OF THESIS

It is the intent of this research to demonstrate the potential of an active/passive smart foam technique to control panel radiation due to a turbulent boundary layer noise disturbance. Chapter 2 discusses the principal components and design configuration of a smart foam actuator. The acoustic radiation characteristics are also presented. Chapter 3 sets forth a derivation of the filtered-x LMS feedforward control algorithm used in the experiments. The potential control issues of causality and multiple coherence are also discussed. Chapter 4 summarizes the methodology involved in the simulation of a turbulent boundary layer noise excitation using a wind tunnel. Characterization of the experimental components and test rig is also presented. Three separate wind tunnel test facilities were utilized in conducting experiments to simulate the turbulent boundary layer excitation of an exterior fuselage panel. The three wind tunnels used were located at NASA Langley Research Center, Hampton, Virginia, Virginia Polytechnic Institute and State University (VPI), Blacksburg, Virginia, and Arnold Engineering Development Center (AEDC), Tullahoma, Tennessee. Specifics regarding the individual test facilities as well as the results achieved along with discussion for these tests are presented in Chapter 5. Finally, the thesis concludes in Chapter 6 with a summary of conclusions and potential future work using smart foam.

Chapter 2

Smart Foam Elements

2.1 INTRODUCTION

The goal of this work was to demonstrate the control of turbulent boundary layer noise transmission using smart foam elements. A turbulent boundary layer induces vibration in the fuselage panel, which radiates noise into the interior cabin of an aircraft. Smart foam elements can be positioned on the interior fuselage skin and used as both passive sound absorbers and active sources in an active control system to reduce the cabin noise level. The aviation industry is extremely conscience of the size and weight of elements on an aircraft because of the cost issues involved. For this reason smart foam elements, due to their lightweight and integration of active and passive noise control techniques, have an advantage over conventional speakers that utilize heavy magnets.

A device comprised of a distributed piezoelectric layer and sound absorbing foam has been developed for controlling structural acoustic radiation. The motivation behind combining these two components was to develop a device that will operate over a wide range of frequencies. The acoustic foam acts as a passive noise suppression device and targets primarily the high frequency content, while the piezoelectric actuator serves as the active component and targets the low frequency content. Active control is easier at lower frequencies because the signal processing speed demand is less and fewer actuators and sensors are required. The piezoelectric element works by translating an electrical input signal into a motion that radiates sound away from the surface of the smart foam element. Unlike the traditional ASAC methods that use local actuators to directly modify structural vibration to reduce sound radiation [14-15], smart foam employs a continuous active

layer that decouples the vibration from the radiation field. The combined effects of both the acoustic foam as the passive component and the piezoelectric element as the active component make this a more robust device that will be useful in a greater number of applications. This chapter presents a detailed description of the individual components of smart foam, how they are constructed, and the characterization of smart foam as an actuator.

2.2 ACTIVE COMPONENT

The active component of a smart foam element is the piezoelectric polymer polyvinylidene fluoride (PVDF). Piezoelectricity is Greek for "pressure electricity" and is a characteristic some materials have for generating an electric field when mechanically deformed. Piezoelectric materials are often used as sensing devices where charge output is proportional to the mechanical deformation or strain in the material. These materials, however, can also be used as actuators in which the mechanical behavior of the actuator is controlled by varying the amplitude and phase of an electrical input signal. This motion, in the case of a smart foam element, is used to generate an acoustic signal that is equal in amplitude and 180º out of phase with a disturbance. The combination of the two acoustic signals results in an overall decrease in sound level.

An analysis of the piezoelectric phenomenon seen in a piezo-polymer requires the definition of a few parameters and notation conventions. The mechanical and electrical responses within piezoelectric materials depend on the axis of applied mechanical force or electric field (for anisotropic materials). Figure 2.1 defines a standard numerical classification for the film axes: 1 for length, 2 for width, and 3 for thickness. Two subscripts are typically used when referring to the piezo-coefficients for charge d_{mn} and voltage g_{mn}, but since we are using the PVDF as an actuator, we are most concerned with the piezoelectric coefficient associated with change in length per applied voltage, or d_{mn}. The first subscript (m) refers to the electrical axis and the second subscript (n) refers to the mechanical axis. In the case of piezoelectric film, the electrodes must be mounted to transfer the voltage through the thickness of the film, and for this reason m is always 3 for piezo-film. The mechanical axis subscript can be a 1, 2, or 3 depending on which axis is of interest. Most sensing and actuation is done along the n=1 axis except for high

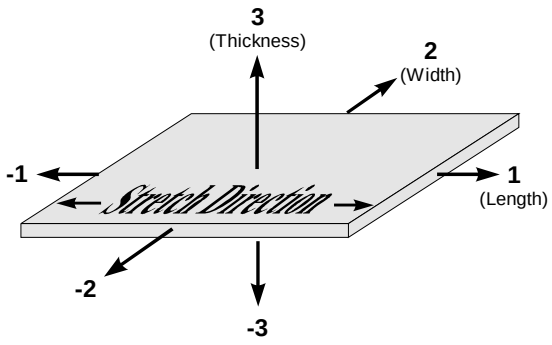

Figure 2.1 Numerical classification of PVDF axes.

ultrasound sensing and actuation in which n=3. Applying a voltage across the film thickness causes the film to change in thickness, length, and width. This unconstrained change in length, width, and thickness induced in the PVDF for an applied voltage can be calculated with the following equations

$$\Delta l = l \cdot d_{31} \cdot V \,, \tag{2.1}$$

$$\Delta w = w \cdot d_{32} \cdot V \,, \tag{2.2}$$

$$\Delta t = t \cdot d_{33} \cdot V \,, \tag{2.3}$$

where Δl is the change in film length, l is the original length of film, V is the applied voltage across the thickness t, and d_{3n} is the piezoelectric coefficient for change in length/volt in the "n" direction [41]. The relationship between input voltage and mechanical deformation is illustrated in figure 2.2(a) where it is shown that a positive voltage polarity causes the piezoelectric film becomes longer, wider, and thinner. The opposite polarity causes the film to contract in length and width and an increase in thickness. This induced deformation is caused by the attraction and repulsion of the internal dipoles of the applied electric field and can be used to generate out of plane motion. Figure 2.2(b) illustrates that applying an alternating current will result in a rapid expansion and contraction of the film or pulsating effect. This motion is analogous to the motion of a speaker cone thus can be used to radiate sound.

PVDF has many advantages that lend itself well for use as the active component in a smart foam element. The film is extremely lightweight and flexible when compared to other piezoelectric materials. This flexibility permits the film to take on almost any imaginable shape allowing it to be customized for each specific application while the low

weight does not alter system characteristics by adding significant mass. A convenience and cost advantage to using the film is that it can be bonded or glued using commercial adhesives. A final advantage for using PVDF as the active element within smart foam is the close match between the acoustic impedance of PVDF and that of air. The closer the acoustic impedance of an actuator is to that of the medium on which it operates (air in this case) the more efficient that source will radiate. The improved efficiency of the actuator will thus require less control energy in its operation. Table 2.1 lists some typical properties of PVDF and compares them with a popular piezoelectric ceramic material [41].

2.3 PASSIVE COMPONENT

The passive component used in the implementation of the smart foam element investigated in this thesis is the porous sound absorbing material partially-reticulated polyurethane foam. Partially-reticulated polyurethane foam is an acoustical grade, open cell, flexible ester based urethane foam designed to give maximum sound absorption per given thickness [42]. Some of the reasons for choosing this particular passive material are that the foam is relatively inexpensive, various sizes are commercially available, and it is easy to form into a desired shape. It should be noted however that the smart foam concept is not limited to partially-reticulated polyurethane foam, but numerous other passive absorbing materials could be used in the fabrication of a smart foam element. Porous sound-absorbing materials are often implemented to reduce sound transmission and radiation in buildings, enclosures, and aircraft. Such materials work to dissipate

Table 2.1 Comparison of piezoelectric material properties.

Property	Units	PVDF Film	PZT
Density	(10^3) kg/m^3	1.78	7.5
Relative Permittivity	$\varepsilon/\varepsilon_0$	12	1200
d_{31} Constant	(10^{-12}) C/N	23	110
g_{31} Constant	(10^{-3}) V·m/N	216	10
k_{31} Constant	% at 1 kHz	12	30
Acoustic Impedance	(10^6) kg/m^2·sec	2.7	30

acoustic energy through friction losses. These losses are associated with the air molecules in the interstices of the porous material that oscillate with the frequency of the incident acoustic wave. A loss of momentum results as the flow changes direction and expands and contracts as it moves through the irregular pores of the foam. These account for most of the energy losses at high frequencies. At low frequencies heat conduction is a source of energy loss. An accompanying change in temperature occurs as the air within the foam undergoes periodic compression and decompression. Fundamentally this is an isothermal process due to the time between half-period oscillations, the large surface-to-volume ratio of the foam, and the high heat conduction of the foam fibers. This heat exchange process is responsible for loss of sound energy [33]. Additionally, the solid phase of the foam dissipates energy by damping vibration in the structure to which it is mounted.

2.4 CONSTRUCTION

As mentioned in the previous section, an electric field applied across the thickness of the thin film PVDF causes its internal dipoles to attract and repulse each other inducing a predominantly in-plane strain within the material. The resulting in-plane motion, with the PVDF arranged horizontally, would be an extremely inefficient radiator of sound since the fundamental requirement for a structure to radiate sound into the far-field is out-of-plane motion (or volume velocity). Since PVDF is extremely flexible, allowing it to take on virtually any shape, it was essential to determine the optimum contour PVDF should have to maximize its far-field radiation efficiency. Gentry-Grace [43] generated a 2-D finite element model of a smart foam element to determine this optimal PVDF configuration. In this work various PVDF contours were examined for multiple boundary conditions applied to the actuator boundaries. Fixed boundary conditions enforce zero displacement on the ends of the PVDF and free boundary conditions enforce no constraints on the ends. The various configurations were compared based on vertical and horizontal motion of the PVDF as well as the radiated sound pressure levels produced. The test setup positioned the smart foam actuator at one end of a rigid duct with an anechoic termination at the opposite end. The optimum smart foam configuration was selected as the configuration that yielded the maximum generated sound pressure

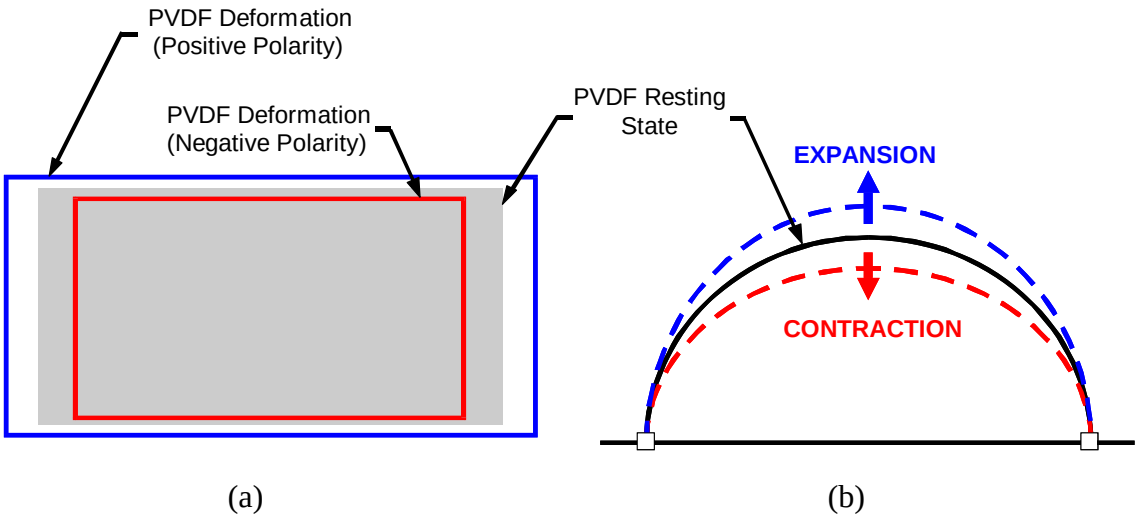

Figure 2.2 (a) Deformation of PVDF. (b) Translation of PVDF into useful motion

levels between 100 Hz and 1000 Hz excited at 300 V_{rms}. This work demonstrated that more vertical displacement could be achieved by increasing the radius of the half-cylinder. A larger radius requires a longer piece of PVDF and thus yields a greater change in length (Δl) for an applied voltage (V) per equation (2.1). C. Liang *et al.* [44] also conducted analytical studies concerning curved PVDF which showed that the acoustic intensity generated by an actuator in the low-frequency region is directly proportional to the radius of the PVDF.

A schematic showing the principal components of a smart foam element and how the PVDF is oriented within the foam is depicted in figure 2.3. As shown, the acoustic foam is shaped to hold the PVDF in the form of a half-cylinder and each side of the PVDF is affixed to the foam using a light application of spray glue. Manufactured PVDF is available in varying sheet sizes with thicknesses of 9μm, 28μm, 52μm, and 110μm and a choice of a carbon or silver ink surface treatment. PVDF with silver ink electrodes was chosen for use with smart foam because it can withstand the higher voltage needed for actuator applications without electrical deterioration. The thickness selected for use was 28 μm which limits the required input voltage to a maximum of 300 V_{RMS} (root mean square of peak amplitude). The leads were soldered to small metal rivets as prescribed by the piezo-film manufacturer [41] such that one lead was in contact with the upper electrode (i.e. PVDF film surface) and the second lead was in contact with the lower electrode. This was done by punching a small hole in the PVDF material just large

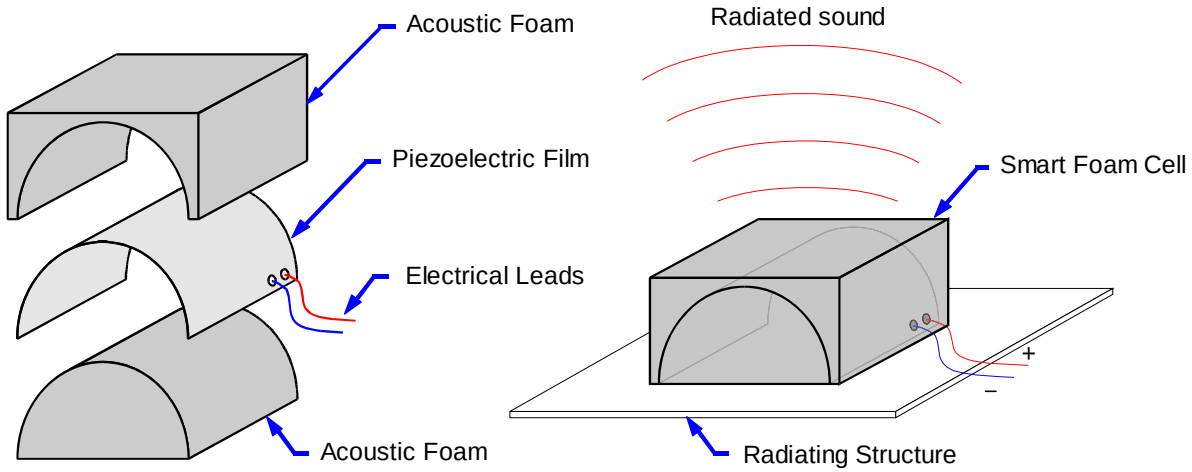

(a) (b)

Figure 2.3 (a) Components of a smart foam element. (b) Smart foam element mounted to a structure.

enough for the rivet to pass through. On the back side of the film the silver electrode material was removed using acetone and a Q-tip, a process called etching. This procedure assured that the rivet only contacted a single side of the PVDF once it was crimped in place. One rivet, with the electrical lead soldered in place, was inserted through the film from one direction and the other is inserted in the opposite direction.

An additional enhancement to the radiation efficiency of a smart foam element in the low-frequency region was achieved by adding a frame around the periphery of the smart foam element (see figure 2.4). Balsa was chosen for this application because it is rigid, lightweight, inexpensive, and easy to work with although any material with a high strength to weight ratio could be substituted. Each end of the PVDF film was glued to a balsa anchor that ran the full width of the smart foam element creating fixed boundary conditions. This results in a more efficient smart foam element because the volume velocity of the half-cylinder is maximized resulting in an increase in sound pressure level. In contrast, if the ends of the PVDF are left free (i.e. not glued) then the volume velocity is low since some of the motion induced by the piezoelectric effect translates into motion at the ends of the film (see figure 2.5). Gentry-Grace [43] compared the sound power generated by a smart foam element positioned on a rigid baffle with and without the balsa frame. In each case the elements were driven with approximately 250 V_{rms} using 0 – 1600 Hz random noise. The radiated sound power was measured in an anechoic chamber

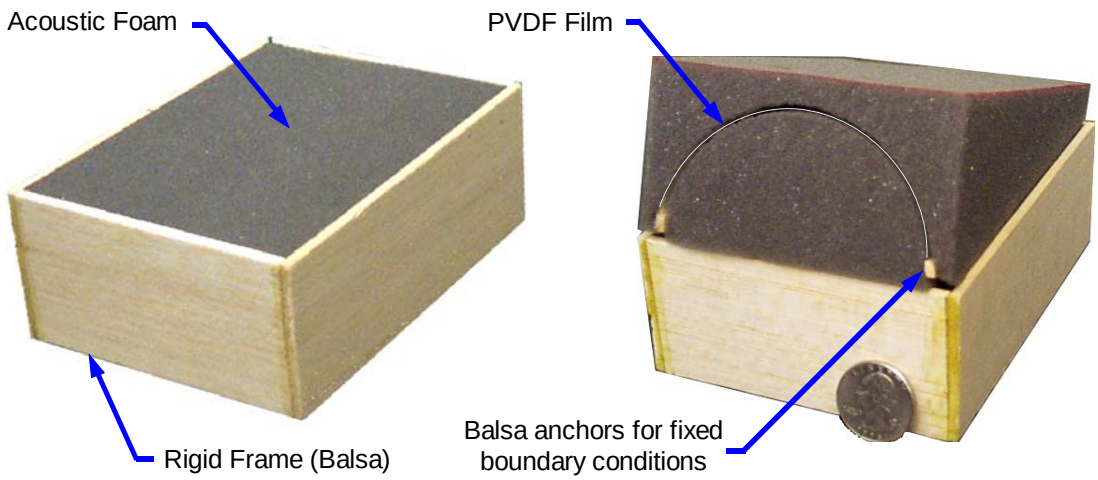

Figure 2.4 Smart foam element.

with a hemispherical array of ten microphones positioned according to ISO 3745 [45]. The addition of the balsa frame resulted in an increase of 10 dB of radiated sound power in the 200 – 650 Hz range.

It has been determined that PVDF in the form of a half-cylinder with a maximized radius is the most efficient configuration for radiation efficiency because large actuator displacements result. Given this fact alone it would be concluded that the smart foam element should be as large as possible in order to maximize the achievable impact from a single actuator element. There are other factors specific to each application to consider that influence the size and shape of a smart foam element. A vibrating structure will have varying radiation characteristics (modes) resulting from both the physical properties of the structure and the nature of the excitation. If it is desired to control the radiation from the vibrating structure, it is necessary to have an actuator configuration with control authority over the radiating modes. As an example, a panel vibrating in its first structural mode (1,1) acts like a monopole and could easily be controlled with a single active source centered on the panel. A panel vibrating in a second order mode (2,1) acts like a dipole and would require two active sources for effective control (see figure 2.6). Dual actuators as in figure 2.6(b) are optimally configured to control the (2,1) mode but, can also control the (1,1) mode by having each actuator driven together in phase. Radiating structures typically consists of contributions from many modes shapes that are excited by the disturbance, especially if the disturbance

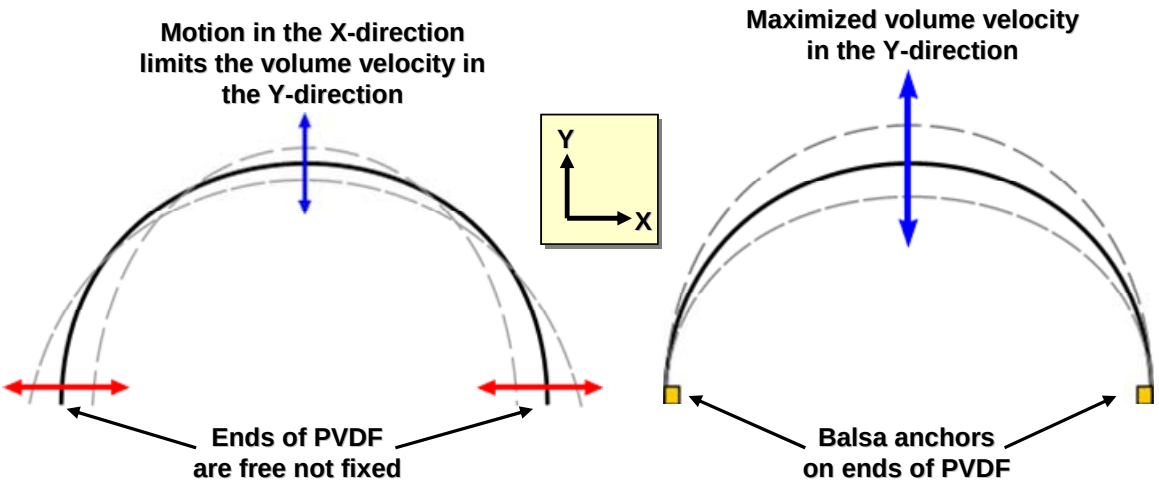

(a) (b)

Figure 2.5 (a) PVDF with free boundary conditions. (b) PVDF with fixed boundary conditions.

is broadband as is the case for a turbulent boundary layer excitation. In addition, the largest standard PVDF sheet size is 8 in. x 11in., which limits the maximum size of an actuator. A larger size could be formed with multiple sheets driven in series or custom designed sheet sizes from the manufacturer but this significantly increases the cost of the film. It is therefore important to understand the physical constraints and radiation characteristics of the system in order to properly design an optimum size and number of actuators.

2.5 CHARACTERIZATION

In order to control noise radiation from a structure through the introduction of secondary sound sources, the secondary sources must be capable of generating equal or greater sound levels than those produced by the disturbance at the error sensors. For this reason it was important to know the radiation characteristics of the smart foam elements before using them as actuators in a control system. The radiated sound power generated by a smart foam element was measured in an anechoic chamber with a hemispherical array of ten microphones positioned according to ISO 3745 [45]. The microphone array surrounded a smart foam element that was baffled and placed on the floor of the anechoic

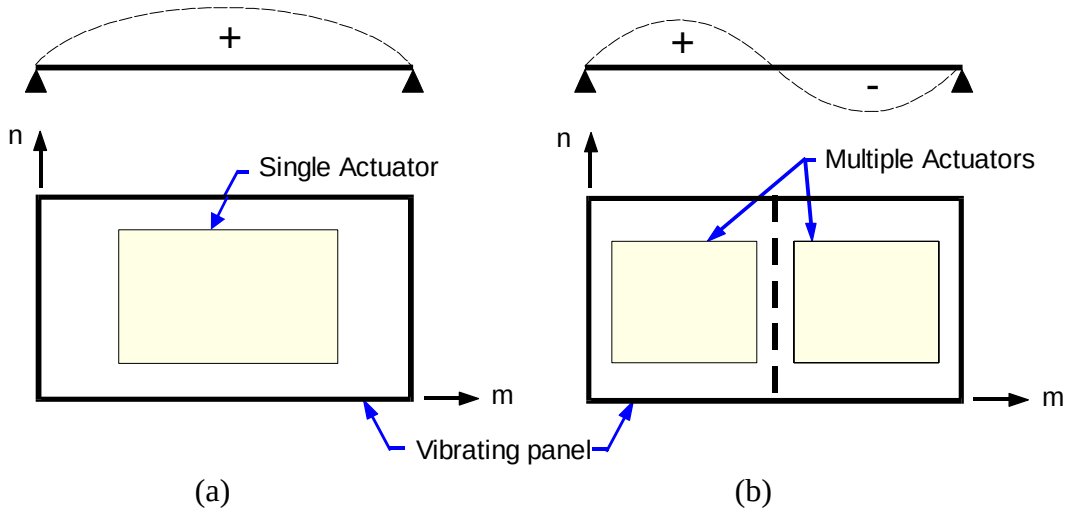

Figure 2.6 Two plate mode shapes Ψ_{mn}. (a) Ψ_{11} with single actuator. (b) Ψ_{21} with multiple actuators.

chamber (see figure 2.7). As the smart foam actuator was driven with an applied voltage the sound pressure levels at the 10 microphones were recorded and used to calculate the radiated sound power. The total acoustic power radiated by the smart foam element was calculated with the expression

$$\Pi = \frac{(S/10)}{2\rho_o c_o} \sum_{i=1}^{10} |P_i|^2 , \tag{2.4}$$

where S is the surface area of the hemisphere, P_i is the measured sound pressure level at the i^{th} microphone, ρ_o is the density of air, and c_o is the speed of sound in air at standard temperature and pressure.

Throughout the experiments involving smart foam actuators, considerable effort was put forth to improving the radiation efficiency of the smart foam actuators. As previously discussed, determining the most effective PVDF shape and orientation and the addition of a balsa frame were significant advances in smart foam performance. An additional modification associated with the balsa frame was developed that helped improve the radiated sound power across a wide band of frequencies. This modification consisted of rigidly fixing each edge of the frame to the radiating surface with glue such that the structure acts like a baffle to the backside of the smart foam actuator. All previous experiments with smart foam consisted of lightly mounting the smart foam element to the vibrating structure using a spray adhesive. Two different actuator sizes

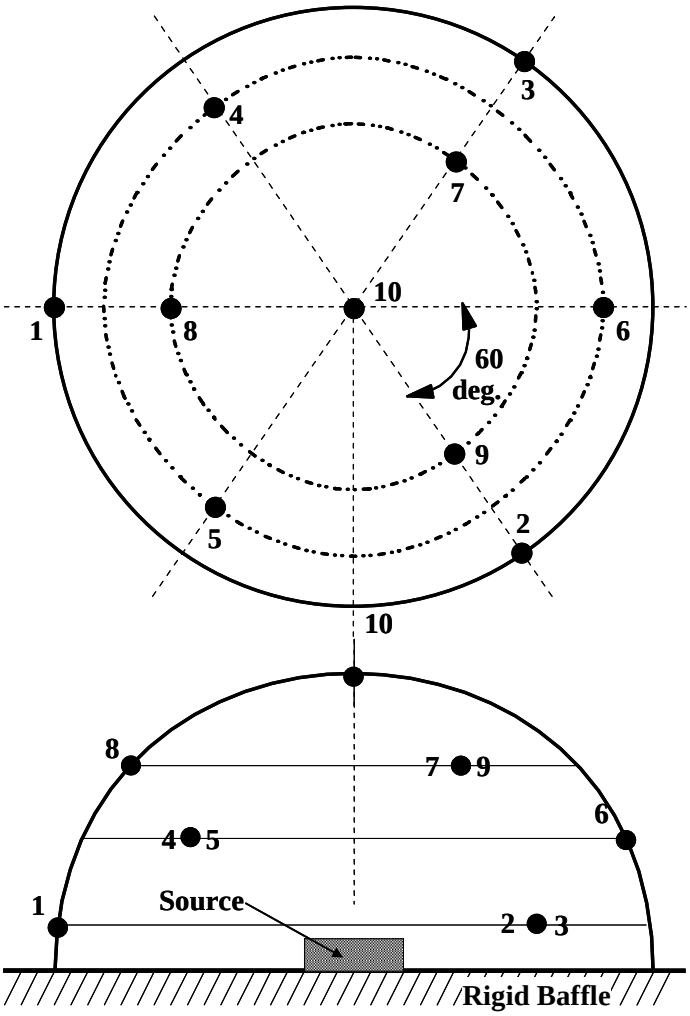

Figure 2.7 Ten microphone hemispherical array.

were arranged for testing to illustrate the smart foam improvements associated with actuator size and gluing the balsa frame (see figure 2.8). Although not shown in the illustration, each of the actuators was encased in a balsa frame. The actuator in figure 2.8(a) was lightly attached to the structure using spray adhesive and the actuator in figure 2.8(b) had each edge of the balsa frame to the radiating structure. The radiated sound power for each smart foam configuration was measured in an anechoic chamber using 10 microphone hemispherical array (figure 2.7) and equation 2.4. The results of each configuration are plotted in figure 2.9(a). Figure 2.9(b) plots in third-octave bands the increase in sound power level associated with the smart foam improvements. Note that there was an increase in radiated sound power across almost the entire bandwidth with only a marginal increase in treated surface area (approximately 6%). It was only at the

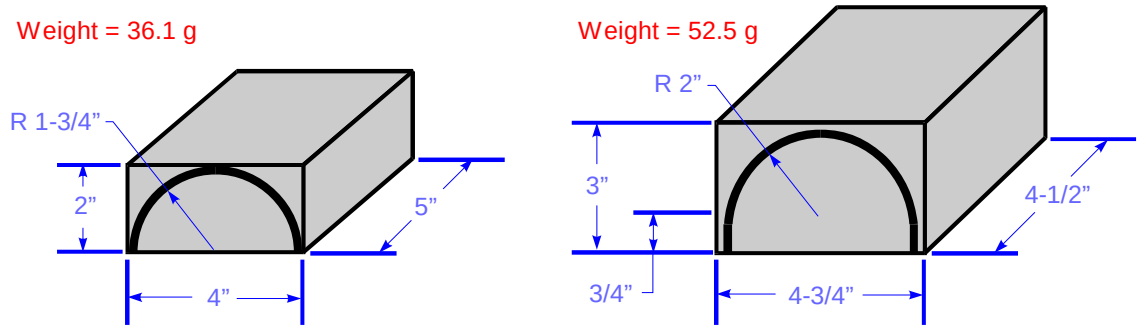

(a) (b)

Figure 2.8 (a) Original smart foam element configuration. (b) Modified smart foam element configuration.

1600 Hz center frequency and above where less power was achieved, which can be considered insignificant since the PVDF would not be expected to operate at these higher frequencies where the passive attenuation properties of the foam work well. It should also be noted that the radiated sound power is significantly less at the lower frequencies. This is the result of a fundamental limitation of piezoelectric materials, including PVDF, to generate the large displacements necessary to generate low frequency noise. It is thus necessary to limit the active control bandwidth to a region where the smart foam elements radiate efficiently. This is discussed in more detail in Chapter 5.

2.6 SUMMARY

A generic smart foam element has been developed for use in the control of sound radiation from structures. Considerable effort has been placed on accentuating the low frequency radiation efficiency of the active component of the smart foam element. It has been concluded from this effort that the PVDF should be formed in a half-cylinder shape with rigid boundary conditions, the actuator should be enclosed within a rigid frame, and this frame should be glued to the radiating structure. In addition to improving the radiation efficiency of the PVDF within a smart foam element, the changes also affect the passive attenuation properties.

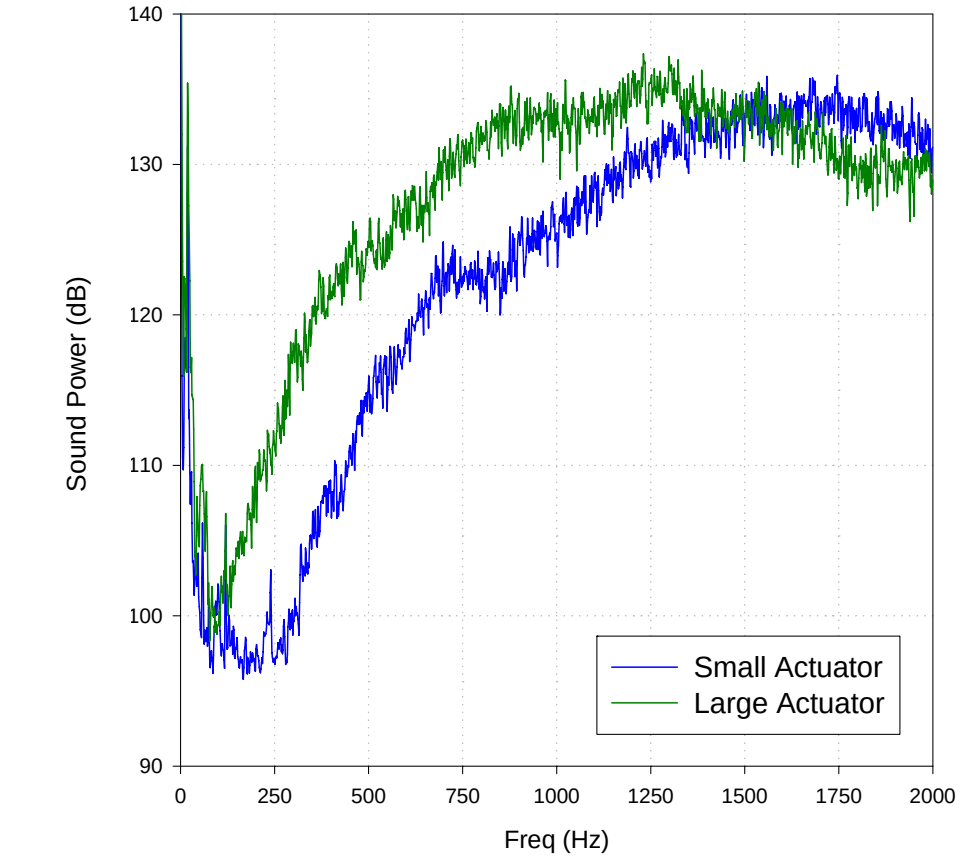

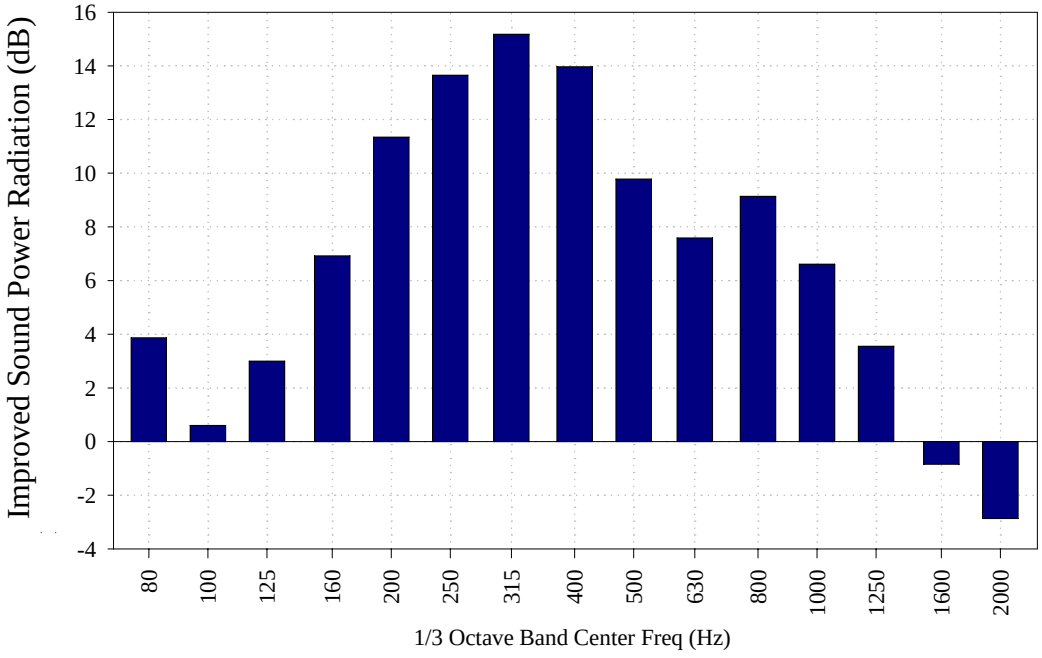

(b)

Figure 2.9 (a) Radiation characteristics of a smart foam element. (b) Increase in sound power radiation due to smart foam improvements.

Chapter 3

Control Methodology

3.1 INTRODUCTION

Paul Lueg first introduced controlling unwanted noise by the introduction of additional sound when he filed for a US patent in 1934 [46]. The system Lueg proposed was designed to control plane wave sound in a duct and consisted of an upstream microphone for detecting the propagating sound waves and a downstream loudspeaker used as a secondary noise source. The two components were linked with an electronic control system that was responsible for adding an appropriate delay and amplification to the detected signal such that the emitted signal at the speaker was an inverted duplicate of the disturbance. Lueg's system was practically the same methodology and contained the same components as systems implemented in many of today's commercial active noise control systems. Although this concept was developed in 1934, the problem of implementing control systems to solve real problems was limited due to the inability to process the required data efficiently and accurately. Recently, with the advent of inexpensive digital signal processors (DSP), these feedforward control techniques are now practical solutions to numerous control problems. Not only are they implemented to control plane wave sound propagation in ducts, as Lueg illustrated in his patent, but also multi-channel systems with less predictable disturbance characteristics, such as those induced by a turbulent boundary layer.

The following sections will give a brief introduction into the development of a filtered-x LMS control algorithm [47]. This discussion will then expand to include the

multiple input multiple output (MIMO) feedforward filtered-x LMS control algorithm [48] and two control issues regarding its implementation: causality and coherence.

3.2 FEEDFORWARD FILTERED-X LMS ALGORITHM

3.2.1 Single Channel Control

The general purpose of a feedforward control system is to reduce the levels of a disturbance through the addition of a secondary control signal that is determined by a computational algorithm. This algorithm is often tasked with minimizing sound radiation from structures when used in Active Noise Control (ANC) applications. One such feedforward control algorithm is the Filtered-x LMS algorithm [47], a modified version of the least-mean-square (LMS) algorithm commonly used for signal cancellation. Figure 3.1 is a block diagram of a single input single output (SISO) filtered-x LMS control system. The plant (i.e. physical system) output $e(n)$, or error signal, can be defined as

$$e(n) = d(n) + y(n), \tag{3.1}$$

where $y(n)$ is the plant response to the control input, $d(n)$ is the plant response to the disturbance input, and n denotes a sampled signal or sequence number. The measured system response $y(n)$ in equation 3.1 can be replaced so that

$$e(n) = d(n) + T_{ce}(z)u(n), \tag{3.2}$$

where $T_{ce}(z)$ is the z-transform of the transfer function between the system response $y(n)$

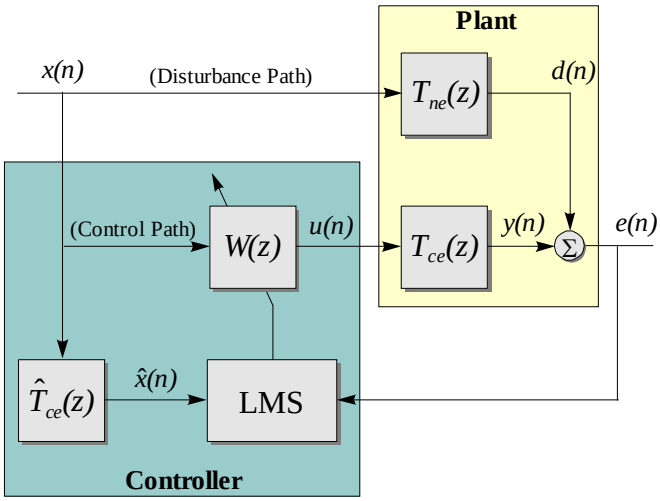

Figure 3.1 Block diagram of single channel Filtered-x LMS feedforward control system.

and the control sequence $u(n)$.

The control sequence $u(n)$ is the output signal from the controller and is obtained from the adaptive FIR (Finite Impulse Response) filter represented as $W(z)$. The adaptive FIR filter is a fundamental component used in the implementation of many control algorithms and is characterized by having zero impulse response after a set number of samples. A FIR filter generates an output to a digital system that is the weighted sum of previous input values, so that

$$y(n) = \sum_{i=0}^{I-1} W_i(n)x(n-i), \tag{3.3}$$

where $W_i(n)$ is the i^{th} filter coefficient and I is the filter order. A block diagram representation of this difference equation is shown in figure 3. where z^{-1} denotes a unit delay operator. This operator, when performed on a sequence, introduces a delay by one sample such that $z^{-1}x(n) = x(n-1)$. The adaptive FIR filter, $W(z)$, can thus be represented as an operator such that

$$W(z) = W_0 + W_1 z^{-1} + W_2 z^{-2} + \cdots + W_{L-1} z^{-(I-1)}, \tag{3.4}$$

$$= \sum_{i=0}^{I-1} W_i z^{-i}, \tag{3.5}$$

and consequently the control sequence can be defined as

$$u(n) = W(z)x(n). \tag{3.6}$$

Substituting equation 3.6 into equation 3.2, the plant output, or error becomes

$$e(n) = d(n) + T_{ce}(z)W(z)x(n). \tag{3.7}$$

An error criterion, or cost function, must now be defined such that the plant input signal $u(n)$ can be adjusted to minimize the plant response $e(n)$. The most commonly used cost function for active noise control is defined as

$$C(W_i) = \mathrm{E}[e^2(n)], \tag{3.8}$$

where $\mathrm{E}[e^2(n)]$ is the expected value of the mean-square error signal and is a quadratic function of the filter coefficients. In the frequency domain, he quadratic cost function, or performance surface, can be plotting for visualization as a function of the real and imaginary components of the plant input $u(n)$ and has a unique global minima. This performance surface is a bowl-shaped error function where the elliptical contour lines

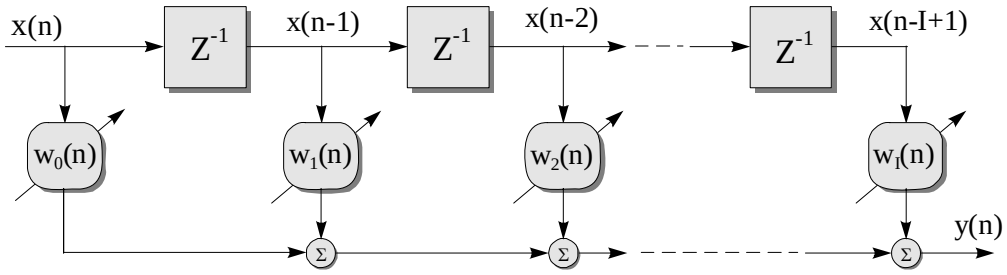

Figure 3.2 Single-input adaptive FIR filter where output is the weighted sum of past input values.

represent lines of constant E[$e^2(n)$]. An adaptation algorithm is used to compute the gradient of this quadratic surface and converge in the negative direction toward the global minima. The LMS algorithm uses the steepest decent method [47] as an adaptation criterion for adjusting the filter coefficients W_i $(i = 0,\ldots,I-1)$ so that the minimum mean-square error is achieved. The algorithm used to adjust the weights can be written as

$$W_i(n+1) = W_i(n) - \mu \frac{\partial C}{\partial W_i}, \tag{3.9}$$

where μ is know as the convergence coefficient and controls the step size or rate of convergence in the minimization process.

The cost function in equation 3.8 when differentiated with respect to the filter coefficients W_i yields the following expressions

$$\frac{\partial C}{\partial W_i} = 2\mathrm{E}\left[e(n) \frac{\partial e(n)}{\partial W_i} \right], \tag{3.10}$$

$$= 2\mathrm{E}\left[e(n) T_{ce}(z) x(n-i) \right], \tag{3.11}$$

$$= 2\mathrm{E}\left[e(n) \hat{x}(n-i) \right], \tag{3.12}$$

where E[ ] denotes the expected value operator and

$$\hat{x}(n-i) = T_{ce}(z) x(n-i). \tag{3.13}$$

Substituting equation 3.12 into equation 3.9, the update equation becomes

$$W_i(n+1) = W_i(n) - 2\mu(n) \hat{x}(n-i) e(n), \tag{3.14}$$

where $\hat{x}(n)$ is known as the filtered reference signal and is a product of filtering the reference signal $x(n)$ with an approximate model of the plant $\hat{T}_{ce}(z)$. This control

algorithm is known as the filtered-x LMS algorithm. The plant model $\hat{T}_{ce}(z)$ is built using a FIR filter in which the LMS algorithm adapts the filter coefficients while driving the actuator and measuring the response at the error sensor $e(n)$. This process is performed off-line and is know as the system identification.

The convergence coefficient μ controls the step size the LMS algorithm takes as it iterates to the global minimum of the quadratic cost function. As the convergence coefficient μ increases, the time for convergence decreases. Large μ values can, however, cause the algorithm to become unstable where the control inputs increase without bounds. Widrow *et al.* [47] states that in general, the stability of the algorithm can be calculated using the input autocorrelation matrix R such that

$$0 < \mu < \frac{1}{Trace[R]}, \tag{3.15}$$

where

$$Trace[R] = \sum_{i=0}^{I} x_i^2(n). \tag{3.16}$$

A large value of μ results in quicker convergence time but a large coefficient may cause the algorithm to step over the minimum value during iteration. In order to assure quick convergence on the surface minima, the convergence parameter μ should be set high for initial convergence and then reduced to assure that the minima is obtained.

There are several general properties of the filtered-x LMS algorithm that make it an advantages choice for use in noise control applications [12]:

1. Changes in the disturbance signal are rapidly tracked because the algorithm can converge on a time scale comparable with the delay in the error path.
2. The algorithm is robust to errors in the estimation of the error path used to generate the filtered reference signal.
3. The algorithm is easy to implement, only differing from the LMS algorithm in that it requires the generation of the filtered reference signal.

The algorithm does have limitations, however, that exist from poor coherence between reference and disturbance signal, inaccurate model of the plant, low control

filter order, and low sample rate. Each of these limitations, with the exception of poor coherence, is a function of the processing speed of the DSP.

3.2.2 Multiple-Channel Control

It may not always be possible to obtain global noise control with the introduction of a single error sensor and secondary source. Often the primary disturbance or the radiated sound field is such that it requires the introduction of multiple sources and error sensors to achieve global control or control over a large volume. The filtered-x LMS algorithm has been developed for use with multiple secondary control sources and error sensors [48]. The modified update equation for each control filter coefficient with L sensors and M actuators is

$$W_{mi}(n+1) = W_{mi}(n) - 2\mu \sum_{l=1}^{L} \hat{x}_{lm}(n-i) e_l(n), \tag{3.17}$$

where $\hat{x}_{lm}(n)$ is the reference signal filtered with a model of the system path from the m^{th} actuator and the l^{th} error sensor at sample n. Note that equation 3.17 is equivalent to the SISO system of equation 3.14 when $L = M = 1$. In addition, the level of control that can be obtained by a control system also depends on the quality of the reference signal used to capture the dynamics of the disturbance. For a spatially incoherent disturbance, as provided by a turbulent boundary layer, multiple references (K) may be required to achieve adequate control levels. The multiple-channel controller now contains MK finite impulse response filters each updated by the control algorithm. Section 3.3.2 discusses multiple coherence and presents a control example that helps to quantify the benefits of using multiple reference signals.

3.3 PRACTICAL IMPLEMENTATION OF CONTROL ALGORITHM

All experiments conducted in this work utilized the multi-channel version of the filtered-x LMS algorithm. The control code was written in Assembly and C programming languages for a Spectrum Quad TMS320C40 digital signal processor (DSP). The DSP processes data using 4 parallel processors and therefore the system runs at peak efficiency when the computation can be divided easily into multiples of 4. Flexibility has

been incorporated into the control code so that numerous control scenarios can be examined using the same controller. Control performance for a particular set of control parameters may have been compromised, however, to account for the built-in flexibility. To take full advantage of the computing capabilities of the DSP, the control code could have been customized for each set of control parameters, but this would have resulted in countless configurations and was not practical for this phase of the project.

Virginia Tech has developed a LabVIEW® interface program for use with the multi-channel controller that allows the user to easily choose a desired set of control parameters. The following is a methodology and procedure for using the multi-channel filtered-x LMS control algorithm that Virginia Tech has implemented. Details about the flexibility built into the controller will also be included in the procedure.

1. Select the number of reference sensors (4), error sensors (8), and actuators (8) to be used in the experiments. The value in parentheses is the maximum value allowed by the program.
2. Select the sampling frequency, system ID coefficients, and control path coefficients. The system ID coefficients are the number of FIR filter coefficients that are used to build the model of the plant $\hat{T}_{ce}(z)$, through which the reference signal $x(n)$ is filtered. The control path coefficients are the number of coefficients present in the adaptive FIR filter $W(z)$ that are updated by the LMS algorithm to generate the secondary control signal.
3. Set the system coupling. A fully coupled system will model the control paths from an actuator to each of the error sensors, whereas an uncoupled system will model the control path from an actuator to a single error sensor. Typically the control results are best when the system is fully coupled.
4. The controller builds the plant models $\hat{T}_{ce}(z)$, or a matrix of transfer functions, by sequentially driving each actuator and measuring the response at all of the error microphones (e.g. $\hat{T}_{ce}(z)$ will be a 4 x 4 matrix if a system has 4 actuators and 4 error sensors).

5. The controller then drives the actuators such that the error signals are minimized. The user can control the rate of convergence by adjusting the magnitude of the convergence coefficient μ.
6. The user can monitor the error signals and adaptive filter coefficients to assess when maximum control is achieved. Also, the levels of the control signals and reference signals can be monitored to assure that the signals do not clip.
7. A *Control On/Off* button can be toggled so that the control performance can be monitored and acquired using a data acquisition system.

Figure 3. is a general block diagram that presents the physical implementation of the filtered-x LMS control system. In addition to the details already presented about the controller, it should be noted that the A/D and D/A converters are incorporated as part of the controller. All of the control channels incorporate low-pass filters that prevent

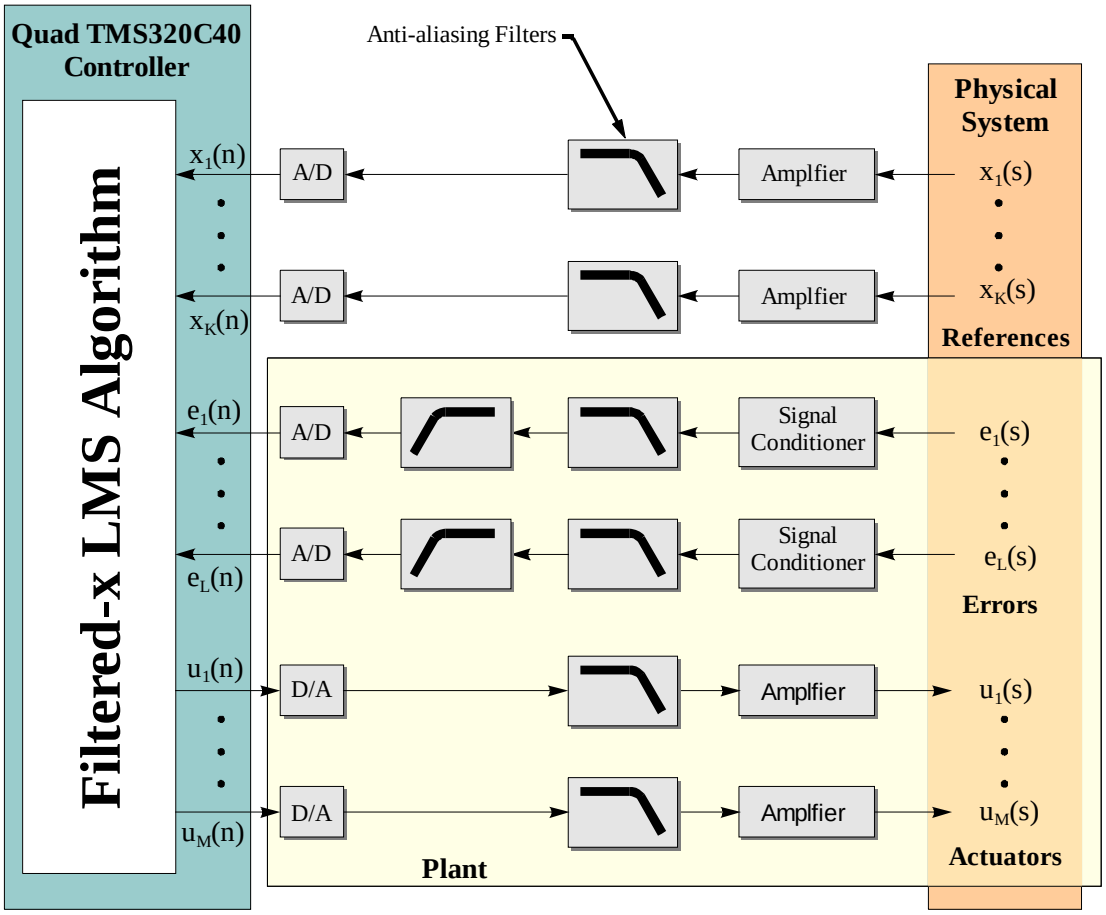

Figure 3.3 Block diagram of MIMO control setup.

aliasing and the introduction of high frequency noise. Sensors mounted to the physical system generate the reference signals x_K that provide the controller with the disturbance characteristics. For a vibrating structure these sensors are often accelerometers, which, depending on the amplitudes of vibration, may need signal amplification prior to being processed by the controller. The error sensors e_L measure the superposition of the radiated sound field, generated by the disturbance, and the secondary sound field generated by the controller driven actuators. The controller uses the error signals along with the filtered references $\hat{x}_{LM}(n)$ to adapt a set of control filters that drive the actuators. In ANC applications, the primary interest is reducing radiated sound so the error sensors are often microphones. The filtered-x LMS controller starts by controlling the most dominant portion of the disturbance spectrum, however, the signals at the error sensors adapt the controller, so their measured response can be filtered to target a particular spectrum bandwidth. For example, if you have a broadband disturbance but are not interested the content below 400 Hz, you can high-pass filter the error signals and the control effort will be concentrated on the disturbance above 400 Hz. The actuator signals u_M generated by the controller also require amplification because the input and output limits of the DSP are ± 10.0 Volts. All of the actuators, error sensors, amplifiers, and filters used in the measurement of the sound field and the generation of control signals are modeled as components of the plant. The delays and system dynamics that are introduced by these components are therefore included in the plant models $\hat{T}_{ce}(z)$ that are used to filter the reference signals $\hat{x}_{LM}(n)$. Specifics about the physical hardware used for the experiments in this research are presented in Chapter 5.

3.3.1 Causality

An important aspect related to the implementation of feedforward control systems for the control of broadband disturbances is system causality. A feedforward system is said to be causal when the input signals to the controller are obtained with enough time advance so that the processing and propagation of the control signals meet and cancel the disturbance signals at the error sensors. This implies, from figure 3.1, that the propagation time of the disturbance $x(n)$ through the control path should be less than or

equal to the propagation time through the disturbance path. Causality is only an issue when the disturbance is broadband since a sinusoidal excitation is deterministic in nature and its future values can always be predicted under steady-state conditions.

The level of performance that can be achieved with a feedforward control system diminishes when causality is not satisfied. Burdisso *et al.* [49] proposed an analytical approach to predicting the control performance of non-causal feedforward control systems with broadband inputs. This work demonstrated that some level of reduction in the error signal mean-square value is always achievable for any non-causal control system.

Control path delays can result from the use of anti-aliasing filters, the process of sampling, and the physical characteristics of the plant. These delays can be compensated for in systems with compact noise sources because the reference can be placed upstream close to the source, however, this is not as easy for distributed disturbances such as turbulent boundary layer noise. The analysis by Burdisso *et al.* [49] did show that the deterioration in the control performance due to the delays in the control path could be partially compensated by increasing the order of the control filter $W(z)$.

3.3.2 Multiple Coherence

The maximum level of control that can be achieved by a feedforward filtered-x LMS is determined by the coherence between the reference signal and the disturbance signal. The ordinary coherence function is defined as

$$\gamma_{xd}^2(f) = \frac{|S_{xd}(f)|^2}{S_{xx}(f)S_{dd}(f)}, \quad 0 \le \gamma_{xd}^2(f) \le 1, \tag{3.18}$$

and is a measure of the extent to which an output signal $d(n)$ may be predicted from an input signal $x(n)$ by an optimum linear least-squares relationship [47]. The notation used was selected to be consistent with figure 3.1, where the subscript x refers to the reference signal and d the signal at the error sensor due to the primary disturbance plus any measurement noise. The cross-spectral density function is represented by $S_{xd}(f)$, where the input and output autospectral density functions are represented by $S_{xx}(f)$ and $S_{dd}(f)$

respectively. The coherent output spectrum $S_{vv}(f)$ can be defined in terms of the output autospectral density function $S_{dd}(f)$ such that

$$S_{vv}(f) = \gamma_{xd}^2(f) S_{dd}(f), \tag{3.19}$$

and the associated noise output spectrum is given by

$$S_{nn}(f) = [1 - \gamma_{xd}^2(f)] S_{dd}(f). \tag{3.20}$$

Note that when $\gamma_{xd}^2(f)$ is equal to 1 the output noise spectrum $S_{nn}(f)$ is 0, and the coherent output spectrum $S_{vv}(f)$ is equivalent to the output autospectral density function $S_{dd}(f)$ [47]. In a linear feedforward control system, $S_{vv}(f)$ represents the controllable portion of the error signal and $S_{nn}(f)$ the uncontrollable portion, therefore, these quantities can be used to estimate the performance of an active control system. For example, at a particular frequency a coherence value of $\gamma_{xd}^2(f) = 0.99$ will yield a maximum of 20 dB attenuation and $\gamma_{xd}^2(f) = 0.9$ produces 10 dB attenuation.

It has been shown that the potential attenuation of a single-channel active control system depends on the level of coherence between the error and reference signals. A similar correlation has been developed, in which a multiple coherence function [12] is used as a performance estimation tool for multi-channel active control systems. In a multi-channel system, a single error signal has information about the disturbance characteristics due to all of the reference signals and not just a single reference, as is the case for the ordinary coherence function. The multiple coherence function is defined as

$$\gamma_{xd}^2(f) = \frac{\mathbf{s}_{xd}^H(f)\mathbf{S}_{xx}^{-1}(f)\mathbf{s}_{xd}(f)}{S_{dd}(f)}, \quad 0 \le \gamma_{xd}^2(f) \le 1, \tag{3.21}$$

where $\mathbf{s}_{xd}(f)$ is a vector of cross-spectra between each reference sensor and the signal at a single-error sensor. The cross-spectra between each of the reference sensors is represented by the matrix $\mathbf{S}_{xx}(f)$ and $S_{dd}(f)$ is the power spectral density of the signal at the error sensor due to the primary field and measurement noise. A Hermitian transpose is performed on the vector $\mathbf{s}_{xd}(f)$, denoted by the superscript *H*, and is defined as the complex conjugate of the transpose

$$\mathbf{s} = \begin{bmatrix} s_1 \\ s_2 \\ \vdots \\ s_K \end{bmatrix}, \qquad \mathbf{s}^H = \begin{bmatrix} s_1^* & s_2^* & \cdots & s_K^* \end{bmatrix}, \tag{3.22}$$

where * denotes the complex conjugate. Similar to the single-reference case, equation 3.19 and equation 3.20 can be used to estimate the performance of the multi-channel active control system.

An analysis was conducted that compared the differences in estimation of control performance using the ordinary coherence function and the multiple coherence function. In each case, the radiation from a panel, excited by a turbulent boundary layer disturbance (see Chapter 4), was monitored with a single error microphone suspended approximately 20 in. above the surface of the panel. Figure 3.4(a) shows the coherence between the microphone and a single reference accelerometer mounted to the panel. Figure 3.4(b) shows the potential control as a function of the measured coherence using equation 3.19 and equation 3.20. Notice that there is only control potential below 400 Hz, the frequency band where there was good coherence. Figure 3.5(a) shows the multiple coherence between the same microphone and 4 reference accelerometers distributed on the panel. Notice that the coherence has increased over the entire bandwidth with significant improvement up to 800 Hz. Consequently, because of the improved coherence results, there is now control potential up to 1400 Hz as depicted by figure 3.5(b).

The advent of higher digital signal processors and the desire to control more complex systems have led to the development of the multiple-channel controllers. These controllers often require multiple reference sensors to determine the appropriate secondary signal that, when combined with the primary disturbance, results in an attenuation in sound pressure level. It may often be difficult to know the number of references required to achieve the desired level of control. The multiple coherence function is a tool that can be used to quantify the control potential of a multi-channel control system given an array of references.

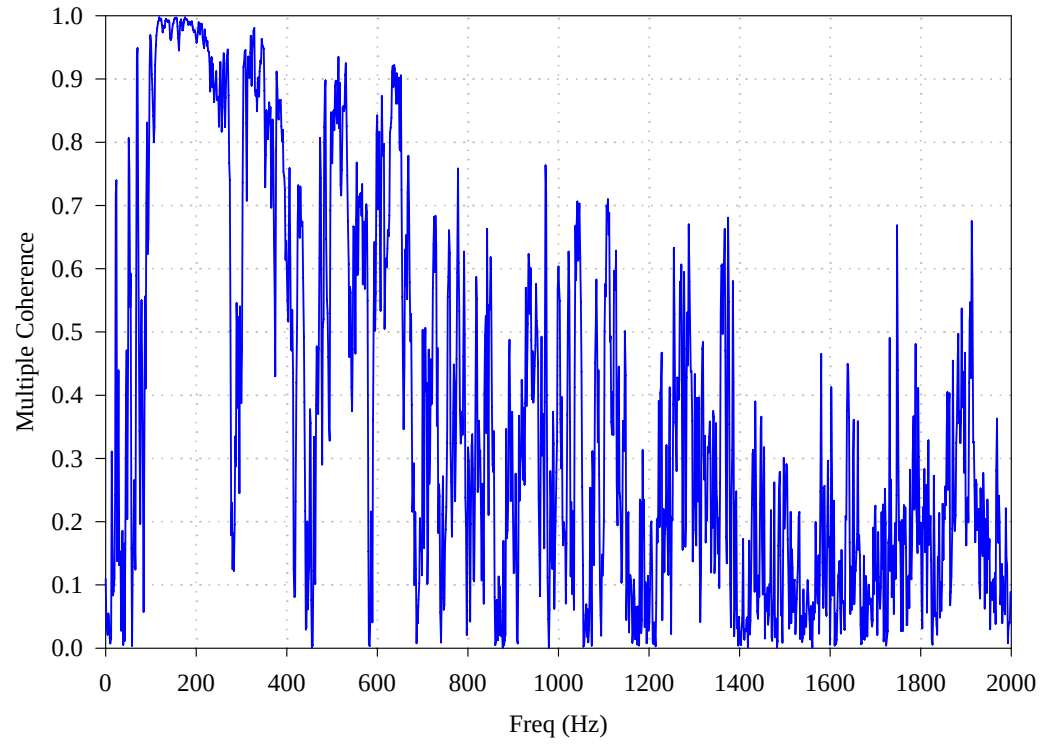

(a)

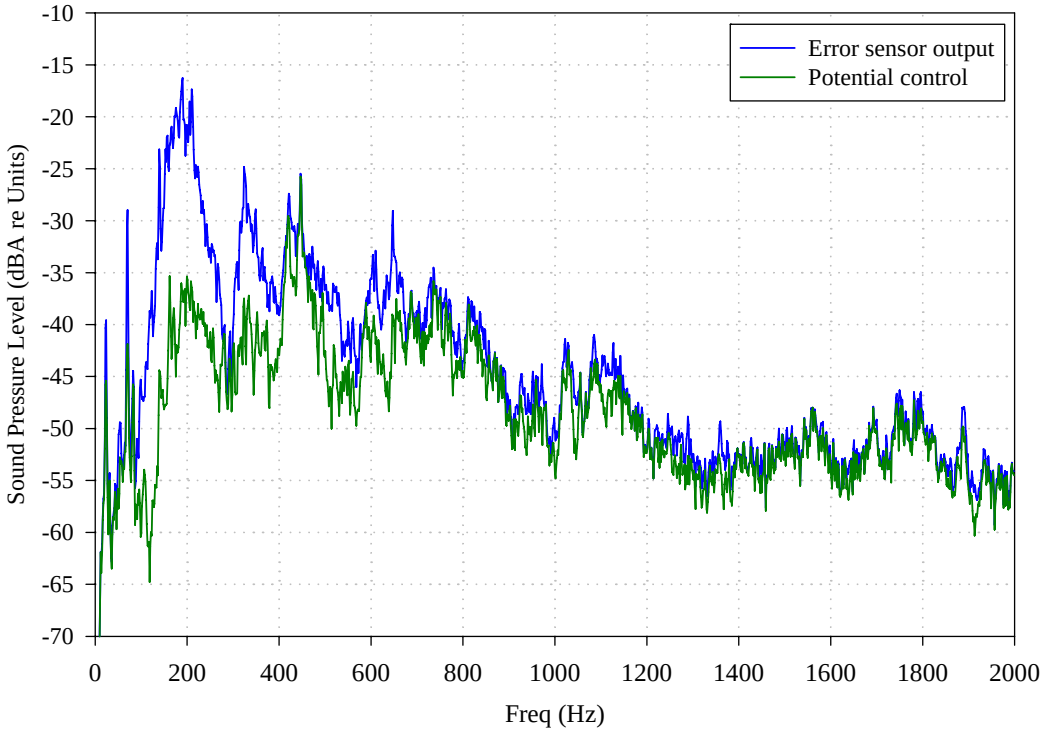

(b)

Figure 3.4 (a) Ordinary coherence function between one reference sensor and one error. (b) Estimate of active control based on coherence.

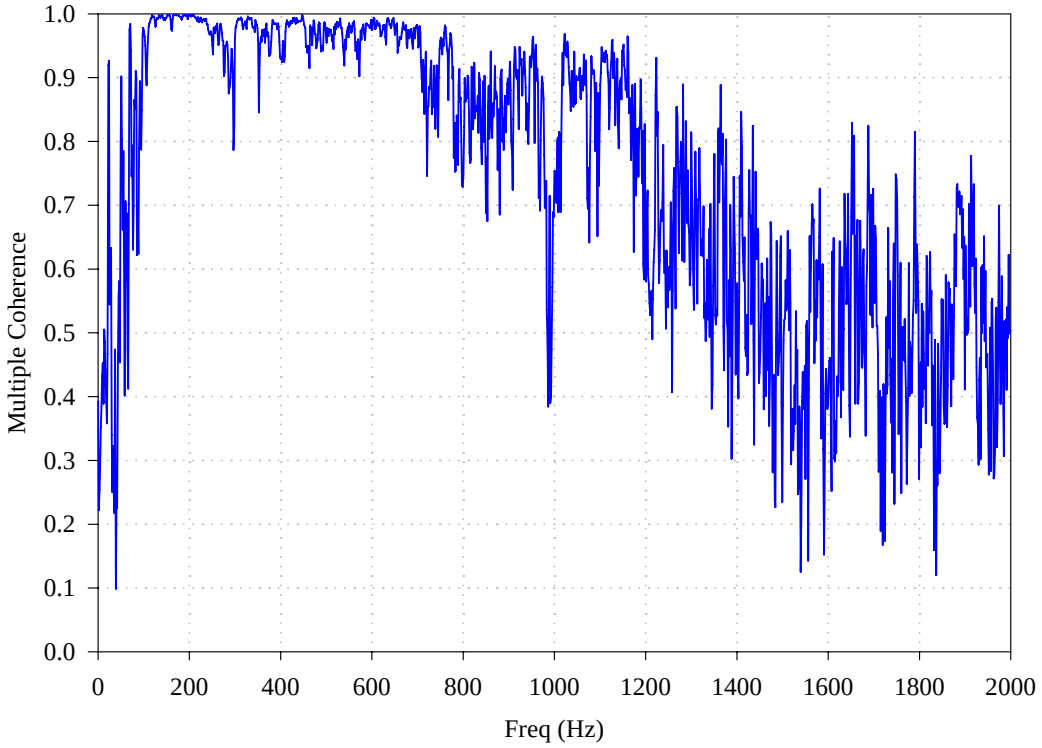

(a)

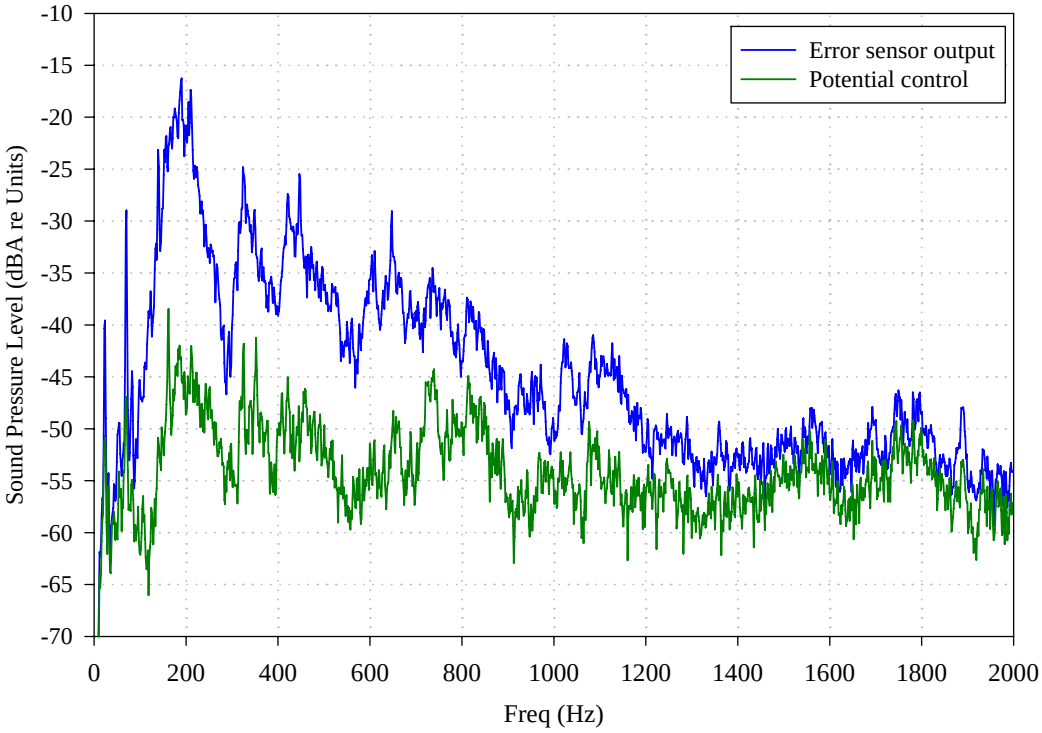

(b)

Figure 3.5 (a) Multiple coherence function between four reference sensors and one error. (b) Estimate of active control based on coherence.

Chapter 4

Test Methodology and Experimental Components

4.1 INTRODUCTION

The interior noise within an aircraft cabin is the product of three primary noise sources: engine noise, noise from structural vibrations induced from wing mounting and reciprocating engines, and aerodynamic noise. This research focused on the control of aerodynamic noise or, more specifically, turbulent boundary layer noise in the passenger cabin. A schematic showing the concepts involved in the control of interior cabin noise using smart foam elements can be seen in figure 4.1. As shown, an aerodynamic flow excites the exterior fuselage panels of an aircraft whose vibration then radiates noise into the cabin. The control concept is to position an array of smart foam actuators between the fuselage skin and interior trim panel of the aircraft. These actuators act as secondary noise sources that destructively interfere with the disturbance and reduce the overall

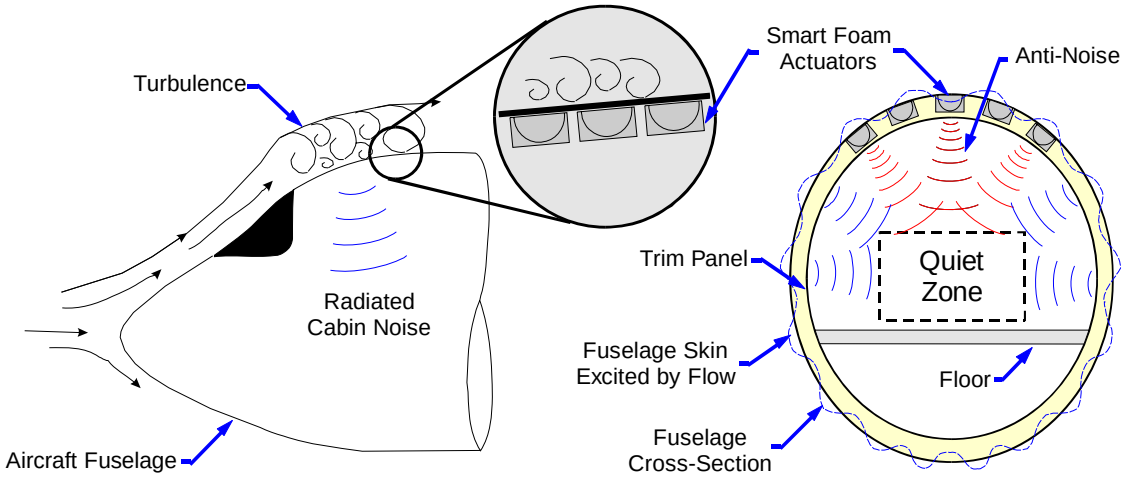

Figure 4.1 Schematic of interior noise control using smart foam actuators.

sound pressure level within the cabin. Actual flight tests are the ideal test environment for evaluating control schemes tasked with minimizing interior cabin noise, however, in the early stages of the research process it is more cost efficient to test in a laboratory environment. It was therefore necessary to design laboratory experiments that simulated the interior cabin noise generated by a turbulent boundary layer flow.

Wind tunnels are required within a laboratory environment to simulate the flow conditions that are experienced in flight. Experiments throughout this research project were conducted using three separate wind tunnel test facilities. The smallest of the three wind tunnels was located at Virginia Polytechnic Institute and State University (VPI) and was used primarily to prepare for testing at the other test facilities. There were no usage times and availability restrictions on the VPI tunnel allowing numerous actuator and controller configurations to be tested prior to use at the other facilities. Although each wind tunnel differed in size and flow speeds, the experimental test methodology and procedure was common at all three sites and is displayed in a schematic in figure 4.2. A flexible test panel, representing an aircraft fuselage skin, was mounted on the side of a wind tunnel whose fan was used to generate the turbulent boundary layer flow. The flow introduced vibrations in the test panel that, subsequently, radiated noise into an anechoic enclosure. The anechoic enclosure is analogous to an aircraft cabin and was used to accurately monitor the radiated sound pressure levels by minimizing the effects of room reverberation and outside noise sources. The active/passive smart foam actuators were

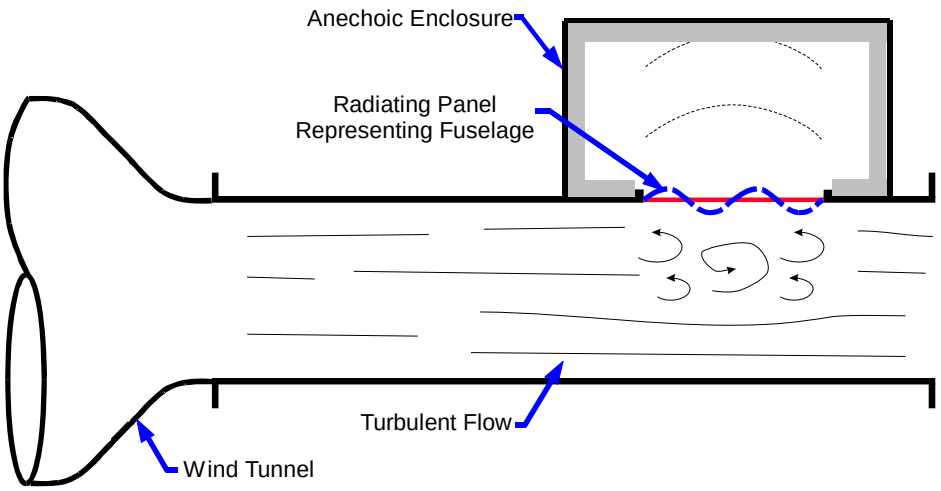

Figure 4.2 Schematic of experimental methodology.

mounted to the panel, within the anechoic enclosure, and used as secondary noise sources.

Information regarding the development of the smart foam actuators and the components used in their construction was presented in Chapter 2 and the adaptive multiple channel feedforward control strategy used in the experiments was outlined in Chapter 3. This chapter describes the design and characterization of the VPI wind tunnel test facility and the anechoic enclosure, which was a common component used in the experiments at all three test facilities.

4.2 VPI WIND TUNNEL

The test panels for both of the NASA wind tunnels were 60 in. long, 20 in. wide, and constructed from 0.06 in. thick aluminum. Each panel was reinforced with longitudinal and vertical stiffeners that sectioned the panel into six smaller bays (more detail regarding each of the test panels is presented in Chapter 5). The goal of the smart foam experiments was to control the radiation from one of the six panel subsections, therefore, the VPI panel was designed to be 20 in. long, 10 in. wide, and constructed from 0.05 in. thick aluminum (i.e. one-sixth the size of the larger test panels). The panel was mounted in a rigid steel frame using screws spaced approximately 1.5 in. apart that was then flush mounted onto the side of the wind tunnel test section as illustrated in figure 4.3.

The wind tunnel test section cross-section measured 12 in. x 12 in. and was 60 in. long. The cut-on frequency for the VPI wind tunnel duct was determined to 563 Hz (the frequency where half a wavelength fits within the ducts interior dimensions). Below the duct cut-on frequency only plane wave propagation is present. Above the cut-on frequency modal density begins to increase rapidly with frequency, which can make active noise control more challenging due to an increased difficulty in characterizing the disturbance. The cut-on frequency was determined by driving a speaker with random noise at one end of the duct and measuring the sound pressure levels at a vertical array of five microphones spaced 1.5 in. apart at the other end (see figure 4.3). Figure 4.4 shows the response characteristics at each of the 5 vertical microphones to be virtually the same below the cut-on frequency of 563 Hz suggesting plane wave propagation.

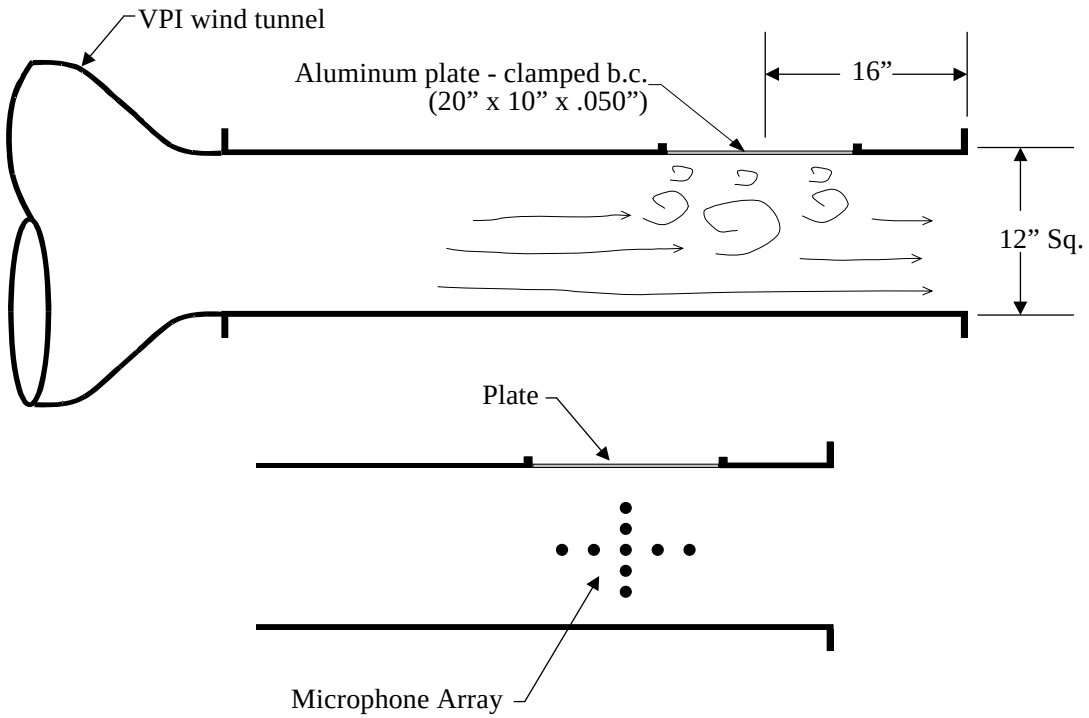

Figure 4.3 VPI wind tunnel configuration.

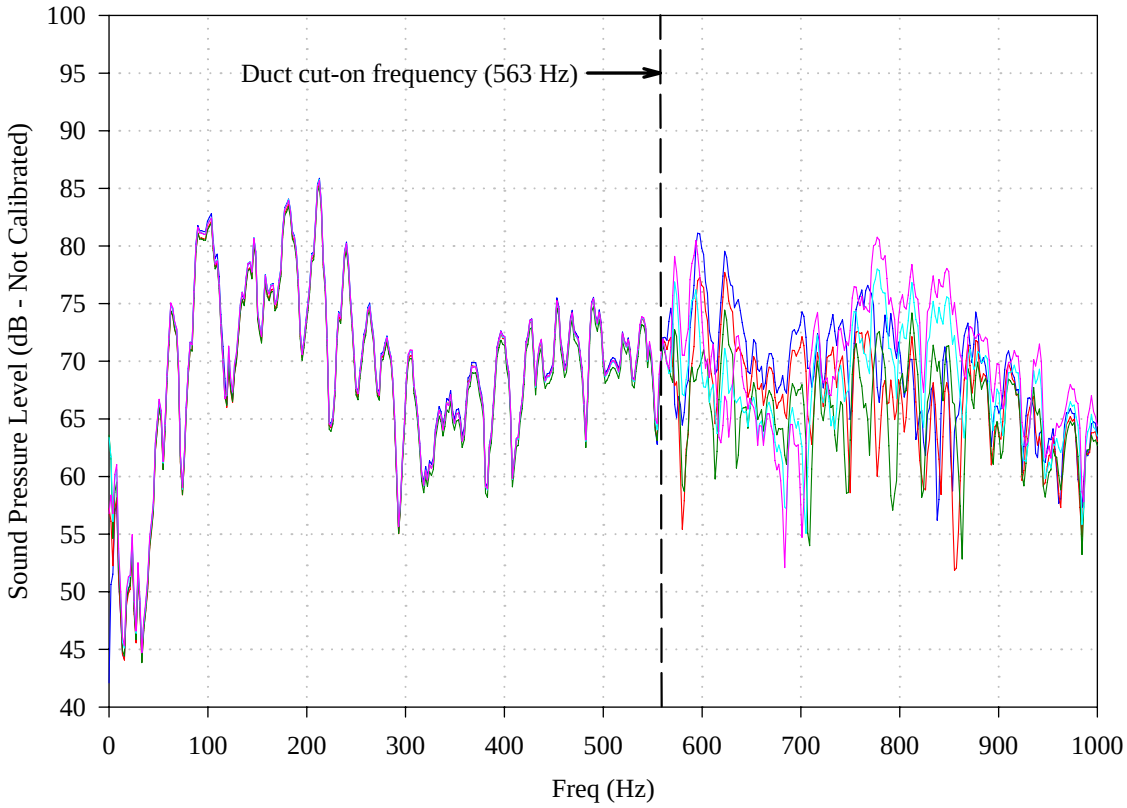

Figure 4.4 Experimental demonstration of cut-on frequency.

One significant characteristic of the VPI wind tunnel was the propagation of fan noise down the tunnel. This was an undesirable characteristic because the goal of this work was to demonstrate noise control of a turbulent boundary layer and not noise control of discrete frequency fan tones. In an effort to characterize the wind tunnel, the mean square pressure was acquired using the nine-microphone array (see figure 4.3) for two test conditions. The first condition had the tunnel fans running to measure the noise characteristics of the wind tunnel and the second had the tunnel fans off to measure the ambient noise level in the laboratory. The measured results for each conditions can be seen in figure 4.4. In the data acquired with the fans running, the presence of the fan tones are clearly observed with the fundamental tone occurring at 261 Hz and subsequent harmonic tones at 525 Hz., 728 Hz., etc. These tones have amplitudes ranging from 10 – 15 dB higher than the boundary layer noise. Note that the disturbance above 300 Hz is uniform in amplitude (ignoring the fan tones) which indicates that the noise is due to the boundary layer. Another indication that the broadband noise is due to the boundary layer was the poor coherence between microphones spaced only 2 in. apart in the duct (see figure 4.6). Again, the fan tones are present at the frequencies with the best coherence.

A practical implementation of a smart foam element for controlling turbulent boundary layer noise would more likely utilize accelerometers and not microphones. Figure 4.7 displays the acceleration response of the VPI test panel when excited by the boundary layer. Note that the fan tones are again present in the response. The coherence was checked between accelerometers spaced 2 in. apart (see figure 4.8). The coherence was significantly better than when measured with microphones with the same spacing because the plate works to filter the boundary layer disturbance.

In addition to the 60 in. standard test section previously described, a 48 in. long diffuser with an exiting cross-section of 12 in. x 20 in. was added onto the end of the wind tunnel duct. The purpose of the diffuser section was to slow down the flow and move the point where the wind exits the tunnel further away from the test panel. This was done in an effort to reduce the level noise at the measurement transducers not generated by the boundary layer. Figure 4.9 plots the mean square pressure reductions to the fan tones associated with the addition of the diffuser. The fundamental fan tone was reduced 3.0 dB and the first harmonic was reduced 6 dB.

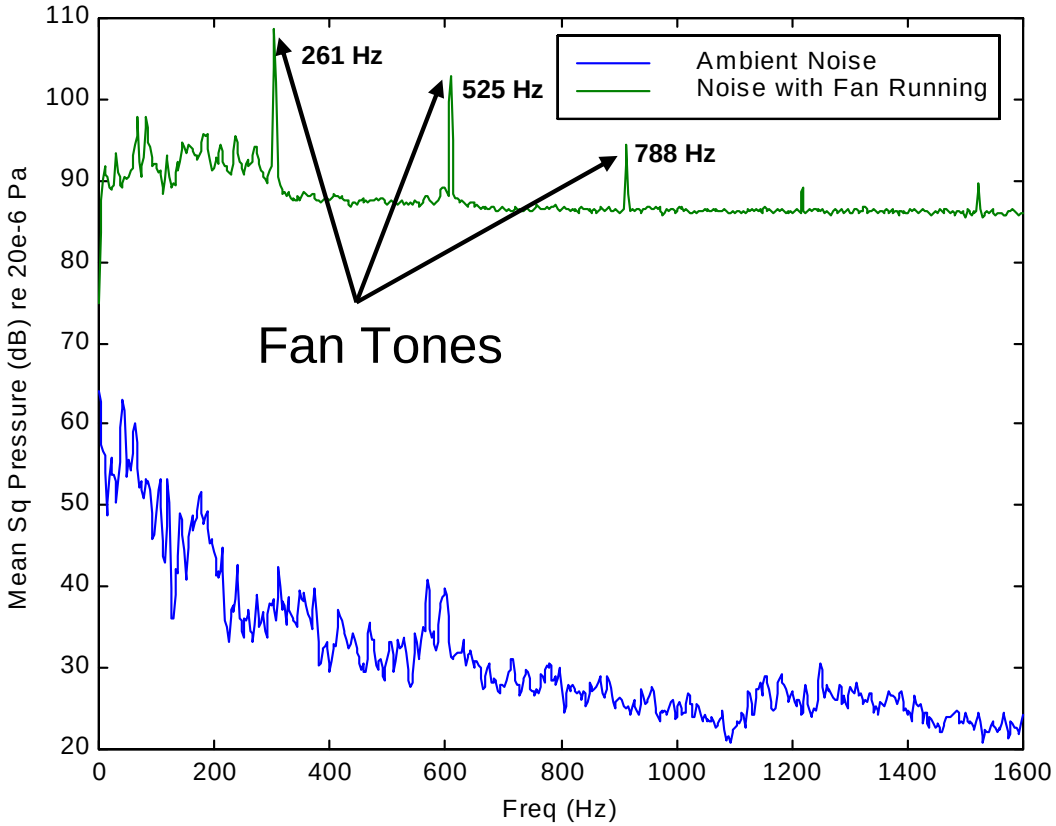

Figure 4.5 VPI wind tunnel noise characteristics.

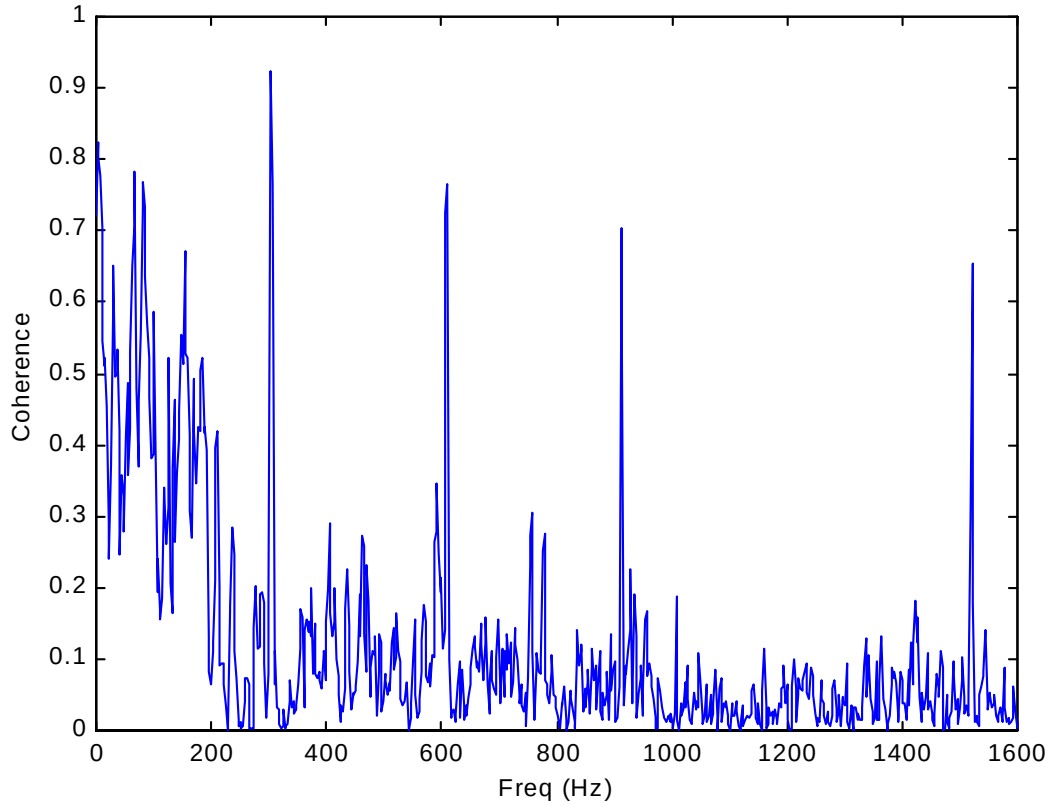

Figure 4.6 Duct coherence between microphones 2 in. horizontally spaced.

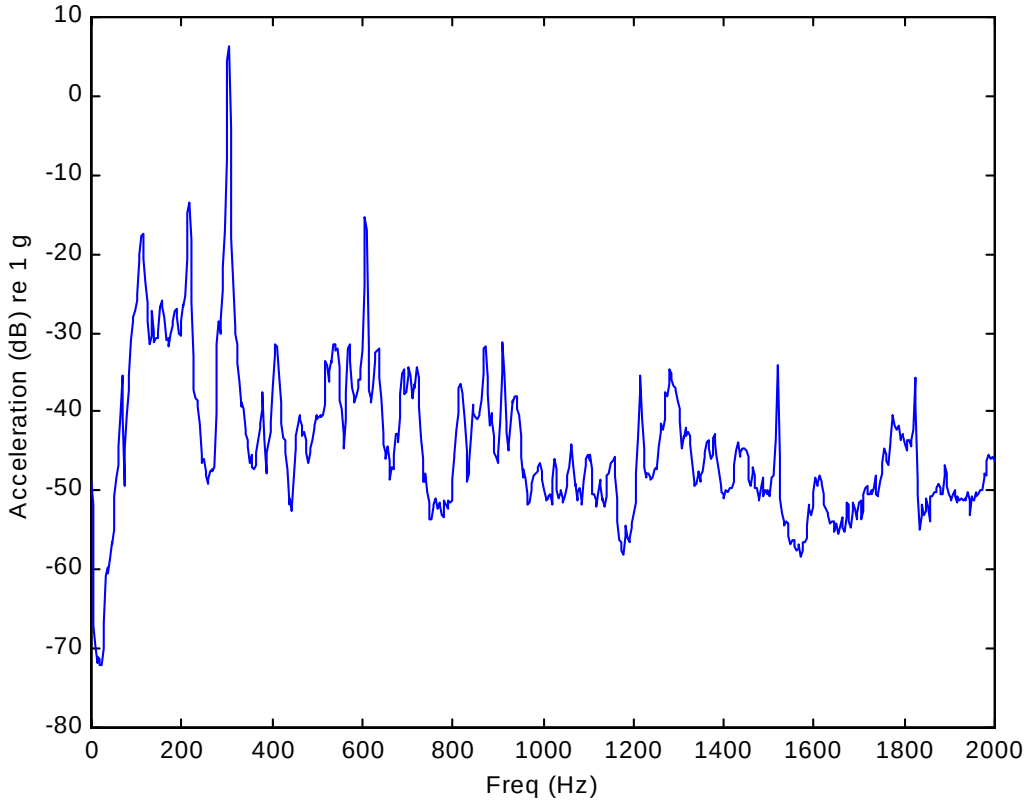

Figure 4.7 VPI test plate accelerometer response characteristics.

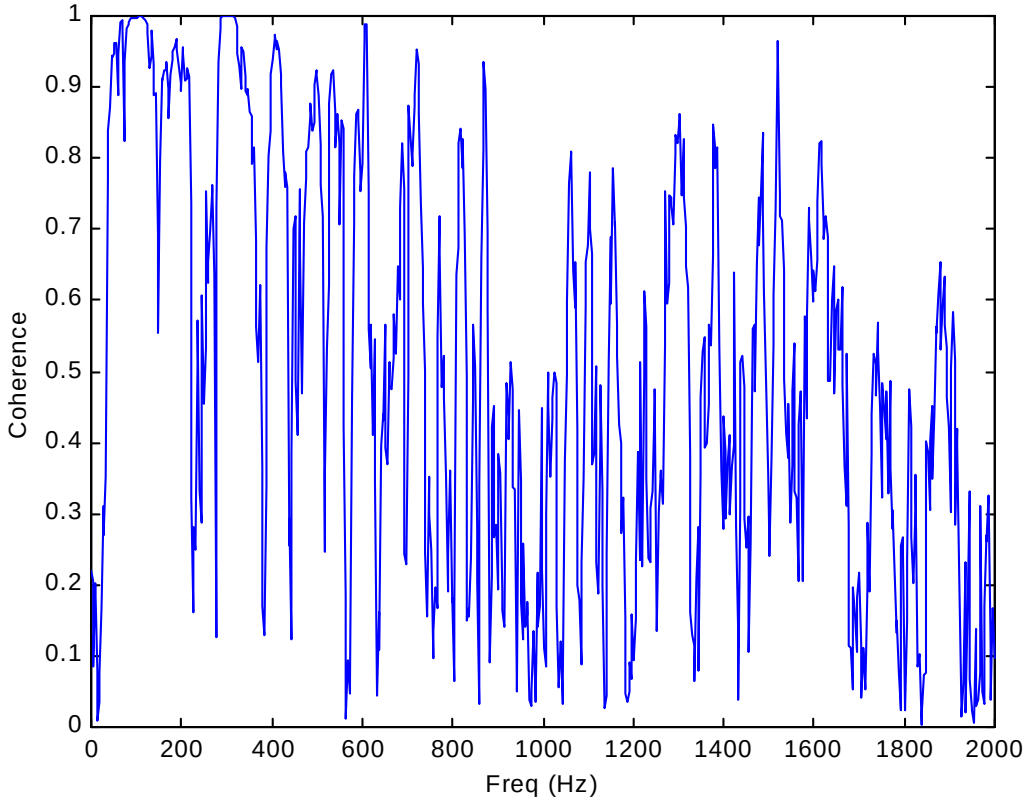

Figure 4.8 VPI plate coherence between accelerometers 2 in. apart.

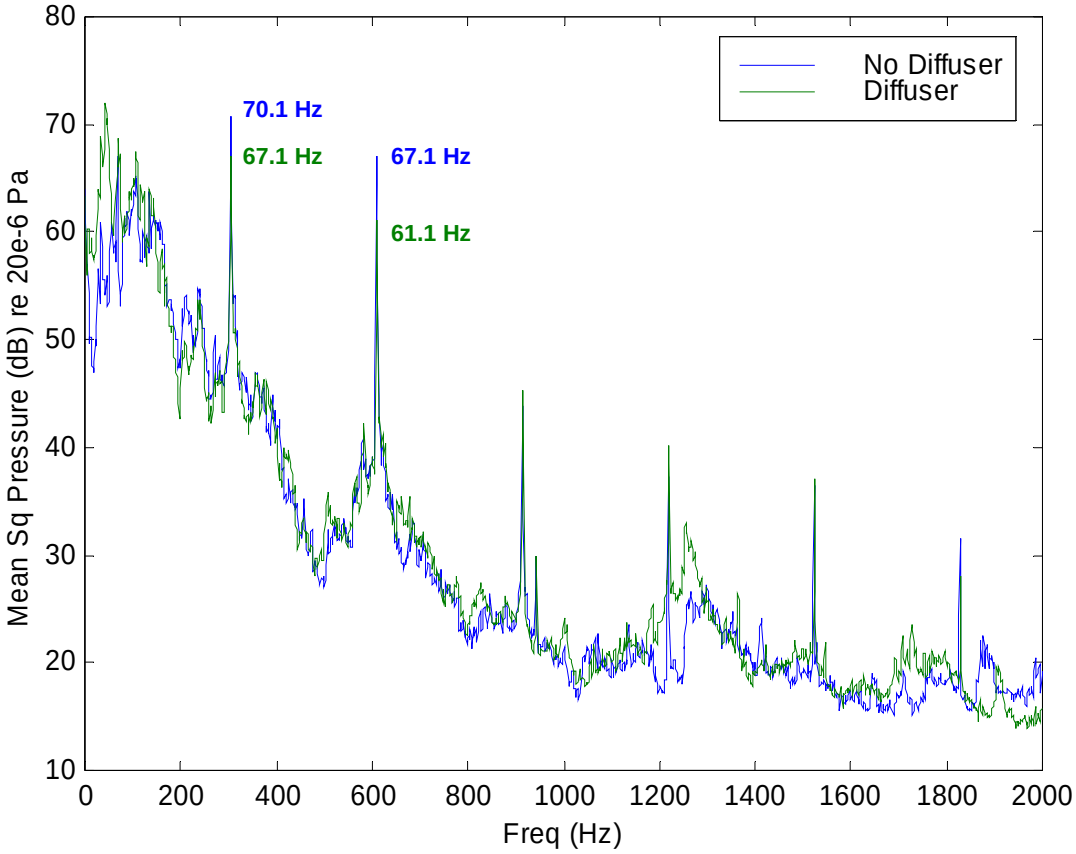

Figure 4.9 Fan tone reduction from diffuser.

Additional effort was made to reduce the fan tone levels with the addition of an array of Herschel-Quincke (HQ) tubes as seen in figure 4.10. HQ tubes are passive noise attenuation devices that have the ability to attenuate the harmonics of a fundamental frequency. The device is a hollow tube with two ends that each attach to the side wall of a main duct with the two ends aligned in the direction of the flow. The incident acoustic wave divides at the first intersection with the HQ tube and recombines with the incident wave downstream. The difference in path length results in a phase shift between the two waves that result in sound attenuation at a select number of frequencies. Factors such as the length of tube, cross-sectional area of the tube, and distance between inlet and outlet openings are all parameters that can be used to tune the performance of a HQ tube. The tuning and implementation of Herschel-Quincke tubes was not a major focus of the project, but with minimal tuning and adjustment the levels of the fan tones were reduced by approximately 4 dB at both the fundamental and first harmonic frequency.

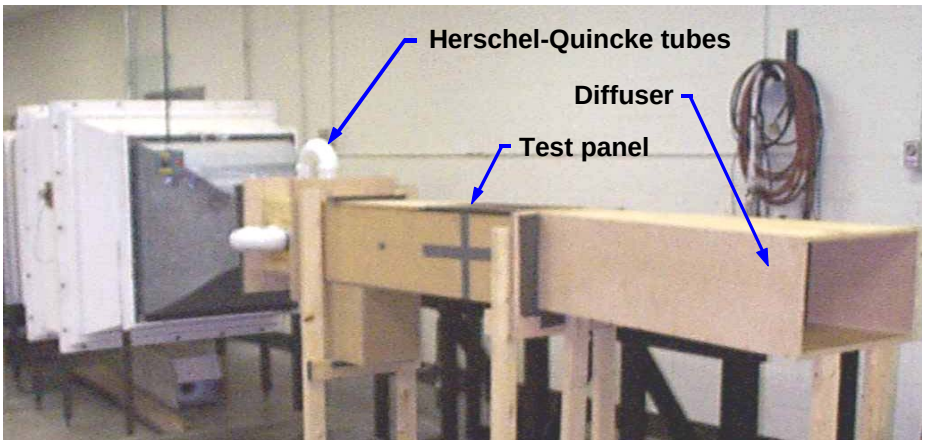

Figure 4.10 VPI wind tunnel test facility.

4.3 ANECHOIC ENCLOSURE

Chapter 3 introduced the filtered-x LMS feedforward control algorithm for the control of turbulent boundary layer noise, which involved the minimization of panel radiation at an array of microphones. In order to achieve control, it was required that the error microphone signals be coherent with the vibration of the panel and isolated from outside disturbances. The obtainable level of control partially depends on how coherent the error signal is with the disturbance. To assure a coherent error signal it was therefore necessary to build an enclosure that minimized the contribution of external noise sources. In addition, the anechoic enclosure loosely represents boundary layer noise radiating into an aircraft interior.

In general, the radiated sound field of a source within an enclosure is comprised of two components: direct-field radiation and reverberant-field radiation. The direct-field radiation is due to sound waves that travel directly from the noise source to the observation point whereas the reverberant field radiation results from sound waves that are reflected from the surfaces of the enclosure. The designed enclosure ideally should be anechoic, which simulates a free-field by minimizing the effects of the reverberant-field and allows for an accurate measurement of radiated sound pressure level throughout its volume. This can be accomplished by lining the inner surfaces of an enclosure with highly absorptive walls often in the form of acoustic wedges. The reflected waves that contribute to the reverberant-field are generated as the incident acoustic waves

experience a sharp change in impedance at the wall of the enclosure. A foam surface treatment in the shape of a wedge (similar to anechoic test chambers) helps to absorb the incident acoustic waves and also minimize the impedance differential between the room and the enclosure surface. In addition to minimizing the reverberant field, the anechoic enclosure must also prevent outside noise sources from passing through the enclosure walls and corrupting the microphone signals. The attenuation of the signal as it passes through the panels, that make up the enclosure, or transmission loss (TL), is established by the mass and stiffness of the material used in the panel's construction and the frequency of the disturbance.

4.3.1 Construction

An anechoic enclosure was designed for use in the turbulent boundary layer control experiments. An ideal anechoic enclosure would be large in size, contain thick dense walls, and lined with large absorbent acoustic wedges. Size was a restriction, however, due to the space limitations at each of the three testing facilities. Also, because it was required to repetitiously move the enclosure in and out of position, the weight of the enclosure needed to be limited to a manageable value. A balance between the size and weight of the enclosure's panels was required since each affects the attenuating properties of the enclosure. Weight can be sacrificed for thickness, provided that the thickness of the panel exceeds one-fourth of the wavelength of the incident wave [50]. A schematic showing the design of the anechoic box can be seen in figure 4.11. The walls of the enclosure were fabricated from two thicknesses of 3/4 in. plywood lightly tacked together forming a total wall thickness of 1-1/2 in. The walls were only lightly tacked to each other because relative motion between the panels will result in a loss of vibrational energy. Glue was used to anchor the corner joints and 3 in. wood screws were used to pull the corners tight together. Both the interior and exterior seams were then sealed airtight with caulk thus eliminating all air gaps. The interior dimensions of the enclosure were 36 in. long, 24 in. wide, and 24 in. deep. An opening was cut in the center of one of the 36 in. x 24 in. sides of the enclosure to allow for the panel radiation to enter the box. To allow access to the control components used in the experiments, the 36 in. x 24 in. enclosure wall opposite the radiating panel was designed to be removable. The panel was

sealed with 1/2 in. wide and 1/2 in. thick airtight foam tape and held closed with six compression latches during tunnel operation.

Structural excitation of the anechoic enclosure induced through contact with the vibrating wind tunnel would introduce additional noise into the system. Two strips of the same 1/2 in. wide and 1/2 in. thick foam tape were positioned around the panel opening between the wall of the wind tunnel and anechoic box as an attempt to isolate the tunnel vibration. Accelerometers were mounted to the enclosure and the wind tunnel and the relative vibration levels were compared. It was concluded that the vibration transmission was sufficiently low as to not induce an additional noise source of any significance. The interior walls of the enclosure were lined with SONEXsuper™ wedges made from wiltec®, a lightweight, semi-flexible, low-density foam [51]. Each foam block measured 12 in. square and contained three 6 in. wedges. The wedge squares were arranged in an alternating pattern, as is conventional in anechoic enclosure design, and were mitered to fit snug within each corner so that the entire interior surface was coated with the acoustic material.

4.3.2 Characterization

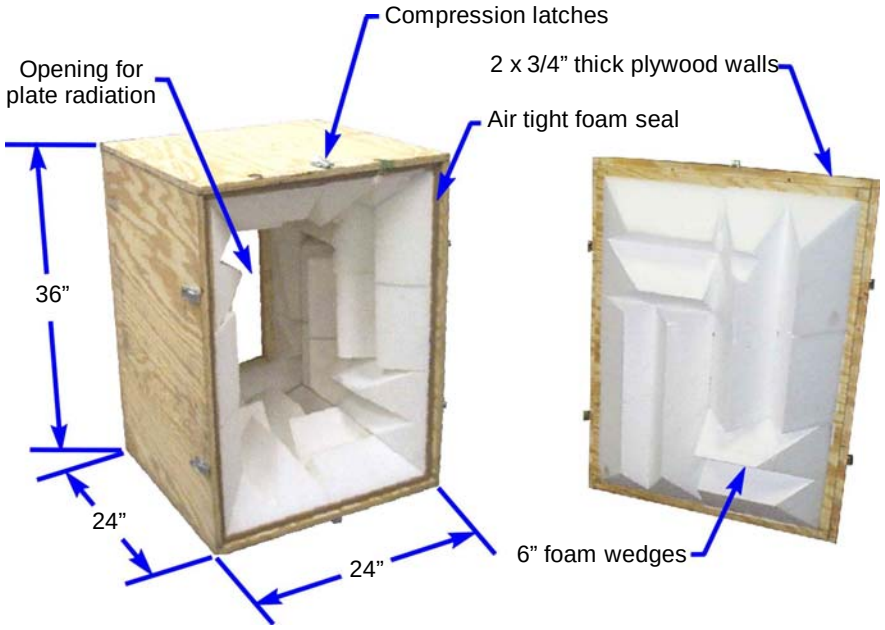

Figure 4.11 Anechoic enclosure.

4.3.2.1 Reverberation

An effort was made to characterize the reverberant properties of the anechoic enclosure designed for the turbulent boundary layer experiments. The enclosure was placed within a larger anechoic chamber located in the Vibration and Acoustics Laboratories (VAL) at VPI. A speaker was placed in the enclosure and five microphones were evenly spaced on a line running diagonally across the interior of the enclosure approximately 18 in. above the speaker and parallel to the floor. The speaker was driven with random noise and the responses measured by the microphones were recorded. The anechoic enclosure was removed and the speaker and microphones were left in the same relative positions. The speaker was again driven and the microphone responses were recorded. The five microphone responses were averaged and the FRF magnitude was calculated for each case. Figure 4.12 shows a comparison between the two systems. Note that above 700 Hz the two systems behave virtually the same, which means that the sound pressure measured within the anechoic enclosure above this frequency will not be biased due to contributions from the reverberant field. In the low frequency region (below 200 Hz) there was a larger response with the anechoic enclosure in place since the box's presence reduces the volume of the sound field surrounding the microphone array. The low frequency noise has a more significant effect on the overall pressure levels within the enclosed space due to the reduced volume. There also exists a discrepancy in the two signals between 200 Hz and 700 Hz. This difference was caused by resonant behavior in the anechoic box and will effect the signal measured by the error microphones during control. The error microphone signals in this frequency range will not reflect the true SPL radiated from the panel but will contain some contribution due to the reverberant field. Thus, the reverberant field radiation if it is in-phase with the direct field radiation will increase the SPL at the microphones and if out-of-phase will decrease the SPL. In both cases bias error will occur. This will not prevent the feedforward control algorithm from controlling the sound radiation, however, the true SPL due to the turbulent boundary layer excitation cannot be determined with certainty.

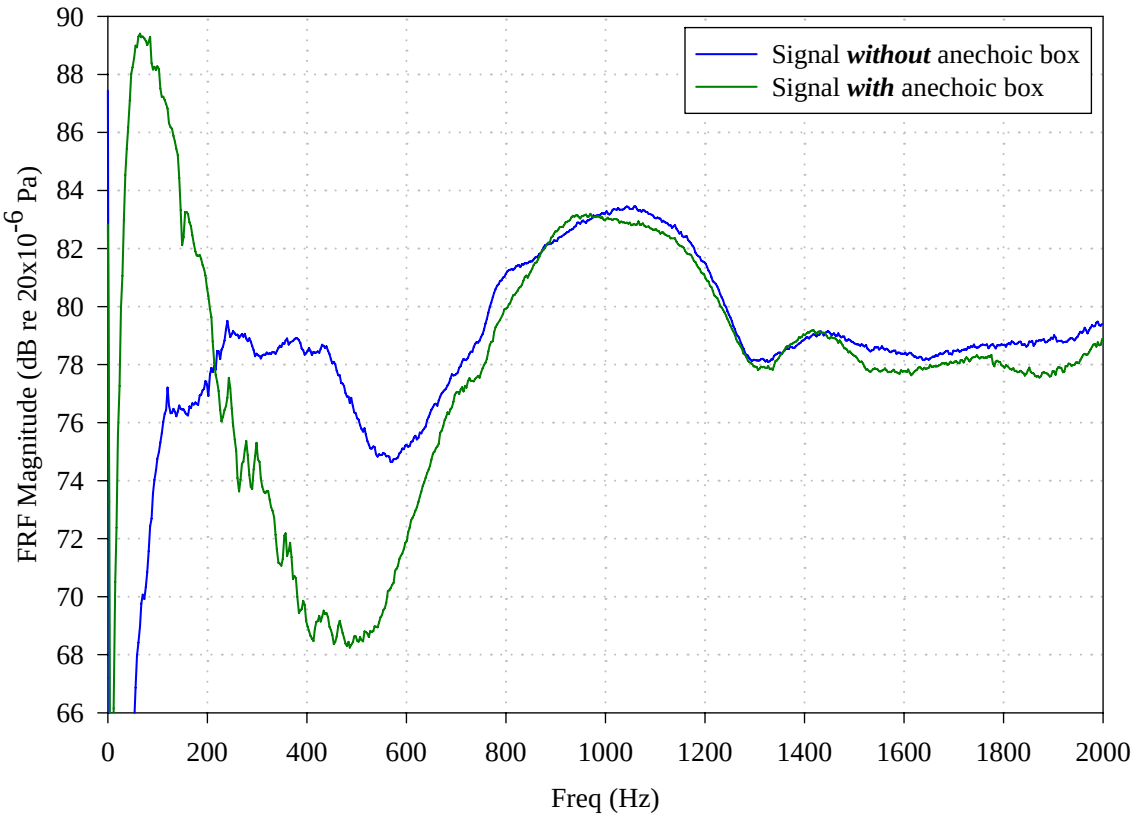

Figure 4.12 Resonant behavior of anechoic enclosure.

4.3.2.2 Noise Reduction

In addition to quantifying the resonant behavior of the anechoic box, the ability to prevent the infiltration of an outside noise source through the enclosure was also characterized. A reverberation chamber located at VPI was used to measure the noise reduction (NR) of the enclosure. Reverberation chambers are designed to closely approximate a diffuse sound field, which is defined when the mean square pressure amplitude of any traveling plane wave is on average the same, independent of direction [52]. Similar to the experiments for measuring the resonant characteristics of the enclosure, five microphones were evenly spaced on a line running diagonally across the interior of the enclosure parallel to the floor. The anechoic enclosure was placed in the center of the reverberation chamber floor with the same airtight seal used when mounting the box to the wind tunnel. The disturbance speaker was positioned in the corner of the

reverberation chamber in order to maximize its radiation efficiency. The SPL's were recorded with and without the anechoic box in place and can be seen in figure 4.13(a). The difference in the two traces was the NR induced by the anechoic enclosure and is displayed in third-octave bands in figure 4.13(b). Note the increase in NR at the higher frequencies. This occurs because the NR of an enclosure is a function of not only the mass and thickness of the panels that make up the enclosure but also the frequency of the disturbance.

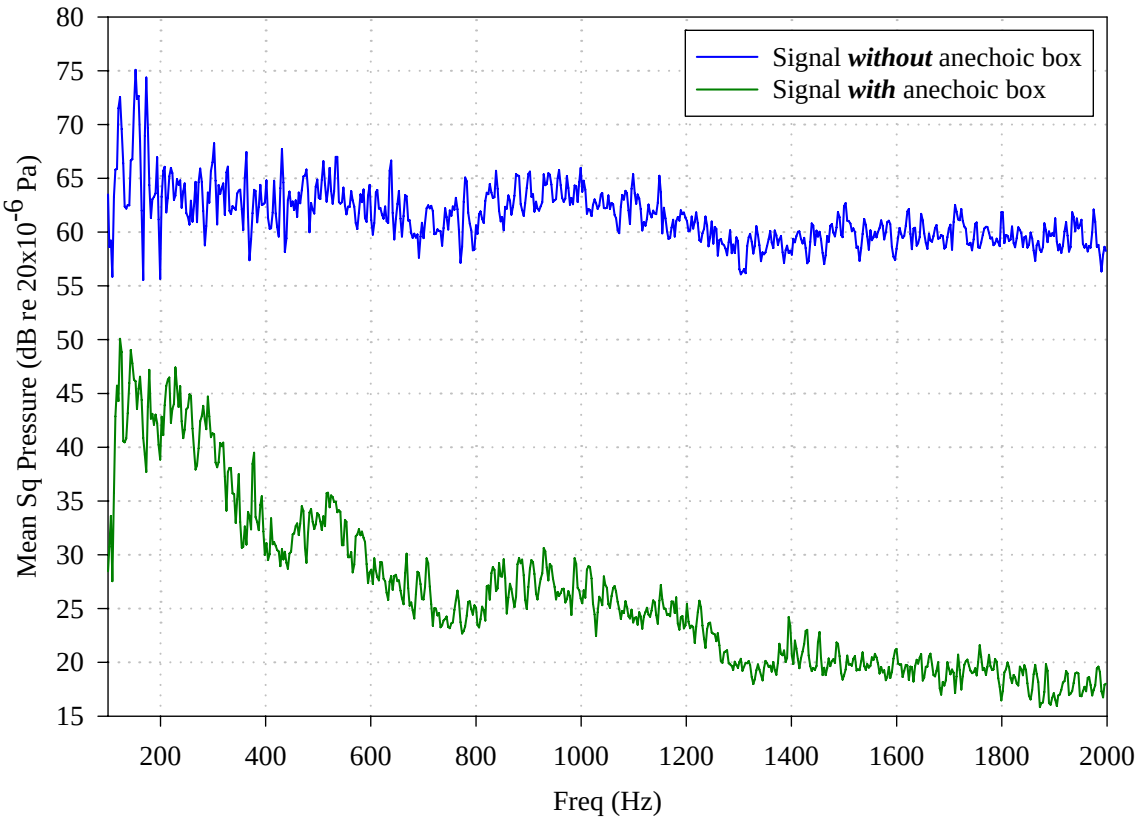

(a)

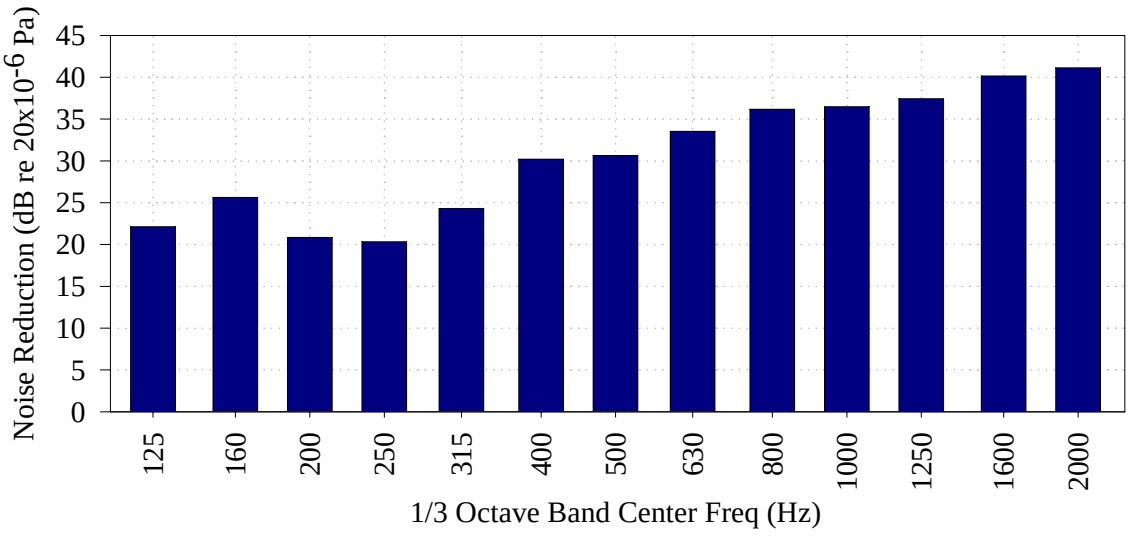

(b)

Figure 4.13 Noise reduction of anechoic enclosure. (a) Microphone response. (b) Noise reduction levels.

Chapter 5

Experimental Results

5.1 INTRODUCTION

It has been the goal of this research to demonstrate the active control of sound radiation from a panel that has been excited with a turbulent boundary layer disturbance. The Structural Acoustics Branch of the NASA Langley Research Center (LaRC) has funded this work as part of a subprogram of the Advanced Subsonic Technology noise reduction program concerned with interior noise. Historically, much of the work in the area of aircraft interior noise has been focused on passive treatments and active control techniques that utilize speakers or input forces as control sources (see Chapter 1). These techniques are often characterized as point approaches since the interaction between the control elements and noise source is localized. Recognizing the limitations of these noise control methods has prompted researchers to consider new control techniques that take advantage of both passive and active control components. The hybrid, active/passive technique of smart foam used in this research (see Chapter 2) is considered a smart skin or a fully distributed noise control approach since the entire noise source is treated with the combined active and passive elements of the device. Smart foam is just one of the many methods being examined for controlling the aircraft interior noise problem.

The present smart foam project has been conducted in parallel with a separate NASA LaRC project also tasked with the active control of turbulent boundary layer noise using piezoceramic actuators attached to a panel. Together these two project interests helped to determine the timetable and operating conditions for each set of experiments.

This timetable for experiments was also dependent on the availability of the wind tunnel test facilities.

The smart foam experiments were performed using three wind tunnel test facilities. Operating speeds and locations of these wind tunnel facilities are summarized in table 5.1. The VPI wind tunnel is a much smaller and more unrefined than the tunnels at both NASA and AEDC. The VPI tunnel, due to its accessibility and minimal time restrictions on its use, was utilized extensively to help prepare for the tests performed at NASA LaRC and AEDC. It should also be noted that research is a continual learning and iterative process in which new knowledge is obtained from each set of experiments performed. Consequently, knowledge learned from a set of experiments if applied to previous experiments could have possibly improved the results obtained in those tests. Ideally, the previously conducted experiments should be repeated incorporating the improvements, however, due to a finite amount of time and funding this was not feasible for this project.

It is the purpose of this chapter to present the results obtained for the turbulent boundary layer noise control experiments using smart foam. This chapter first presents details regarding the acquisition sensors used in all of the experiments. The remainder of the chapter is organized according to testing location with the NASA presented first, AECD experiments second, and finally the VPI experiments. Each test section contains a detailed description of the testing facility and specifics related to sensor and actuator locations as well as the specific controller parameters used for the tests. The sections conclude with the results obtained for that set of experiments.

Table 5.1 Wind tunnels.

Wind tunnel	Location	Test Speed
Mechanical Engineering Department - Virginia Polytechnic Institute and State University (VPI)	Blacksburg, Virginia	Mach 0.1
Structural Acoustic Branch - NASA Langley Research Center (LaRC)	Hampton, Virginia	Mach 0.2
Arnold Engineering Development Center (AEDC) - Arnold Air Force Base	Tullahoma, Tennessee	Mach 0.8 Mach 2.5

5.2 ACQUISITION SENSORS

Chapter 3 presented the multi-channel filtered-x LMS feedforward control algorithm used in the smart foam turbulent boundary layer experiments. This methodology can be used to generate multiple control signals based on information supplied by arrays of both error and reference signals. This section will provide specifics regarding the transducers chosen to serve as error and reference signals and the reason each type was chosen. The transducers that were used as error and reference signals were common to all experiments performed at each of the three test locations. Characteristics specific to each set of experiments will be presented in the measurement setup section for each test location.

As discussed in Chapter 2, the output signal of the system plant is the summation of both the actual disturbance signal and the secondary actuator signals generated by the controller. It is the goal of the controller to adjust the magnitude and phase of the secondary control signal so that by superposition the error signal is minimized. For the smart foam experiments performed in this research, the error signals were generated using microphones. Microphones were chosen as the minimization criteria because it was the principal goal of the work to reduce the interior cabin noise perceived by an aircraft crew. PCB Acousticel microphones (Model TMS-130B) connected to a PCB Acousticel signal conditioner (573 Series) were used in all experiments.

In the filtered-x LMS feedforward control algorithm the reference signals are used to provide the controller with knowledge of the disturbance. PCB piezoelectric ICP accelerometers (Model 352A10) were used for all experiments and mounted directly to the test panel surface. Each accelerometer weighed approximately 0.7 grams making the combined weight of all reference accelerometers only 0.6% of the NASA and VPI test panel weight and 1% of the AECD test panel weight. These percentages are based on the weight of the panel test section exclusively and do not include the weight of the stringers and frames used to stiffen the NASA & AEDC test panels. Each accelerometer was connected to a twelve-channel PCB signal conditioner (Model 483B07) with adjustable gains for each channel that were set in order to take advantage of the dynamic range of the input A/D converters. Accelerometers were chosen because the controller requires sufficient time advance in order to determine and induce the secondary control signals

into the system in phase with the primary disturbance. Direct panel vibration provides the most time advance since upstream flow measurements are not possible in an aircraft and due to the unpredictable nature of a turbulent boundary layer disturbance.

5.3 NASA LARC LOW SPEED EXPERIMENTS

5.3.1 Test panel

An aircraft fuselage section was designed and built by Boeing Aircraft Company and shipped to NASA LaRC to be used in the experiments demonstrating the active control of turbulent boundary layer noise. The panel was made from a 60 in. long, 20 in. wide, and 0.060 in. thick panel of T6 aluminum and was mounted within a steel frame designed to form a continuous clamped boundary condition on all edges. The frame was also designed so that the panel could be placed in tension in the 20 in. dimension and strain gauges were used to verify an applied strain of 414 lb./in. Tension applied to the panel increases the stiffness and therefore reduces the modal density of the panel by shifting the panel resonances to higher frequencies. This is also representative of an aircraft under certain flight conditions since cabin pressurization causes tension in the fuselage panels. The panel was also reinforced with two vertical stiffeners and a single longitudinal stiffener, which are often referred to as frames and stringers, respectively. The frames were nominally spaced with 20 in. between supports and the stringer was centered on the panel sectioning the panel into six equal size bays (see figure 5.1). Accounting for the widths of the stringers and frames, the size of the radiating surface of the lower center

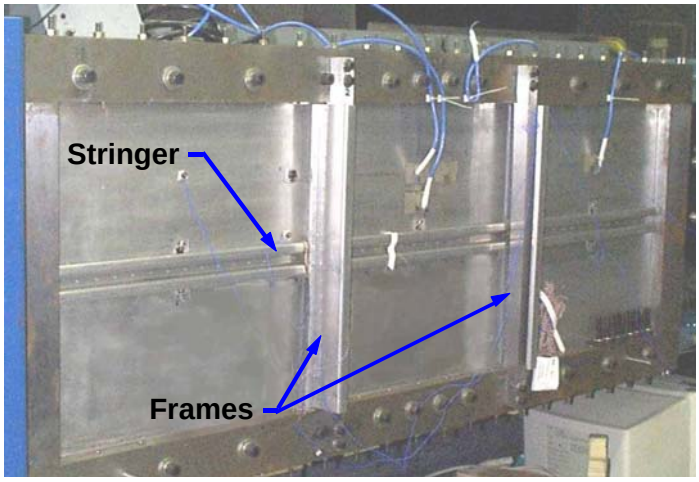

Figure 5.1 NASA LaRC test panel.

test section was 18.5 in. x 9 in. (i.e. one sixth of the panel). Care was taken in the construction of the frames and stringers as well as their attachment to best approximate the panel radiation of an actual aircraft system.

Engineers at NASA LaRC also performed an experimental modal analysis of the top center section of the test panel. The modal survey was performed using an impact hammer at forty-five locations evenly distributed with approximately 2 in. spacing in both the longitudinal and horizontal directions. Three fixed response accelerometers were positioned on the top center bay as well as a single accelerometer centered on each of the other five panel bays. A ratio of the acceleration response measured by the accelerometers to the input force supplied by the modal hammer at the fourty-five input locations was acquired (i.e. frequency response function data). The data was analyzed using the STAR modal analysis software and is presented in table 5.2 along with the theoretical predictions. The experimental mode shapes can be seen in the Appendix.

Table 5.2 Modal analysis of the top center bay of the NASA LaRC test panel.

Mode*	Theoretical Frequencies (Hz)	Experimental Frequencies (Hz)
(1,1)	319.2	275.5
(1,2)	362.8	349.4
(1,3)	436.6	442.8
(1,4)	540.5	553.4
(2.1)	656.3	581.3
(1,5)	674.3	650.9
(2,2)	687.9	678.0
(2,3)	743.3	767.9
(2,4)	825.2	**
(1,6)	837.4	**
(2,5)	936.0	**

Note: (*) Mode (m,n) corresponds to “m” half-wavelengths along the 10” dimension and “n” half-wavelengths along the 20” dimension.

(**) Not experimentally verified possibly due to insufficient spatial resolution

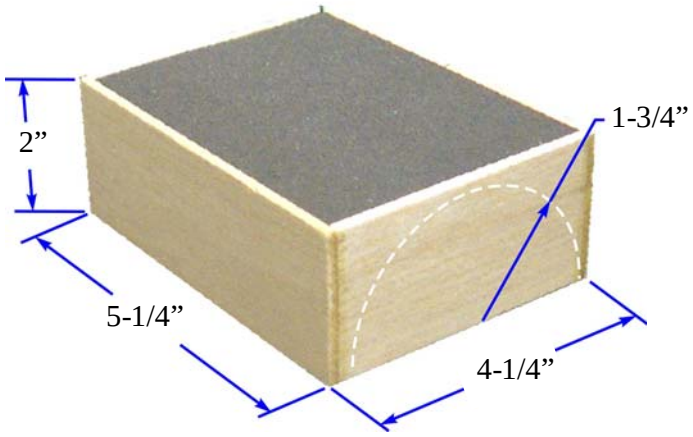

Figure 5.2 Actuator used in NASA LaRC experiments.

5.3.2 Measurement setup

5.3.2.1 Actuators

Custom smart foam actuators were designed and manufactured for use in the NASA wind tunnel experiments according to the procedure outlined in Chapter 2. Specific design characteristics for the smart foam actuators are shown in figure 5.2. Six identical actuators were positioned in a 2 x 3 array on the bottom center section of the panel as depicted in figure 5.3. The dimensional properties of each actuator as well as the number of actuators used in the experiments were based on the size of the panel section and its modal behavior. It is noted from table 5.2 that the first higher order panel mode in the 10 in. dimension for the center section is the (2,1) mode occurring at 581 Hz. These higher order panel modes occur within the control bandwidth and therefore two rows of actuators were implemented in the 10 in. direction. The two actuator rows allowed the controller to have control authority over these higher order modes. In like manner, three rows of actuators are implemented in the 20 in. direction. The gaps between the actuators are filled with strips of the same acoustic foam used to create the smart foam cells such that the entire center panel section was acoustically treated. All of the foam was held in place on the panel using a spray adhesive. Gluing the balsa frame to the structure was discussed in Chapter 2 as a method of improving the performance of a smart foam actuator. This improvement was not developed until after the NASA experiments.

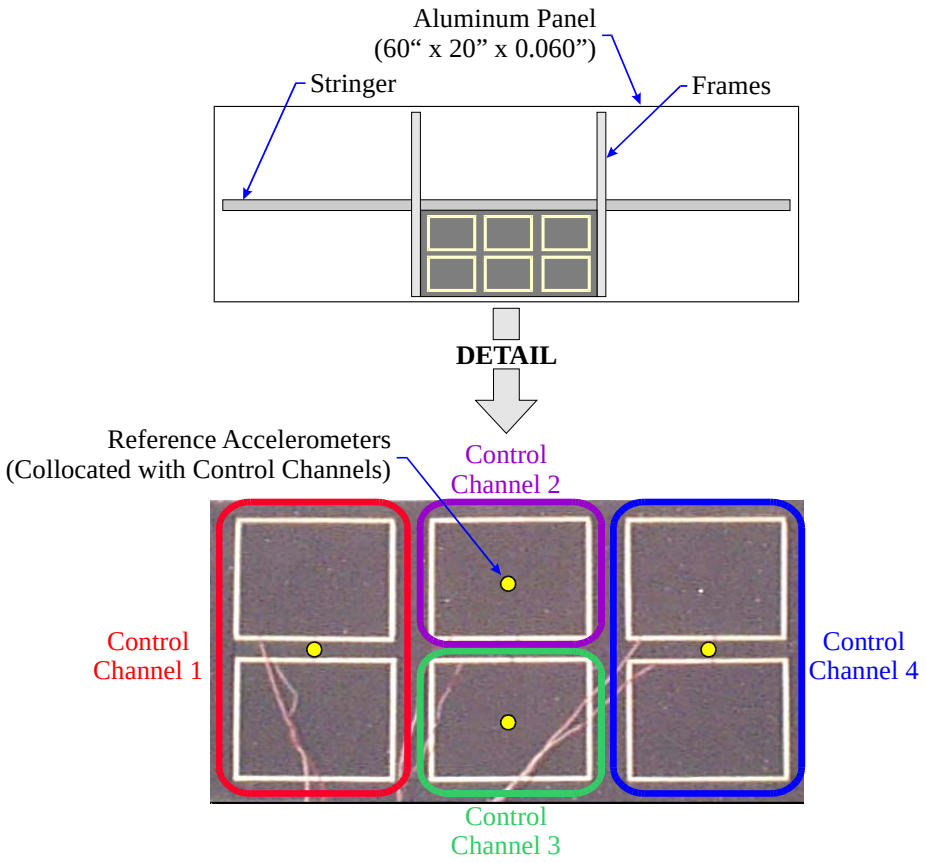

Figure 5.3 NASA LaRC actuator configuration.

Although six actuators were mounted to the panel in the experiments, two sets of two actuators were wired in phase creating a total of four actuator channels as depicted in figure 5.3. The actuator channels were confined to four due to limitations in the speed of the digital signal processor (DSP). Note that the multi-channel controller has been designed such that all of the actuators will be driven in phase should that be required to control a particular panel mode. The control signals leaving the DSP were amplified using a ±200 V and 100 mA PCB power amplifier (790 Series). In addition, the output signals were low-pass filtered at 1000 Hz using Ithaco 24 dB/octave filters (Model 4302) in order to eliminate the high-frequency content introduced by the D/A converters.

5.3.2.2 Error Microphones

The anechoic enclosure described in Chapter 4 was used to isolate the panel radiation from the other noise sources present. See section 5.3.3 for specific details of mounting

the anechoic enclosure. Four error microphones were located within the anechoic box along the midpoint of each panel edge suspended approximately 20 in. above the panel. The controller functions by attempting to reduce the radiated sound pressure only at the error microphones, which can sometimes result in an increase in sound pressure at other locations. To help monitor the global performance of the controller an additional four microphones were also distributed 20 in. above the panel in the anechoic box. The confined physical size of the anechoic enclosure and test facility prevented the use of additional monitoring microphones.

The poor sound radiation characteristic of a smart foam cell at low frequencies was addressed in Chapter 2 where the typical radiated sound power of an actuator used in the NASA LaRC experiments was shown (Small Actuator curve of figure 2.9(a)). The radiation characteristics of the actuators coupled with the modal properties of the panel were used to determine the frequency range for control. It was necessary to remove the low frequency radiation content from the error signals in order to prevent the controller from driving the actuators in this range, where they have no control authority. If the control system was allowed to drive the actuators where they were incapable of generating sufficient sound power (see Chapter 2), then the control system became unstable and needed to be reset. The lowest frequency that could be tolerated by the control system was both a function of the radiation characteristic of the smart foam and the noise content. The value where the instability occurred varied for each test, but typically the low value of each control band was the lowest frequency that could be tolerated by the control system. Also, due to the inherent active/passive properties of the smart foam, the high frequency radiation content was removed (i.e. where the passive attenuation properties of the smart foam work well). This was accomplished by band-pass filtering each error channel with two Ithaco filters (Model 4302) connected in series. The control bandwidth for the NASA LaRC experiments was set to be 400 – 1000 Hz.

5.3.2.3 Reference Accelerometers

The reference signals required for control were provided by four fixed response accelerometers mounted to the surface of the panel. Again, four was the maximum number of possible references due to the speed limitations of the DSP. As discussed in

Chapter 3, the maximum level of control depends partially on the multiple coherence function between the reference and error sensors. Data was acquired for the panel section instrumented with eight accelerometers and excited by the turbulent boundary layer disturbance. The multiple coherence functions were calculated between each of the four error sensors for various groupings of four accelerometers. The coherence levels of these groupings were compared and used to establish the reference sensor locations used in the control experiments. Figure 5.4 shows the multiple coherence function between a single error microphone with the four reference accelerometers collocated with the center of each control channel (see figure 5.3). These accelerometer locations were chosen because they provide the controller a high coherence signal across the majority of the control bandwidth at each of the error sensors. The fact that the coherence tends to drops off at the higher frequencies was not of much concern since, as will be seen later, the passive attenuation properties of the smart foam increase with frequency. Each reference channel was also low-pass filtered at 1000 Hz using an Ithaco filter (Model 4302).

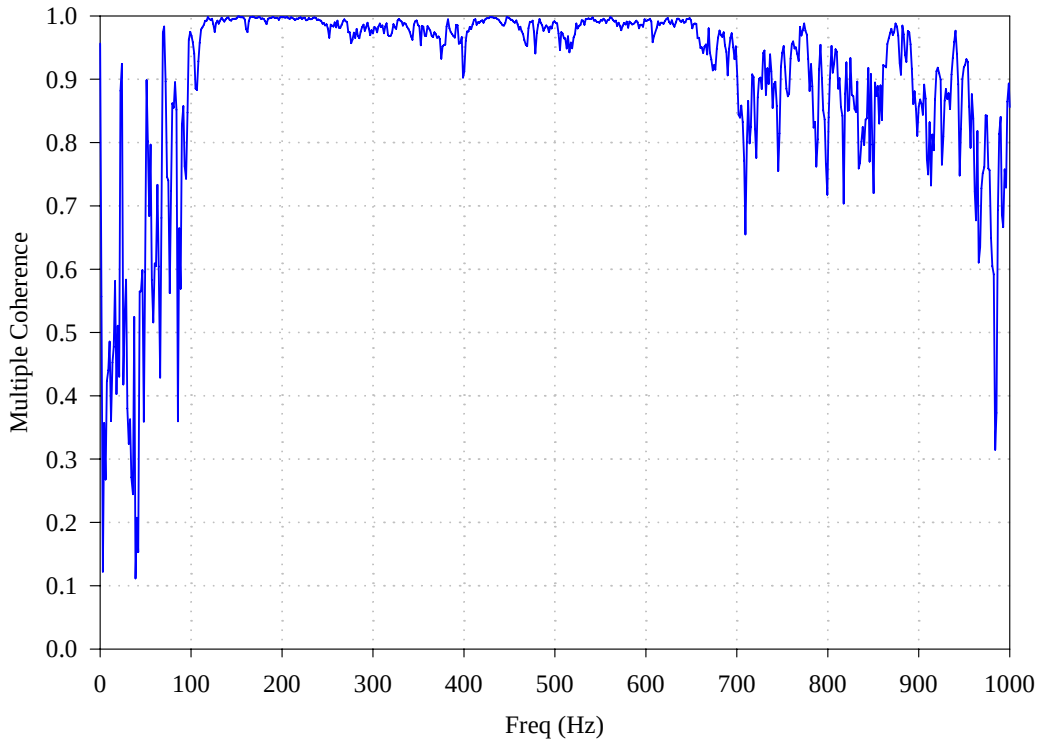

Figure 5.4 Multiple coherence of NASA LaRC panel.

5.3.2.4 Controller

Chapter 3 described the multi-channel filtered-x LMS feedforward controller and a LabVIEW® interface program developed by VPI. The program was designed generically so that specific control parameters could be selected based on the requirements of each set of experiments. The control parameters selected for the NASA experiments are summarized in table 5.3. The target active control bandwidth was used to determine the necessary sampling frequency required to prevent aliasing. The control bandwidth was selected to be 400 – 1000 Hz and thus the sampling frequency of the controller was set at 3000 Hz (i.e. three times higher than the 1000 Hz value in the control bandwidth). The processing limitations of the DSP are a function of the parameters selected in the experiments, consequently, the number of actuators, references, and errors, as well as the sampling frequency, dictated the number of system ID and the control path coefficients available for selection. During system ID, the controller drives each actuator individually and models the transfer functions between each actuator and all of the error sensors. The number of system ID coefficients selected determines the length of the FIR filters used to model these transfer functions. Fewer system ID coefficients (26) were required to obtain an accurate model since the system (actuator to microphone) did not contain any highly reverberant components. This was partly due to the acoustic wedges designed to reduce the reverberant properties of the anechoic enclosure. The number of control path coefficients sets the lengths of the adaptive FIR filters that are updated by the LMS algorithm and used to generate the secondary control signals. The control path

Table 5.3 Control parameters for NASA LaRC experiments.

Controller Parameters	Value
Number of Actuators	4
Number of error sensors	4
Number of reference sensors	4
Sampling frequency	3000 Hz
System ID coefficients	26
Control path coefficients	190

coefficients were selected to be 190 since a higher number of control path coefficients allows for better frequency resolution in the modeling of more resonant systems. In this case the transfer function included the plate dynamics. This was the largest value allowed by the controller taking into account the previously set parameters and the processing limitations of the DSP.

5.3.2.5 Data Acquisition

A data acquisition system, separate from the controller, was used to record performance data during the experiments. This system consisted of National Instruments SCXI 1140 and 1141 modules within a SCXI 1000 DC chassis. The SCXI modules simultaneously sample and hold each signal and contain anti-aliasing filters for each channel. The data was fed to a portable PC using a National Instruments PCI-MIO-16E-4 sixteen-channel data acquisition card and was acquired using programs created in LabVIEW® by VPI. The programs require the user to input the number of data channels, the sampling frequency, and the highest frequency of interest (should be one-third of sampling frequency to prevent aliasing). The results presented for all of the NASA experiments are based on the measured sound pressure levels at an array of eight microphones. The data was sampled at 6000 Hz so that a maximum frequency of 2000 Hz could be observed.

5.3.3 Results

The general concept in the design of the turbulent boundary layer control experiments using smart foam is summarized in figure 5.5 for the Mach 0.2 NASA LaRC wind tunnel test facility. In summary, four control channels comprised of six smart foam actuators were mounted to a single section of the six-bay panel and excited by the tunnel flow. A multi-channel filtered-x LMS feedforward controller referenced the disturbance using four accelerometers mounted to the panel and minimized the radiated sound pressure levels at four error microphones. An anechoic enclosure was necessary to isolate the panel radiation from surrounding noise sources and model an aircraft interior. Figure 5.6(a) is a picture of the NASA LaRC panel with all of the actuators mounted to the

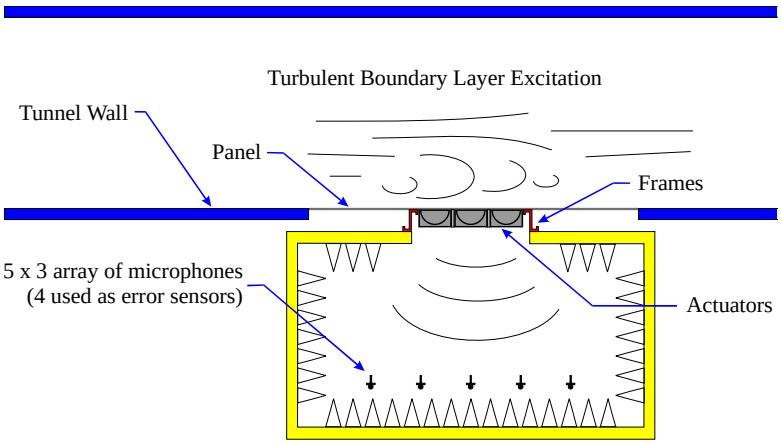

Figure 5.5 Schematic of experimental setup.

panel. The frame surrounding the actuators was designed to allow the anechoic box to seal around the center panel bay, isolating the panel radiation while not restricting the panel motion. Figure 5.6(b) is a detail view of the actuators with control channel two removed to show the placement of the reference accelerometer. Figure 5.7 shows the fully instrumented test panel with the anechoic enclosure in place.

As previously discussed, smart foam actuators attenuate high frequency content due to the passive properties of the acoustic foam and attenuate low frequencies by driving an imbedded piezoelectric layer. It was therefore important to independently measure the contribution of the passive and active elements of the smart foam. First, the radiated sound pressure of the bare panel, containing no acoustic treatment, was measured to establish a baseline for evaluating the control performance. Second, the panel section was treated with the smart foam actuators and the radiated sound pressure

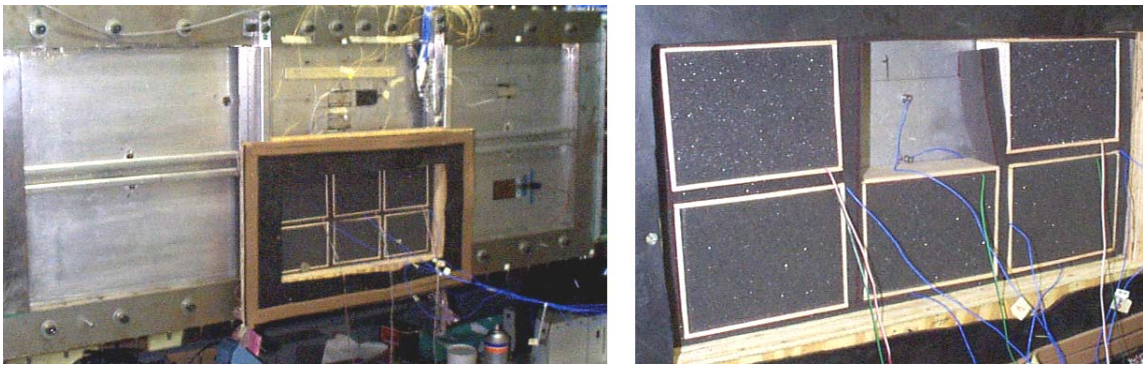

(a) (b)

Figure 5.6 (a) NASA LaRC six-bay panel with smart foam actuators mounted to test section. (b) View of reference accelerometer centered on control channel 2.

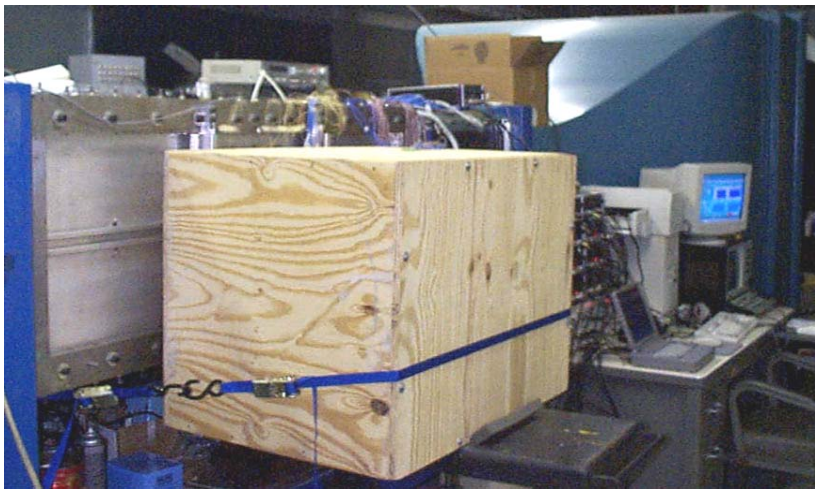

Figure 5.7 NASA LaRC panel with anechoic enclosure mounted in place.

was again acquired. The purpose of this acquisition was to evaluate the passive attenuation performance of the treatment, therefore, the embedded piezoelectric actuators were not driven. The final acquisition measured the combined active and passive attenuation properties of the smart foam treatment by actively targeting the radiated sound pressure in the 400 – 1000 Hz bandwidth. The global control performance of each acquisition was evaluated by calculating the mean square pressure of all eight microphones. Since the goal of the project was to reduce aircraft cabin noise, the results were A-weighted to account for the inefficiencies of the human ear in perceiving low frequency noise. Figure 5.8 displays the results obtained from these control experiments.

Various observations are made regarding the performance of the smart foam actuators. It is observed that there are two separate attenuation mechanisms that can be attributed to the passive properties of the foam. First, the foam works as an absorber, through which acoustic energy is dissipated, especially at the higher frequencies (see Chapter 2). Second, the smart foam cells add damping to the plate system, which accounts for the attenuation at the lower order modes. This is clearly observed at the 186 Hz peak, which corresponds to a lower order mode of the entire six-bay panel. Figure 5.8(b) is a detail view of the control bandwidth where the additional contribution from the active component is observed. Note how the controller was successful in flattening the response above 500 Hz however was unable to contribute from 400 – 500 Hz. This lack of performance within this band can be attributed to the poor radiation efficiency of the actuators in the low frequency region. The same results are presented in terms of

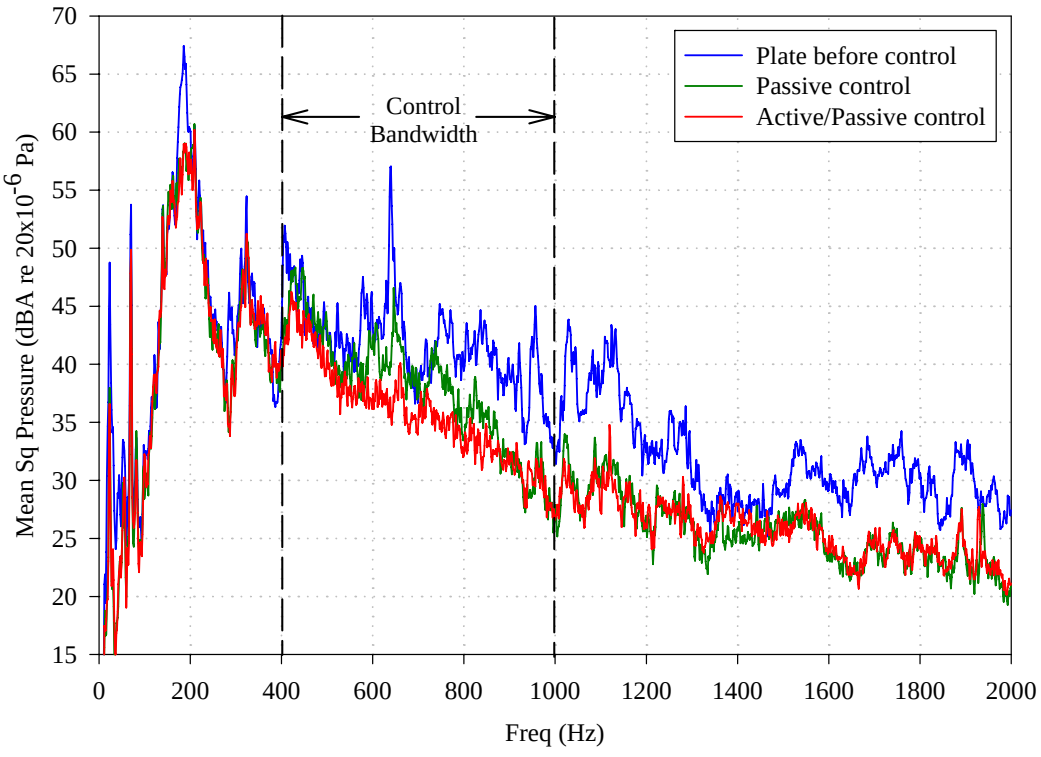

(a)

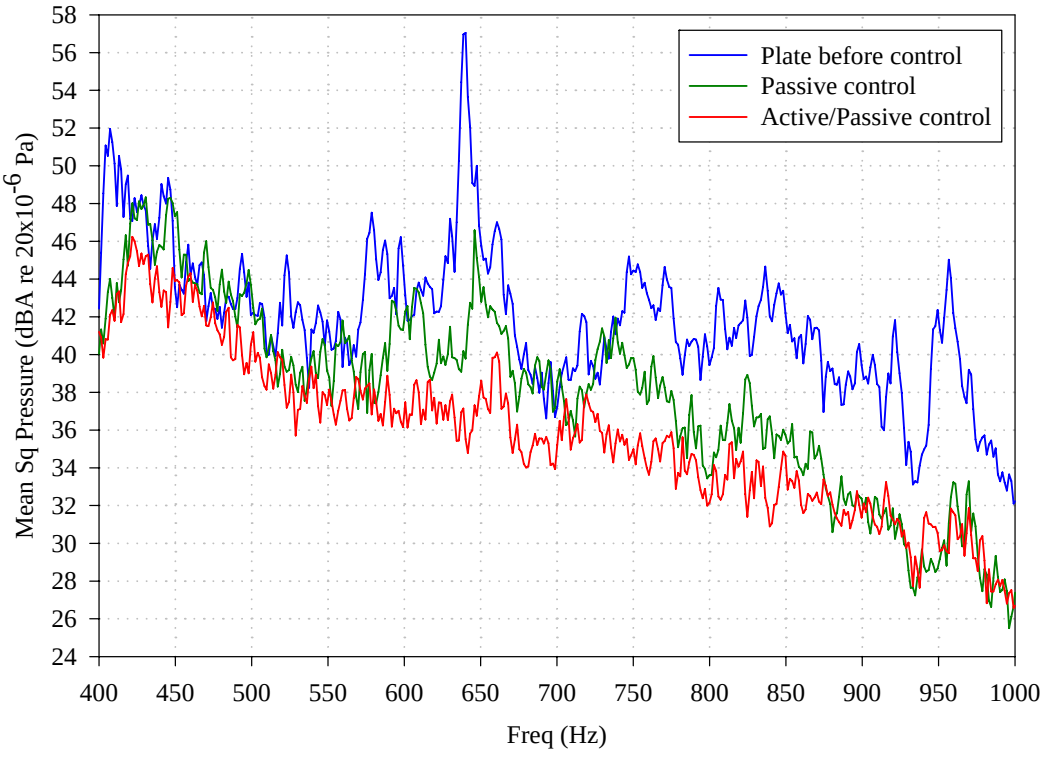

(b)

Figure 5.8 (a) NASA LaRC results with a control bandwidth of 400-1000 Hz. (b) Detail view of control bandwidth.

respective passive and active attenuation contributions in figure 5.9. The data is presented in one-third octave bands where the overall performance of the smart foam actuator, or total attenuation observed, is the summation of both the active and passive components. The attenuation results were also computed for both the entire bandwidth and the specific control bandwidth and are presented in table 5.4.

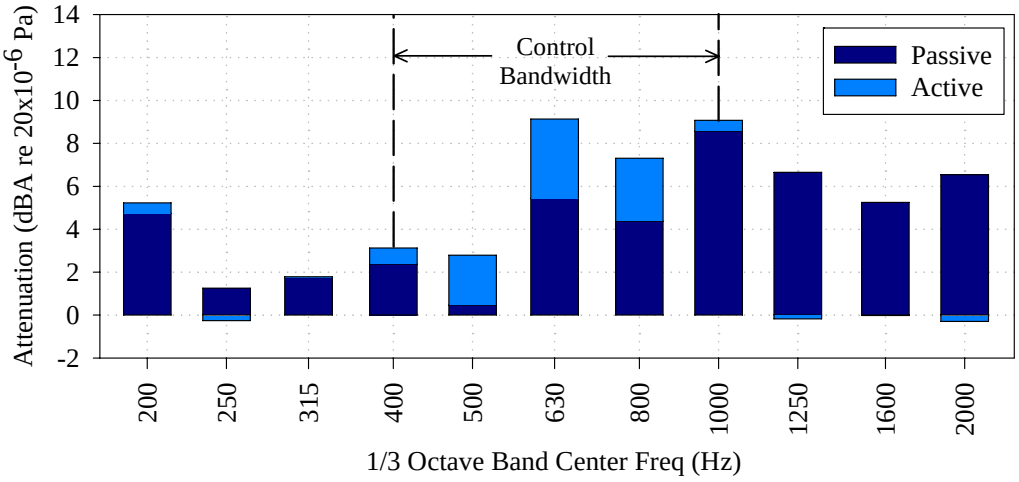

Figure 5.9 NASA LaRC attenuation results in one-third octave bands.

Table 5.4 NASA LaRC attenuation results.

Bandwidth	Passive Attenuation	Active Attenuation	Total Attenuation Active + Passive
0 – 2000 Hz.	3.8 dBA	0.7dBA	4.5 dBA
400 – 1000 Hz.	3.5 dBA	2.5 dBA	6.0 dBA

5.4 AEDC HIGH SPEED EXPERIMENTS

5.4.1 Test panel

A panel was designed and built by NASA LaRC to be used in experiments performed at the AEDC wind tunnel test facility. The panel construction and mounting procedure was similar to the NASA LaRC test panel, however, since the AEDC tunnel was a high speed tunnel a few modifications were required. It was necessary to add two additional frames and stringers to the panel to reduce the stress experienced by the panel induce by the high-speed flow. The stiffeners were again attached to the panel in a manor similar to that used in the construction of an actual aircraft panel. The frames and stringers again sectioned the panel into six equal size subsections measuring 15 in. x 5.25 in. and can be seen in figure 5.10. The test section was notably smaller than the NASA LaRC pane1 subsection that measured 18.5 in. x 9 in.

5.4.2 Measurement setup

5.4.2.1 Actuators

A separate set of actuators were designed and manufactured for the AEDC wind tunnel experiments according to the procedure outlined in Chapter 2. The specific design characteristics for the smart foam actuators are shown in figure 5.11. Throughout this

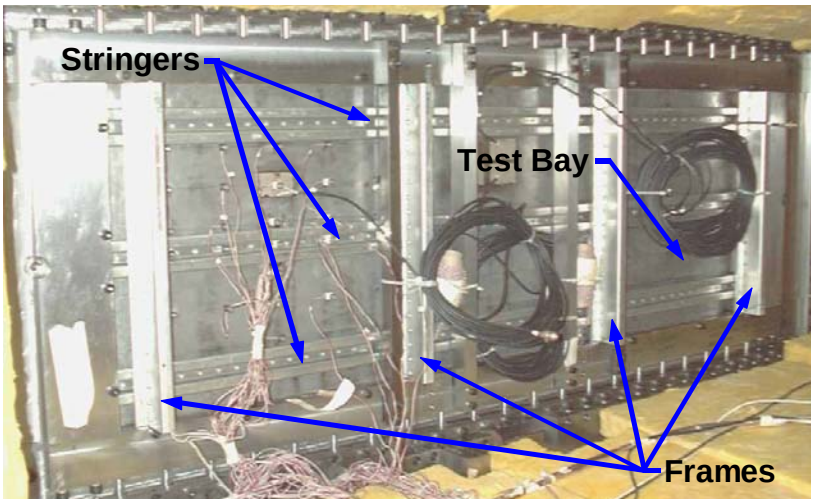

Figure 5.10 AEDC test panel.

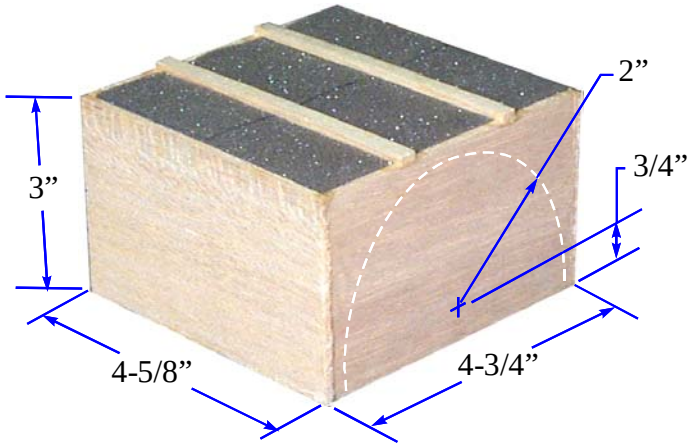

Figure 5.11 Actuator used in AEDC experiments.

project, substantial effort has been placed on improving the low frequency radiation efficiency of the smart foam actuators. Two main differences are noted between the actuators used in the NASA experiments with those used at AEDC. First, the actuators were thicker allowing a larger piece of PVDF to be used. Recall that larger PVDF results in more out-of-plane displacement and, consequently, more far-field radiation. Also, the thicker foam results in better passive attenuation. Second, the edges of the balsa frame were rigidly attached using glue to the radiating surface, which effectively baffled the rear of the actuator. The improvement in radiated sound power between the AEDC actuators and those used in the NASA LaRC experiments was previously presented in figure 2.7.

Engineers from NASA LaRC again performed a modal analysis of the panel used in the AEDC experiments and the results can be seen in the Appendix. The modal behavior of the panel did not, however, help determine the actuator configuration used in the smart foam control experiments. The number of smart foam actuators and their dimensional properties were instead based on maximizing radiation efficiency and control authority, therefore, the AEDC test panel was instrumented with only three actuators due to the reduction in radiating surface area. The three actuators were larger than those used in the NASA LaRC experiments yet some control flexibility was maintained by having multiple control channels. Similar to the NASA LaRC experiments, there was a 0.25 in. spacing between all of the actuators, which was filled with strips of acoustic foam.

5.4.2.2 Instrumentation

The same experimental methodology used in the NASA LaRC tests was implemented in conducting the AEDC experiments, therefore, the same control sensors were utilized. Figure 5.12 shows the relative positions of the actuators and accelerometers. Each actuator was used as a separate control channel and three accelerometers were collocated with the center of control channels and used as references. A 3 x 5 array of microphones were evenly distributed 20 in. above the panel to monitor the global control performance. Four of these microphones, located in the same positions as described for the NASA experiments, were used as error sensors and the same anechoic enclosure was used to isolate the radiated panel noise from other noise sources. For the AEDC experiments, PCB microphones (Model 130A10) were used with a control bandwidth set to be 400 – 800 Hz.

As previously discussed, the maximum level of control that can be achieved depends partially on the multiple coherence function between the reference and error sensors. In the NASA LaRC experiments, the number and position of the reference sensors were chosen based on analysis of data acquired by eight accelerometers mounted to the panel and excited by the turbulent boundary layer. The time restrictions with the experiments performed at AEDC did not permit a separate acquisition of panel data for the purpose of determining reference sensor locations. The financial restraints required that all tests for both Mach 0.8 and Mach 2.5 tunnel speeds be performed within a three-hour time block. In addition, logistics involving the tunnel operation required thirty minutes of both startup and shutdown time for each test setup. The multiple coherence

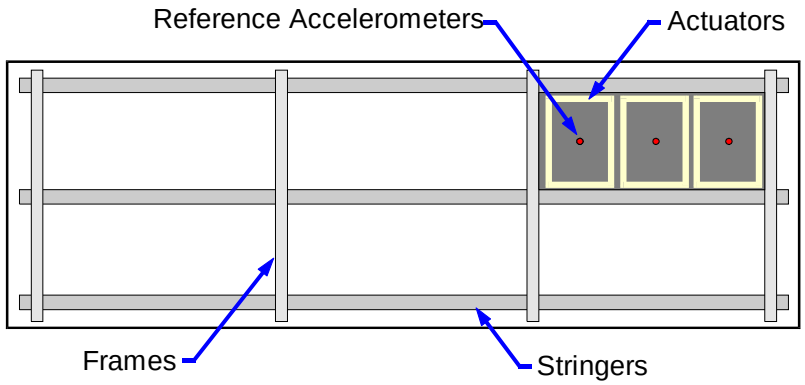

Figure 5.12 AEDC actuator configuration.

was therefore calculated for both flow speeds using the three accelerometers used as references for control (i.e. collocated with the control channel) and can be seen in figure 5.13. Note that the multiple coherence for the AEDC experiments was considerably less than for the experiments performed at NASA LaRC. One reason this may have occurred was the use of one less reference sensor on the AEDC panel. Most likely, however, the reductions in coherence levels were due to the increased levels of background noise. The coherence levels for the Mach 0.8 flow speed were still high at frequencies within the control bandwidth (400 – 800 Hz), therefore, some control was expected. One thing to note about the AEDC wind tunnel was that the side of the panel opposite the flow was depressurized. This was necessary to reduce the high pressure gradient across the panel cause by the large pressure reduction inside the tunnel induced by the high flow speeds. This does, however, reduce the levels of noise radiated by the panel since radiation efficiency is a function of air density.

5.4.2.3 Controller

The same controller and interface program that was used in the NASA LaRC experiments was also used for experiments at AEDC. The control parameters selected for the AEDC tests are summarized in table 5.5. One notable difference between the parameters at AEDC and those at NASA LaRC is the number of control path coefficients. At NASA LaRC, 190 was the largest possible value for the control path coefficients, which was determined by the number of control elements selected and the speed of the DSP. The test setup at AEDC contained one fewer actuator and reference signal, therefore, more coefficients were available for control because of the reduced demands on the DSP.

Table 5.5 Control parameters for AEDC experiments.

Controller Parameters	Value
Number of Actuators	3
Number of error sensors	4
Number of reference sensors	3
Sampling frequency	3000 Hz
System ID coefficients	50
Control path coefficients	250

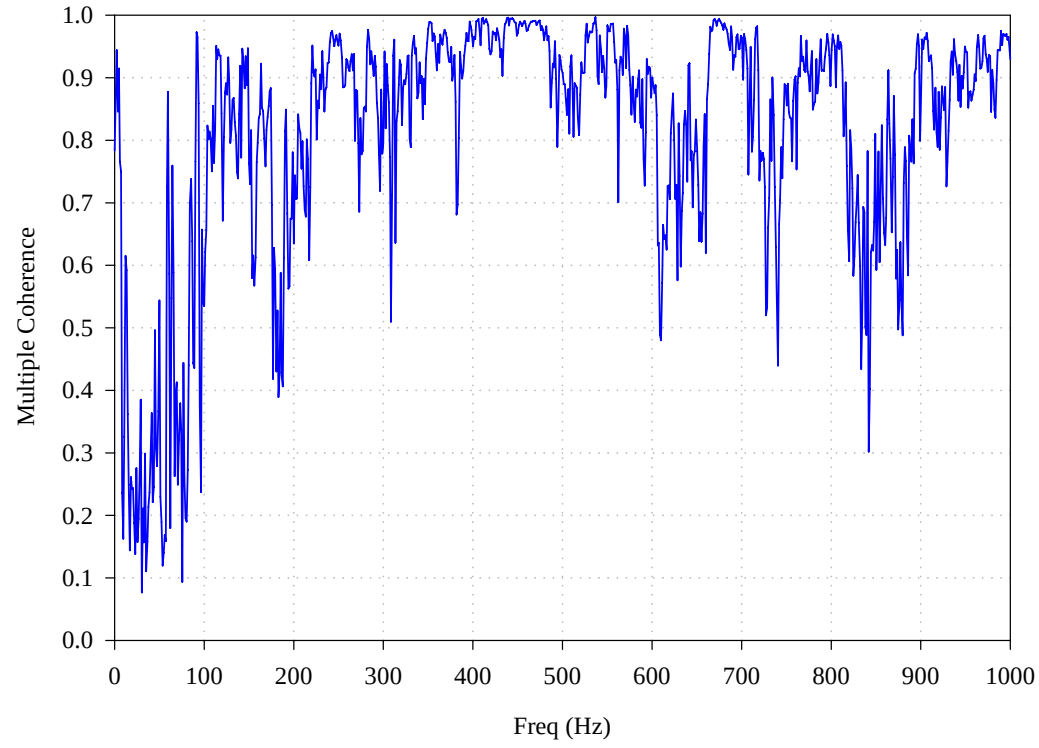

(a)

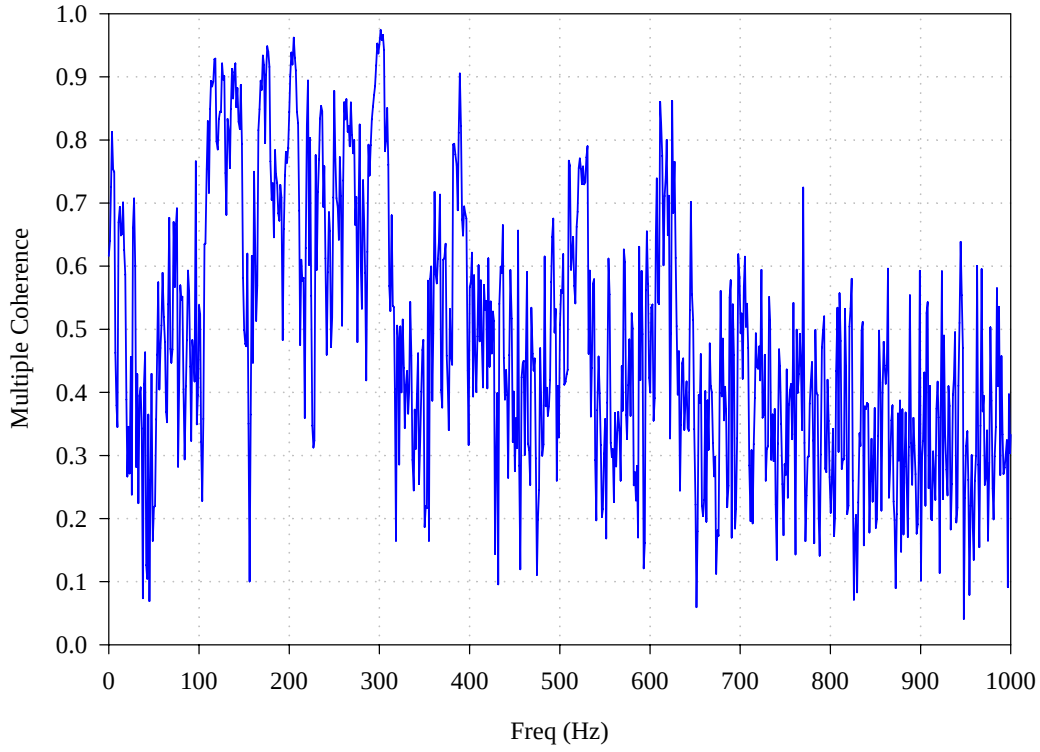

(b)

Figure 5.13 Multiple coherence of AEDC panel. (a) Mach 0.8 flow speed. (b) Mach 2.5 flow speed.

Again, few system ID coefficients were required to model the transfer functions between the actuators and error sensors due to the damping added by the acoustic wedge treatment of the anechoic enclosure.

5.4.2.4 Data Acquisition

As before, a separate data acquisition system was used to acquire performance data for all experiments. For the AEDC tests, the Boeing Company provided field support and was responsible for the acquisition of data for all of the experiments performed. Time histories were recorded digitally for all accelerometer and microphone channels using a sampling frequency of 20000 Hz. The time data was then processed and analyzed using MATLAB®.

5.4.3 Results

5.4.3.1 Mach 0.8

The same process as was outlined for the NASA LaRC experiments was performed in the AEDC wind tunnel experiments. The performance of the smart foam actuators for the control of turbulent boundary layer noise must be evaluated on both passive and active control contributions. As previously described, it was necessary to acquire data for bare panel radiation to establish a baseline from which to evaluate the control performance. Next, the panel radiation was acquired with the smart foam actuators glued in place on the panel to measure the passive attenuation performance of the foam treatment alone. Finally, the smart foam actuators were driven within a bandwidth of 400 – 800 Hz and a acquisition was taken reflecting the combined active and passive attenuation performance of the smart foam. As before the global performance of the control system was evaluated by calculating the mean square pressure of all fifteen microphones with an applied A-weighting. Figure 5.14 displays the results obtained in the experiments performed at a flow speed of Mach 0.8.

Similar observations are made for the AEDC experiments that were noted in the NASA LaRC tests. The most noteworthy observation is the passive attenuation results obtained by the smart foam. Again, as expected, the absorptive properties of the foam

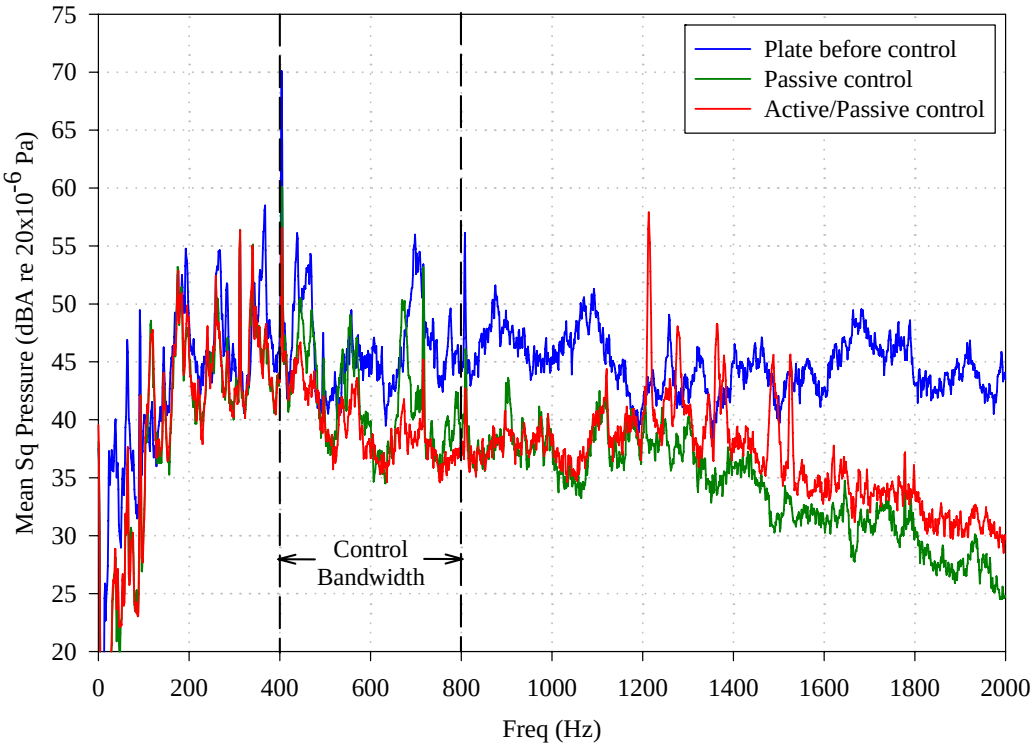

(a)

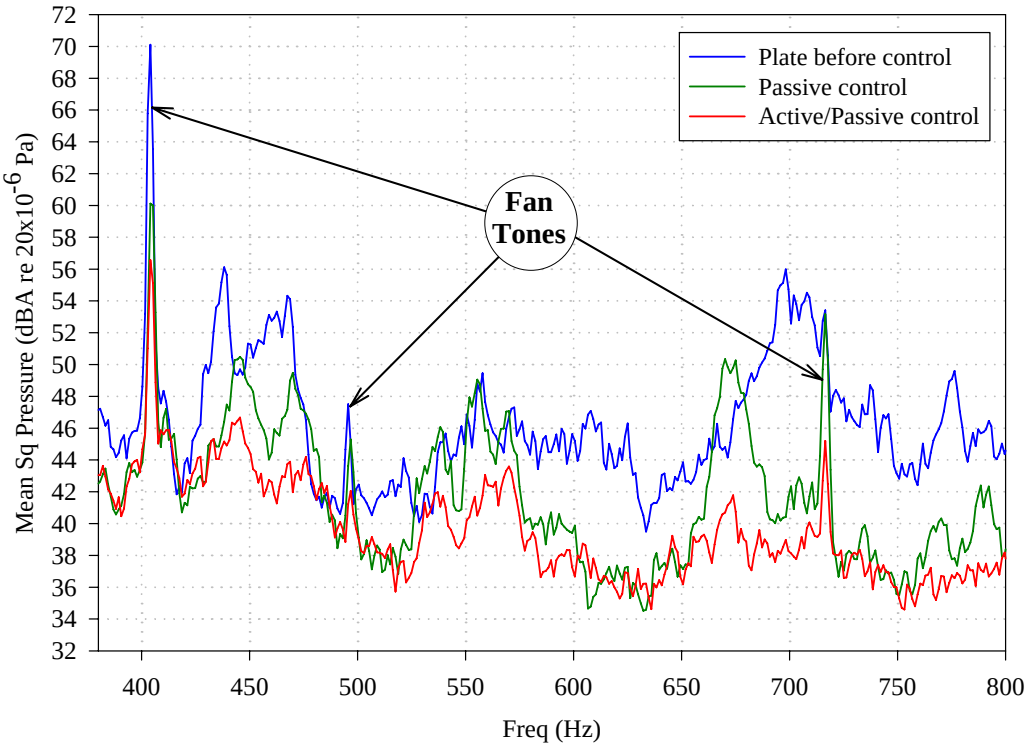

(b)

Figure 5.14 (a) AEDC Mach 0.8 results with a control bandwidth of 400-800 Hz. (b) Detail view of control bandwidth.

tend to improve at the higher frequencies. The attenuation results were also computed for one-third octave bands in figure 5.15 and for the entire bandwidth and specific bandwidth in table 5.6. Note that there was 3.5 dBA of total contribution within the control bandwidth and as much as 5 dBA within the 630 Hz band. Note from figure 5.14 that there was negative control performance at the frequencies starting at approximately 1200 Hz. The controller input/output board has a maximum allowable voltage of ±10 volts and if the control signals are allowed to approach this range the actuator signals clip. It is likely that during these experiments the actuators were driven non-linear thus introducing the high frequency noise, which could be removed with better low-pass filters. Despite the introduced noise, the total attenuation was 5.6 dBA over the entire 2000 Hz bandwidth. It should be noted that there were fan tones present in the data and are noted in figure 5.14(b).

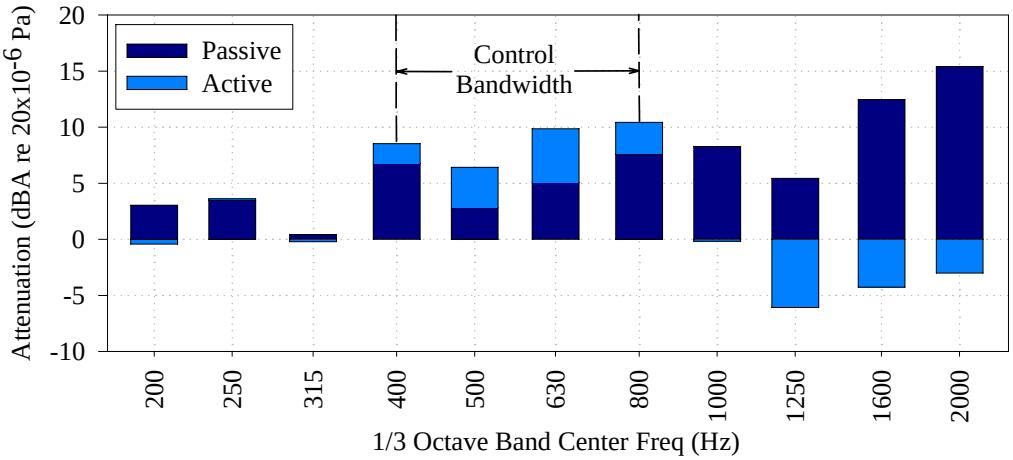

Figure 5.15 AEDC mach 0.8 attenuation results in one-third octave bands.

Table 5.6 AEDC mach 0.8 attenuation results.

Bandwidth	Passive Attenuation	Active Attenuation	Total Attenuation Active + Passive
0 – 2000 Hz.	5.6 dBA	0.0 dBA	5.6 dBA
400 – 800 Hz.	5.5 dBA	3.5 dBA	9.0 dBA

5.4.3.2 Mach 2.5

Figure 5.16 shows the control results for the same actuator configuration with a flow speed of Mach 2.5. As before, the attenuation results are presented for one-third frequency bands in figure 5.17 and for the entire bandwidth and specific bandwidth in table 5.7. The passive attenuation over the 2000 Hz bandwidth was 9.6 dBA, however, there was very little additional attenuation achieved by driving the actuator. This was due in part to the poorly coherent reference signal and the lack of control authority due to the test chamber depressurization.

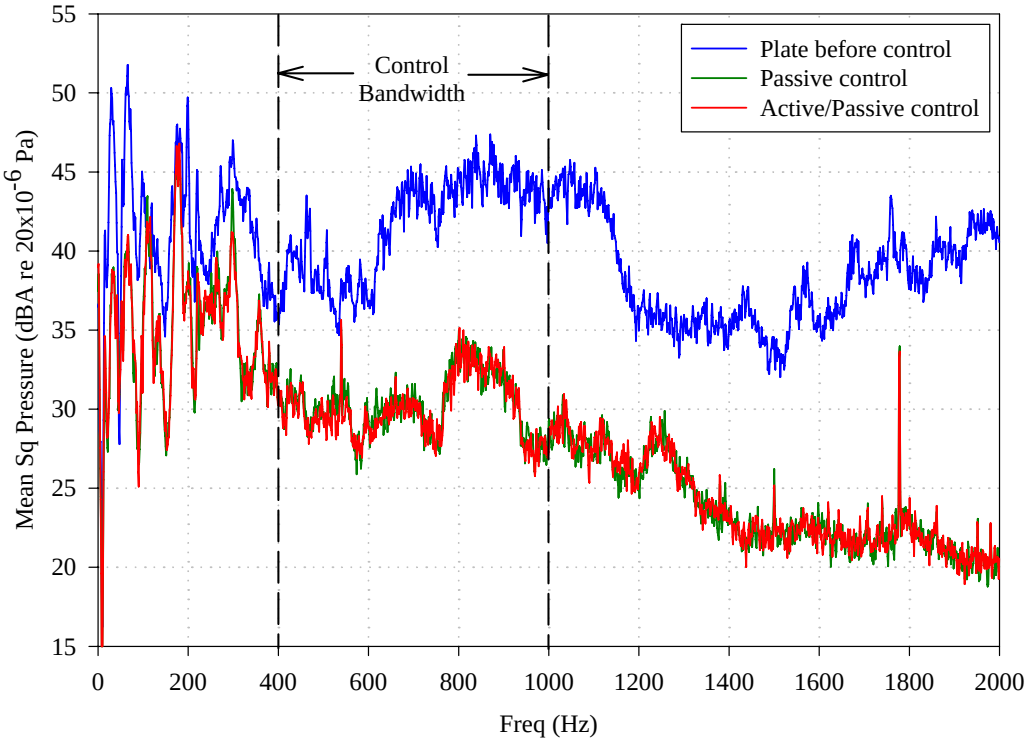

Figure 5.16 AEDC mach 2.5 results with a control bandwidth of 400-1000 Hz.

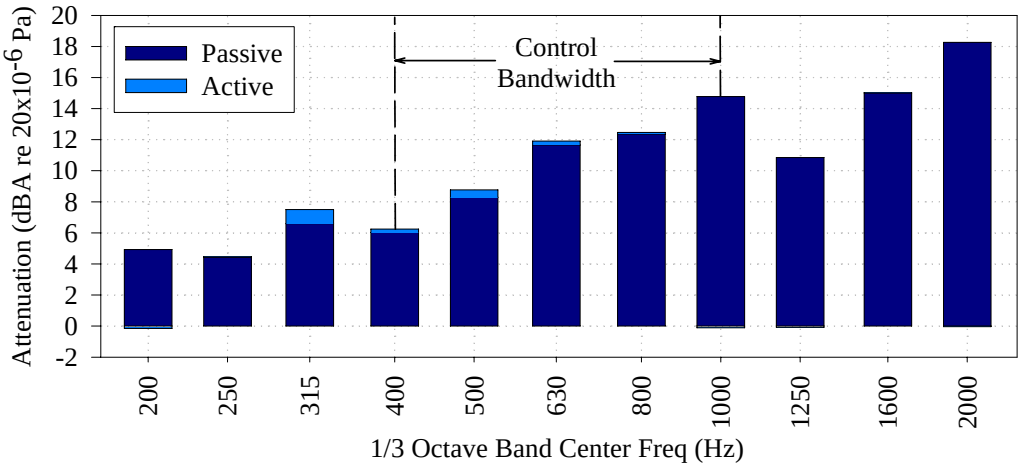

Figure 5.17 AEDC mach 2.5 attenuation results in one-third octave bands.

Table 5.7 AEDC mach 2.5 attenuation results.

Bandwidth	Passive Attenuation	Active Attenuation	Total Attenuation Active + Passive
0 – 2000 Hz.	9.6 dBA	0.1 dBA	9.7 dBA
400 – 1000 Hz.	11.9 dBA	0.2 dBA	12.1 dBA

5.5 VPI LOW SPEED EXPERIMENTS

It has been previously noted that the VPI wind tunnel was primarily used to prepare for the experiments performed at the NASA LaRC and AEDC test facilities. Some of the testing parameters explored using the VPI tunnel throughout the course of the project included actuator configurations, mounting conditions, and control parameters involving both reference and error sensors. This freedom to test numerous scenarios helped to minimize the number of iterations required at each of the test sites, which was important due to the cost involved in the operation of these larger wind tunnels.

5.5.1 Test Panel

The test panel designed for the turbulent boundary layer control experiments at VPI was built to be the same size as a single subsection of the NASA LaRC panel. Specific details regarding the construction and mounting of the 20 in. x 10 in. x 0.050 in. aluminum panel were presented in Chapter 4.

An experimental modal analysis was performed on the VPI test panel in which FRF data was acquired between an accelerometer and an impact hammer at fifty evenly distributed locations on the panel. The data was analyzed in MATLAB® using a single-degree-of-freedom analysis and the results are presented in table 5.8. The experimental mode shapes are also presented in the Appendix. One thing to note is that the structural modes of the VPI panel occurred at much lower frequencies than those observed in the NASA LaRC panel subsection (e.g. the (1,1) mode for the VPI panel was 119 Hz and 276 Hz for the NASA LaRC panel). This difference was due to the tension applied to the NASA LaRC panel.

5.5.2 Measurement Setup

5.5.2.1 Actuators

Although many actuator configurations were tested using the VPI wind tunnel facility, a separate set of actuators were designed following the AEDC tunnel tests to improve radiation efficiency. Specific design characteristics for the actuators are shown in figure

Table 5.8 Modal analysis of VPI test panel.

Mode*	Theoretical Frequencies (Hz)	Experimental Frequencies (Hz)
(1,1)	125.2	119.4
(1,2)	160.3	164.9
(1,3)	222.9	232.4
(1,4)	313.2	320.3
(2.1)	327.1	285.4
(2,2)	362.0	330.8
(2,3)	420.9	388.4
(1,5)	429.7	430.6
(2,4)	505.8	475.9
(1,6)	571.5	563.8
(2,5)	617.2	581.1
(3,1)	630.1	534.3

Note: (*) Mode (m,n) corresponds to "m" half-wavelengths along the 10" dimension and "n" half-wavelengths along the 20" dimension.

5.18. The actuator size was chosen by incorporating the largest radius that could be formed from a standard sheet size of PVDF (8 in. x 10.5 in. of active surface). The balsa frames of the smart foam actuators were again glued to the panel, thus baffling the rear of the actuator and improving its far-field radiation. Four separate actuators were positioned on the panel and each was driven independently by the controller creating four output control channels (see figure 5.19). Again, the actuators were not positioned linearly in an effort to give the controller flexibility in controlling the higher order modes.

5.5.2.2 Instrumentation

The same control methodology and, therefore, the same sensors were used in the VPI experiments as in the NASA LaRC and AEDC tests. Four microphones were used as error sensors and an additional four were used to help monitor the global performance of the controller. The control bandwidth, implemented by band-pass filtering the error signals, was set to be 250 – 630 Hz.

As before, four accelerometers were used as references by the controller and were mounted directly to the panel and collocated with each of the actuators as shown in figure

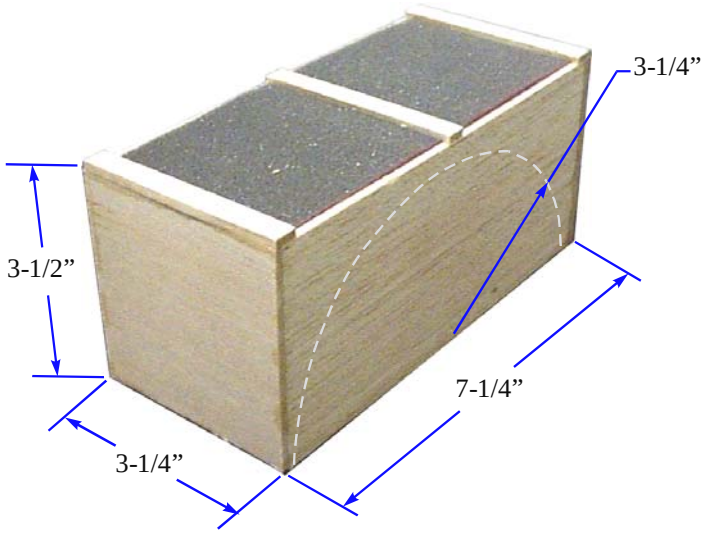

Figure 5.18 Actuator used in VPI experiments.

5.19. The multiple coherence was also measured to establish whether the chosen accelerometer locations provided a coherent signal with each of the actuators. The multiple coherence measured at one of the microphones is shown in figure 5.20.

5.5.2.3 Control and Data Acquisition

The experiments performed at VPI contained the same number of actuator, error, and reference channels as the NASA LaRC experiments, therefore, the parameters selected for control were the same as were summarized in table 5.3. Likewise, the same data acquisition equipment and programs were used to collect and record the data, which was again was sampled at 6000 Hz.

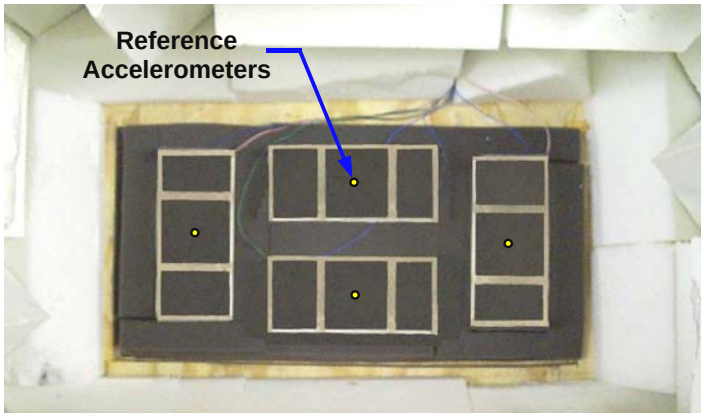

Figure 5.19 VPI actuator configuration.

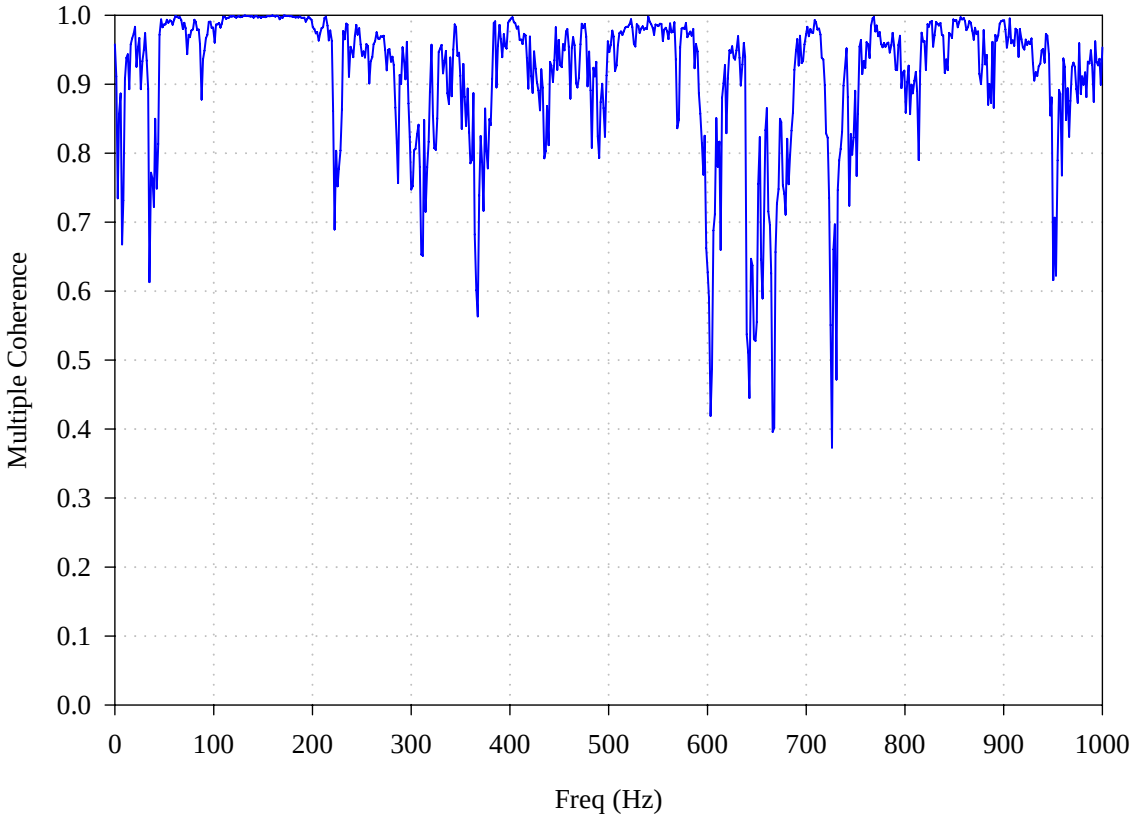

Figure 5.20 Multiple coherence of VPI panel.

5.5.3 Results

As was performed in previous experiments, the mean squared pressure was acquired and A-weighted for the bare panel, passive control, and active control cases and can be seen in figure 5.21. Again the attenuation observed due to the passive smart foam properties can be attributed to two separate mechanisms. At the high frequencies, the passive attenuation is due to absorption and at the low frequencies the absorption is primarily due to the added damping to the panel. Note the high levels of passive attenuation around the first three panel modes (119 Hz, 165 Hz, and 232 Hz) caused by the damping added by the smart foam. The VPI wind tunnel is a much smaller and slower tunnel than the two other test facilities used in this project, which can be observed in the low levels of excitation, especially at the higher frequencies. Fan tones were also present in the plate radiation data recorded by the microphones and are noted in figure 5.21(a). The presence of fan tones, although not present in a pure turbulent boundary layer disturbance, were

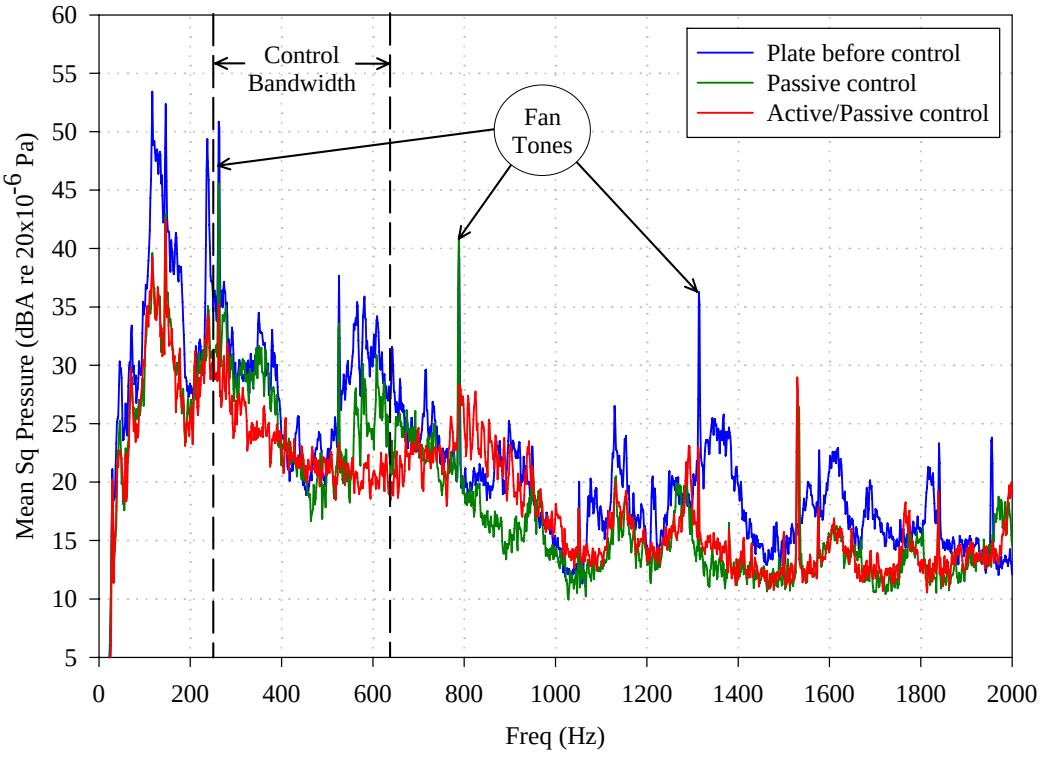

(a)

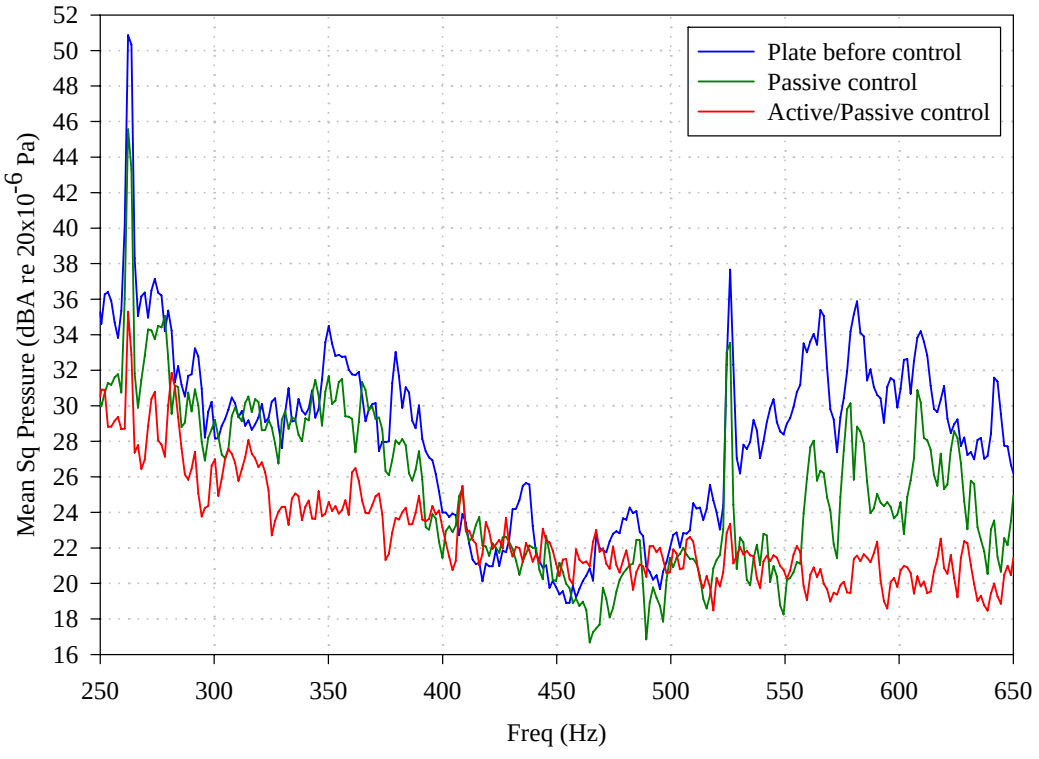

(b)

Figure 5.21 (a) VPI results with a control bandwidth of 250 – 630 Hz. (b) Detail view of control bandwidth.

easily removed by the smart foam active control system. The fundamental tone and first harmonic were reduce 16 dbA and 14 dBA respectively.

A separate experiment was performed as an attempt to quantify the passive contribution of the individual smart foam elements. Again the bare panel radiation was acquired at an array of microphones to establish a baseline for comparison. Next, the same microphone array was used to acquire the panel radiation when treated with a plain foam layer made from the same acoustic foam used to construct the smart foam cells. Finally, the panel radiation was acquired with the smart foam actuators glued to the panel as was displayed in figure 5.19. The passive attenuation comparison can be seen in figure 5.22. It is observed that the panel with just foam has attenuation in the 100 – 125 Hz frequency bands whereas the panel with smart foam has significant attenuation in all frequency bands below 200 Hz. It is also observed that the layer of PVDF embedded within the acoustic foam adds to the attenuation in the high frequencies. This is consistent with results obtained by Gentry-Grace [43] and is due to a dissipation of acoustic energy caused by the discontinuity.

The control contribution of both the active and passive smart foam components

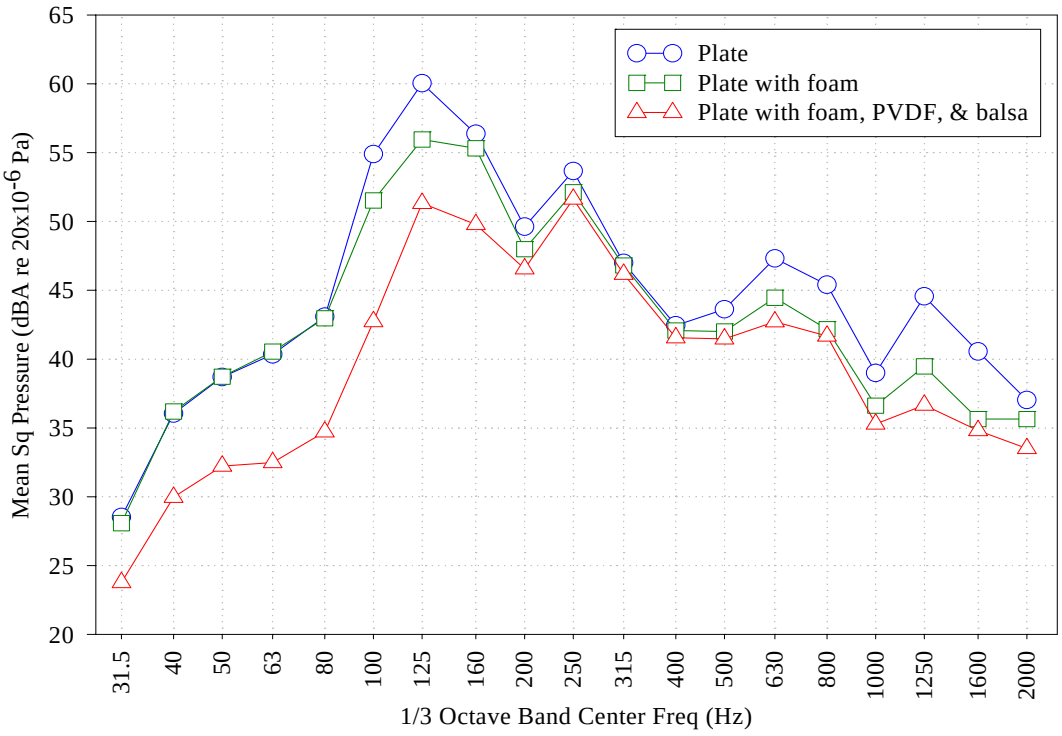

Figure 5.22 Passive attenuation properties of a smart foam actuator by components.

can be seen in figure 5.23. The active elements of the smart foam actuators were able to significant contribute to the attenuation across the entire control bandwidth between 250 – 630 Hz. The control achieved in the 200 Hz and 800 Hz frequency bands was due to roll-off in the filters used to band-pass filter the error signals prior to entering the controller. Notice that in the 1000 Hz, 1250Hz, and 1600 Hz octave bands, the active control signals slightly increased the sound pressure levels. As the filtered-x LMS control algorithm tries to minimize (or flatten) the response at the error microphones, frequencies that are less dominant in the overall pressure spectrum are raised in an effort to control the most dominant frequencies. The attenuation results are tabulated for the entire bandwidth and the specific control bandwidths in table 5.9. The active attenuation contribution over the entire frequency spectrum has been improved to 1.6 dBA whereas in the NASA LaRC tests only 0.7 dbA was realized. This can be attributed to the improved control authority at low frequencies accomplished by increasing the physical size of the active layer and by gluing the balsa to the radiating structure. The improvements allowed the active control bandwidth for the VPI experiments to start at 250 Hz whereas the NASA LaRC control bandwidth started at 500 Hz. Although the AEDC actuators were glued to the structure, the bandwidth was unable to be set below 400 Hz because of the loss of control authority due to the depressurized test chamber.

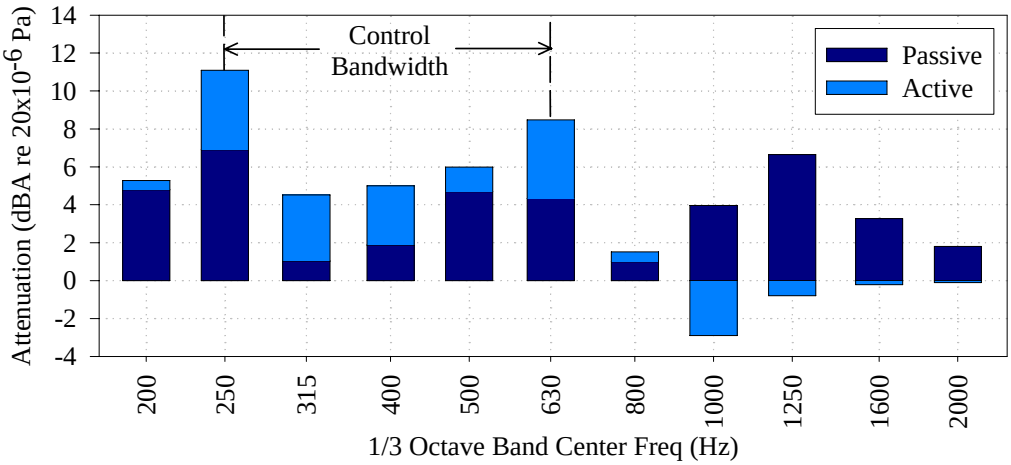

Figure 5.23 VPI attenuation results in one-third octave bands.

Table 5.9 VPI attenuation results.

Bandwidth	Passive Attenuation	Active Attenuation	Total Attenuation Active + Passive
0 – 2000 Hz.	7.6 dBA	1.6 dBA	9.2 dBA
200 – 630 Hz.	4.2 dBA	4.5 dBA	8.7 dBA

Chapter 6

Conclusions and Future Work

The effectiveness of smart foam actuators in controlling panel sound radiation excited by a turbulent boundary layer disturbance has been demonstrated. Smart foam is a hybrid device combining acoustic foam and an embedded PVDF smart skin. The foam works as an acoustic absorber that attenuates the high-frequency content, while the PVDF is driven actively and used to overcome the limitations of the foam at low frequencies. The smart foam actuator is therefore an effective control device for broadband applications and, due to its lightweight when compared to conventional speakers, is an ideal control device for aircraft noise problems.

An experimental methodology was developed for testing the control of aircraft panel radiation using smart foam actuators and was tested using three separate wind tunnel testing facilities. A test panel, representing the exterior fuselage skin of an aircraft, was mounted on the wall of a wind tunnel. The tunnel flow was then used to excite the panel that, consequently, radiated sound into an anechoic enclosure representative of an aircraft cabin. Within the anechoic enclosure was a series of smart foam actuators mounted to the panel and an array of microphones used to monitor the performance of the control system. A multiple channel feedforward filtered-x LMS control algorithm was used to drive the smart foam actuators such that the superposition of the actuator generated sound and the panel noise produced cancellation at the error microphones.

One characteristic of a smart foam actuator is the poor radiation efficiency of the device at low frequencies (i.e. <250 Hz). Most piezoelectric materials, including PVDF,

do not generate large displacements for an applied voltage, which is a fundamental requirement in the generation of low-frequency noise. The PVDF is positioned within the acoustic foam in a half-cylinder configuration to couple the in-plane strain associated with the piezoelectric effect with a maximum amount of vertical displacement. The smart foam cell is then housed within a balsa frame that both anchors the ends of the PVDF and serves as a baffle. Effort throughout the project was focused on improving the performance of the smart foam actuators at low frequencies.

Successful broadband control results were achieved using two separate low-speed wind tunnel test facilities. The smart foam actuators were tested on a Mach 0.2 wind tunnel at the NASA Langley Research Center (NASA LaRC). Across the 0 – 2000 Hz frequency band a total attenuation of 4.5 dBA was achieved where 3.8 dBA was due to the passive contribution. The active control element was driven in the 400 – 1000 Hz where attenuation of 2.5 dBA was realized. A similar set of experiments were later performed on a Mach 0.1 wind tunnel belonging to Virginia Polytechnic Institute and State University (VPI). Two key modifications were made to the actuators prior to the testing at VPI. The first modification was that the actuators were physically larger in size in order to incorporate a larger piece of PVDF. The second modification included gluing the edges of the balsa frame to the radiating panel thus baffling the backside of the actuator and improving its radiation efficiency. Experiments were performed and from 0 – 2000 Hz attenuation of 9.2 dBA was obtained with 7.6 dBA contributed passively. Actively the smart foam was able to contribute 4.5 dBA between 250 – 630 Hz. The increase in performance can be attributed to the improvements in control authority at low frequencies due to the smart foam modifications.

Broadband control results were also achieved using the high-speed wind tunnel test facility at the Arnold Engineering Development Center (AEDC). At the Mach 0.8 flow speed, 5.6 dBA of total attenuation was obtained all coming from the passive properties of the foam. Active contribution was 3.5 dBA in the 400 – 800 Hz bandwidth. At the Mach 2.5 flow speed, a total attenuation of 9.7 dBA was achieved with 9.6 dBA coming from the passive properties of the smart foam. Although the smart foam actuators were large and the frame was glued to the panel, control authority was compromised in the high-speed experiments because the test chamber was depressurized.

The potential for smart foam in controlling broadband radiation due to a turbulent boundary layer disturbance has been demonstrated for various flight conditions. It is clear from these experiments that future improvements in results depend on the ability to increase control authority at low frequencies. The smart foam actuators used in the VPI experiments were able exhibit control as low as 250 Hz octave band, however, a disturbance with dominant noise contribution below this frequency could not be controlled with the current smart foam actuator configuration.

Future work with smart foam could include the use of near-field microphones as error sensors. This change allows the multiple control channels to become decoupled and closer approximates the necessary requirements for implementation into an actual aircraft. Some preliminary experiments have been performed with near-field error microphones and show promising results. Also, a more detailed study into understanding and improving the passive properties of each individual component of the smart foam actuator could be performed. A current modification to the smart foam actuator that is being considered is the addition of a distributed mass layer. This mass layer could be tuned to a frequency below the operating range of the smart foam active layer and work as tuned vibration absorber. Due to the inherent flexibility of the smart foam components and their construction, there exists great potential for incorporating additional noise control strategies into the already robust smart foam actuator.

Bibliography

[1] W.L. Willshire, Jr. and D.G. Stephens, “Aircraft noise technology for the 21st century,” *Proceedings of Noise-Con 98*, pp. 7-22, 1998.

[2] J.F. Wilby, “Aircraft interior noise,” *Journal Of Sound and Vibration*, 190(3), pp. 545-564, 1996.

[3] D.E. Bishop, “Cruise flight noise levels in a turbojet transport airplane,” *Noise Control 7*, pp. 37-42, 1961.

[4] N.J. Fleming, “The silencing of aircraft,” *Journal of the Royal Aeronautical Society*, 50, pp. 639-676, 1946.

[5] R.E. Hayden, B.S. Murray, and M.A. Theobald, “Boundary-layer-induced noise in the interior of aircraft, “ *NASA CR-172152*, 1983.

[6] D.A. Bies, “A review of flight and wind tunnel measurements of boundary layer pressure fluctuations and induced structural response,” *NASA CR-626*, 1966.

[7] W.V Bhat, “Flight test measurement of exterior turbulent boundary layer pressure fluctuations on Boeing model 737 airplane,” *Journal of Sound and Vibration*, 14, pp. 439-457, 1971.

[8] W.V. Bhat and J.F. Wilby, “Interior noise radiated by an airplane fuselage subjected to turbulent boundary layer excitation and evaluation of noise reduction treatments,” *Journal of Sound and Vibration*, 17, pp. 449-464, 1971.

[9] L. Maestrello, “Measurement and analysis of the response field of turbulent boundary layer excited panels,” *Journal of Sound and Vibration*, 2(3), pp. 270-292, 1965.

[10] L. Maestrello, “Radiation from and panel response to a supersonic turbulent boundary layer,” *Journal of Sound and Vibration*, 10(2), pp. 261-295, 1969.

[11] J.F. Wilby and F.L. Gloyna, “Vibration measurements of an airplane fuselage structure, I: turbulent boundary layer excitation,” *Journal of Sound and Vibration*, 23, pp. 443-466, 1972.

[12] P.A. Nelson and S.J. Elliot, *Active Control of Sound,* Academic Press, Inc., San Diego, CA, 1992.

[13] J.E. Ffowcs Williams, “Anti-sound,” *Proc. R. Soc. Lond.*, A 395, pp. 63-88, 1984.

[14] C.R Fuller, “Apparatus and method for global noise reduction,” U.S. Patent No. 4,715,599, 1987.

[15] C.R. Fuller, “Active control of sound transmission/radiation from elastic plate by vibration inputs: I. Analysis,” *Journal of Sound and Vibration*, 136(1), pp. 1-15, 1990.

[16] R.A. Burdisso and C.R. Fuller, “Theory of feedforward controlled system eigenproperties,” *Journal of Sound and Vibration*, 153(3), pp. 437-452, 1992.

[17] R.L. Clark, “Advanced sensing techniques for active structural acoustic control,” Ph.D. Dissertation, Virginia Polytechnic Institute & State University, Department of Mechanical Engineering, 1992.

[18] B.T. Wang, R.A. Burdisso, and C.R. Fuller, “Optimal placement of piezoelectric actuators for active control of sound radiation from elastic plates,” *Proceedings of Noise-Con 91*, pp. 267-275, 1991.

[19] Clark, R.L., and Fuller, C.R., “Optimal placement of piezoelectric actuators and polyvinylidene fluoride (PVDF) error sensors in active structural acoustic control approaches,” *Journal of the Acoustical Society of America*, 92(3), pp. 1489-1498, 1992.

[20] W.T. Baumann, F. Ho, and H.H. Robertshaw, “Active structural acoustic control of broadband disturbances,” *Journal of the Acoustical Society of America*, 92(4), pp. 1998-2005, 1992.

[21] H.H. Bruderlin, “Developments in aircraft sound control,” *Journal of the Acoustical Society of America*, 8, pp. 181-184, 1937.

[22] R.H. Nichols, H.P. Sleeper Jr., R.L. Wallace Jr., and H.L. Ericson, “Acoustical materials and acoustical treatments for aircraft,” *Journal of the Acoustical Society of America*, 19(3), pp. 428-443, 1947.

[23] J.S. Mixson and C.A. Powell, “Review of recent research on interior noise of propeller driven aircraft,” *Journal of Aircraft*, 22, pp. 931-949, 1985.

[24] R. Vaicaitis and J.S. Mixson, “Review of research on structureborne noise,” *AIAA Paper*, 85-0786, 1985.

[25] M.A. Simpson, T.M. Luong, C.R. Fuller, and J.D. Jones, “Full-scale demonstration tests of cabin noise reduction using active vibration control,” *Journal of Aircraft*, 28(3), pp. 208-215, 1991.

[26] C.R. Fuller and G.P. Gibbs, “Active control of interior noise in a business jet using piezoceramic actuators,” *Noise-Con 94*, pp. 389-394, 1994.

[27] S.J. Elliott, P.A. Nelson, I.M. Stothers, and C.C. Boucher, “In-flight experiments on the active control of propeller-induced cabin noise,” *Jounal of Sound and Vibration*, 140(2), pp. 219-238, 1990.

[28] U. Emborg, “Application of active noise control in Saab 340 and Saab 2000,” *Proceedings of the Nordic Conference on Vehicle and Machinery Vibrations*, Stockholm, Sweden, September, 1994.

[29] F.W. Grosveld, “Plate acceleration and sound transmission due to random acoustic and boundary-layer excitation,” *AIAA Journal*, Vol. 30, No. 3, pp. 601-607, 1992.

[30] W.R. Graham, “Boundary layer induced noise in aircraft, Part I: The flat plate model,” *Journal of Sound and Vibration*, 192(1), pp. 101-120, 1996.

[31] W.R. Graham, “Boundary layer induced noise in aircraft, Part II: The trimmed flat plate model,” *Journal of Sound and Vibration*, 192(1), pp. 121-138, 1996.

[32] B. W. Mahnken, “Active control of aircraft interior flow noise via the use of active trim panels,” Master’s Thesis, Virginia Polytechnic Institute & State University, Mechanical Engineering Department, 1996.

[33] L. Beranek and L. Ver, *Noise and Vibration Control Engineering: Principles and Applications*, John Wiley & Sons, Inc., New York, NY, 1992.

[34] Y.J. Kang, W. Tsoi, and J.S. Bolton, “The effect of mounting on the acoustical properties of finite-depth polyimide foam layers,” *Proceedings of Noise-Con 93*, Williamsburg, Virginia, pp. 285-290, 1993.

[35] J.S. Bolton and E.R. Green, "Smart foams for active absorption of sound," *Second Conference on Recent Advances in Active Control of Sound and Vibration*, Blacksburg, Virginia, pp. 139-149, 1993.

[36] C.R. Fuller, M.J. Bronzel, C.A. Gentry, and D.E. Wittington, "Control of sound radiation/reflection with adaptive foams," *Proceedings of Noise-Con 94*, Ft. Lauderdale, Florida, pp. 429-436, 1994.

[37] S.J. Elliott, "A simple two microphone method of measuring absorption coefficients," *Acoustic Letters*, 5(2), pp. 39-44, 1981.

[38] C.A. Gentry, C. Guigou, and C.R. Fuller, "Smart foam for applications in passive-active noise radiation control," *Journal of the Acoustical Society of America*, 101(4), pp. 1771-1778, 1997.

[39] C.A. Gentry, C. Guigou, and C.R. Fuller, "Smart foam for active/passive plate radiation control," *Journal of the Acoustical Society of America*, (to appear).

[40] C. Guigou and C.R. Fuller, "Control of aircraft interior broadband noise with foam-PVDF smart skin," *Journal of Sound and Vibration*, 220(3), pp. 541-557, 1999.

[41] Measurement Specialties Inc., "Piezo Film Sensors Technical Manual", Published by Measurement Specialties Inc., Valley Forge, PA, 1998.

[42] Polymer Technology Inc., "Technical Data Sheet: Acoustical Products-An Overview," Published by Polymer Technology Inc., Newark, Delaware, 1994.

[43] C.A. Gentry-Grace, "A Study of Smart Foam for Noise Control Applications," Ph.D. Dissertation, Virginia Polytechnic Institute & State University, Mechanical Engineering Department, 1998.

[44] C. Liang and C.A. Rogers, "A fully coupled acoustic analysis of curved PVDF acoustic actuators for active sound attenuation," *Materials and Devices*, pp. 765-779.

[45] International Organization for Standardization (ISO), "Acoustics-determination of sound power levels of noise sources-precision methods for anechoic and semi-anechoic rooms," #3745-1977 (E)

[46] P. Lueg, "Process of silencing sound oscillations," U.S. Patent No. 2,043,416, 1936.

[47] B. Widrow and S.D. Stearns, *Adaptive Signal Processing*, Prentice-Hall, Inc., Englewood Cliffs, NJ, 1985.

[48] S.J. Elliott, I.M. Stothers, and P.A. Nelson, "A multiple error LMS algorithm and its application to the active control of sound and vibration," *IEEE Transactions on Acoustics, Speech, and Signal Processing*, Vol. ASSP-35. No. 10, pp. 1423-1434, 1987.

[49] R.A. Burdisso, J.S. Vipperman, and C.R. Fuller, "Causality analysis of feedforward-controlled systems with broadband inputs," *Journal of the Acoustical Society of America*, 94(1), pp. 234-242, 1993.

[50] L.L. Beranek, *Noise Reduction*, McGraw-Hill Book Company Inc., NY, p. 258, 1960.

[51] Illbruck Inc., "Technical Data Sheet: SONEX Acoustic Products," Illbruck Inc., Minneapolis, MN, 1995.

[52] D.A. Bies and C.H. Hansen, *Engineering Noise Control: Theory and Practice*, Second Edition, E&FN Spon, London, UK, p. 233, 1996.

Appendix

Test Panel Mode Shapes

Chapter 5 gave a detailed description of each of the three test panels used in the turbulent boundary layer control experiments for this project. An experimental modal analysis was also performed for each of the panels in order to assist in the design and placement of the smart foam actuators. Chapter 5 also presented a list of modes and their corresponding frequencies for each of the modals performed. The figures in the appendix are the mode shapes for each of the panels analyzed.

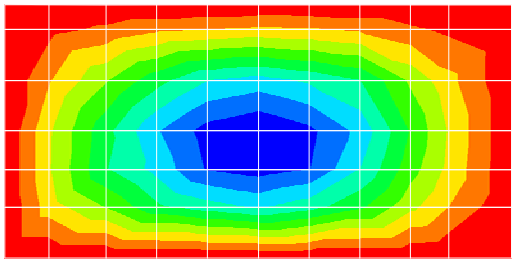

Mode (1,1) = 276 Hz

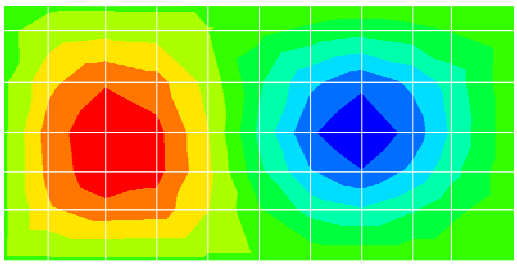

Mode (1,2) = 349 Hz

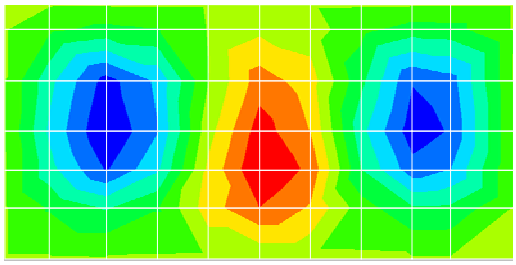

Mode (1,3) = 443 Hz

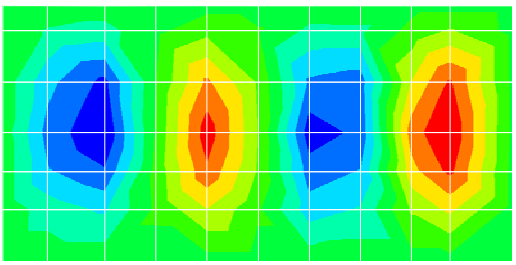

Mode (1,4) = 553 Hz

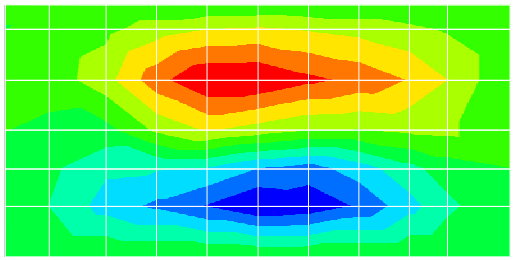

Mode (2,1) = 581 Hz

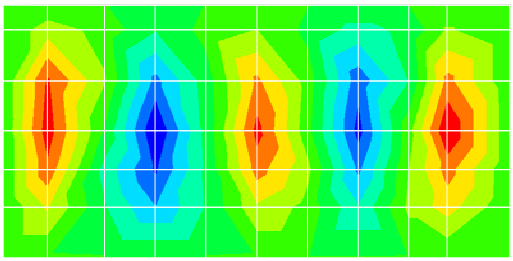

Mode (1,5) = 651 Hz

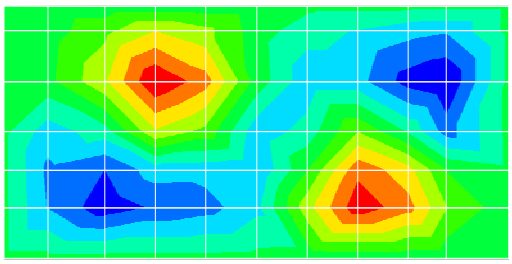

Mode (2,2) = 678 Hz

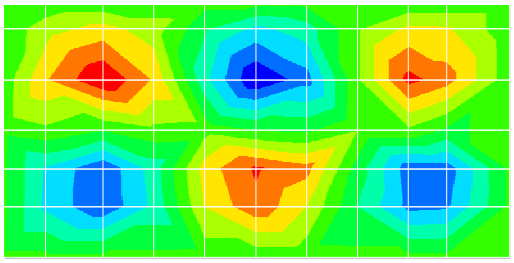

Mode (2,3) = 768 Hz

Figure A.1 Experimental mode shapes of NASA LaRC test panel.

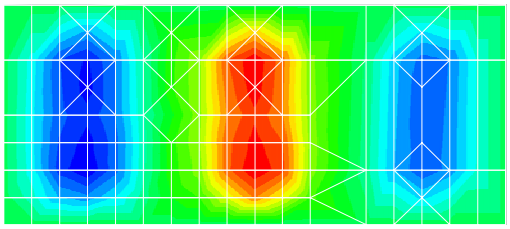

Mode 1 = 192 Hz

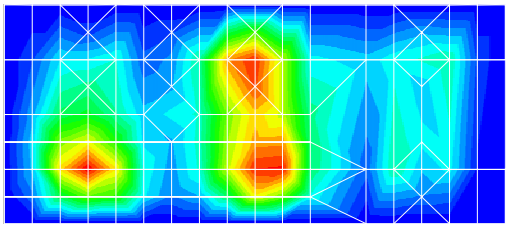

Mode 2 = 225 Hz

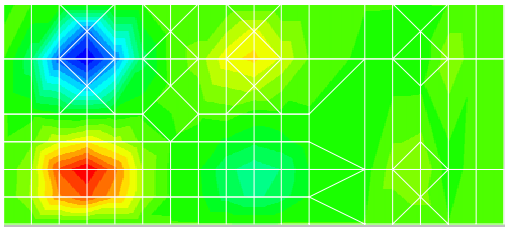

Mode 3 = 255 Hz

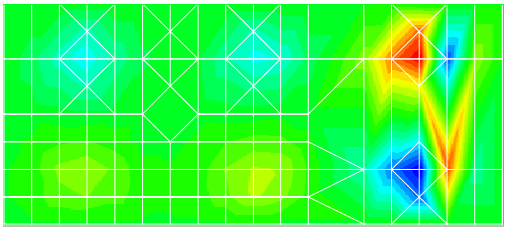

Mode 4 = 265 Hz

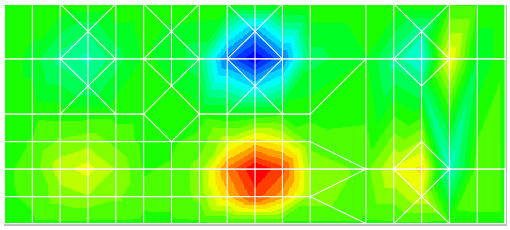

Mode 5 = 280 Hz

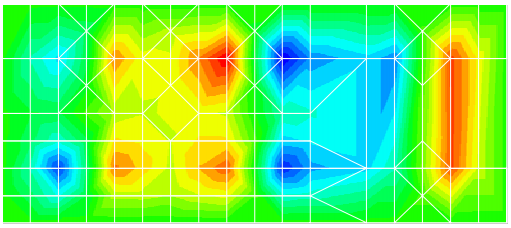

Mode 6 = 338 Hz

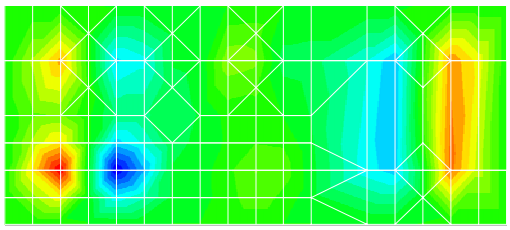

Mode 7 = 351 Hz

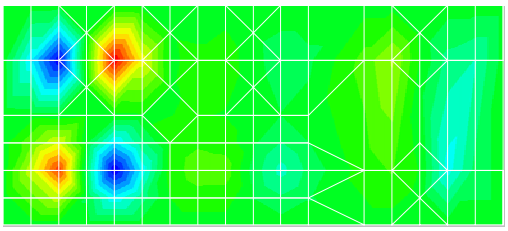

Mode 8 = 361 Hz

Figure A.2 Experimental mode shapes of AEDC test panel.

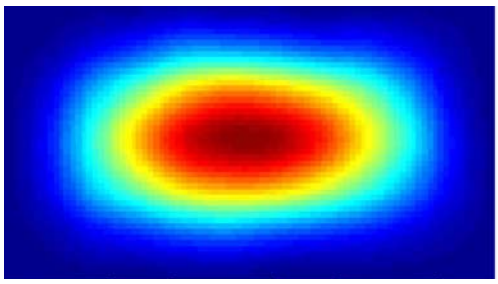

Mode (1,1) = 119 Hz

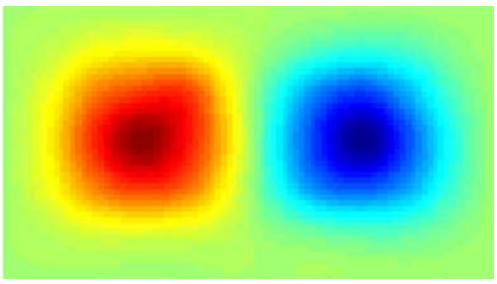

Mode (1,2) = 165 Hz

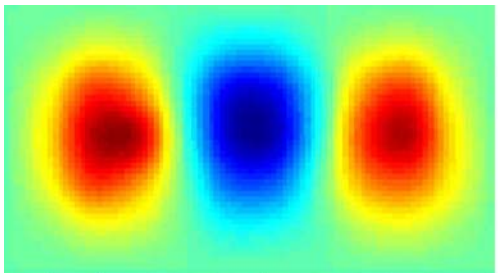

Mode (1,3) = 232 Hz

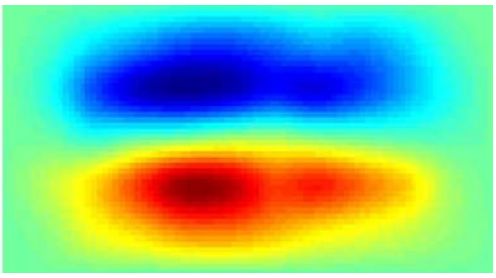

Mode (2,1) = 285 Hz

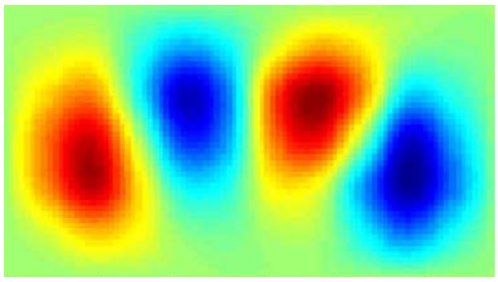

Mode (1,4) = 320 Hz

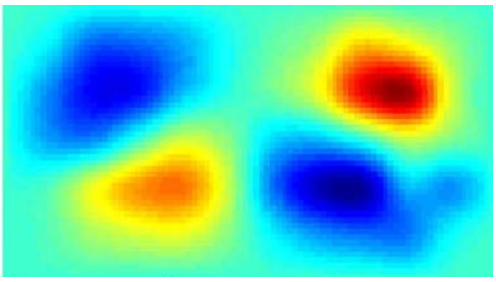

Mode (2,2) = 331 Hz

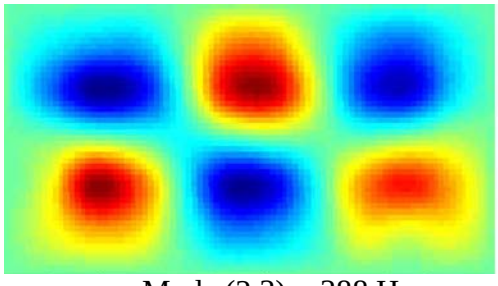

Mode (2,3) = 388 Hz

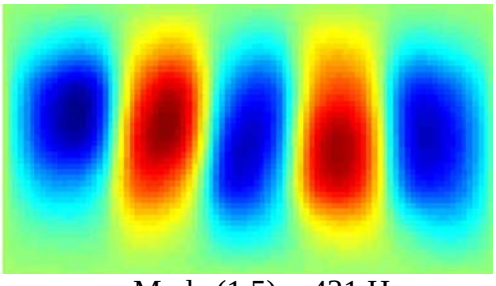

Mode (1,5) = 431 Hz

Figure A.3 Experimental mode shapes of VPI test panel: modes 1–8.

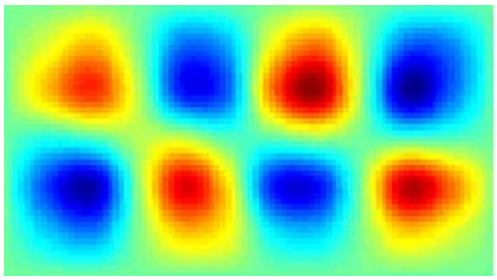

Mode (2,4) = 476 Hz

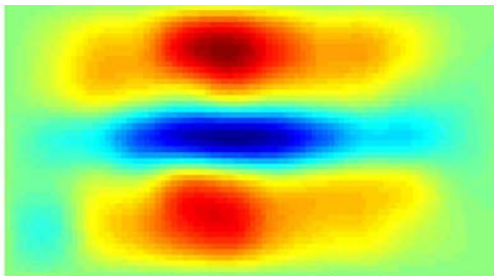

Mode (3,1) = 534 Hz

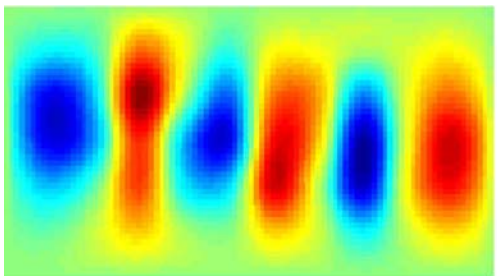

Mode (1,6) = 564 Hz

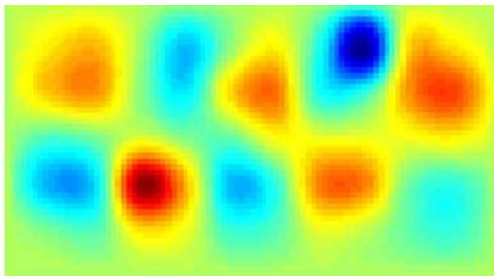

Mode (2,5) = 581 Hz

Figure A.4 Experimental mode shapes of VPI test panel: modes 9–12.

Vita

Jason R. Griffin was born on March 25, 1972 in an Army hospital in Alexandria, Virginia. Several years later he moved to Waynesboro, Virginia where he spent the rest of his childhood. Jason graduated in June of 1990 from Stuarts Draft High School and began his undergraduate studies that following August in Mechanical Engineering at Virginia Polytechnic Institute and State University. In December of 1994 he received his B.S. in Mechanical Engineering and began working temporarily at Litton Poly-scientific in Blacksburg, Virginia while his wife finished her degree. In August of 1995 Jason took a job in Colonial Heights, Virginia designing commercial refrigerated display cases for Hill PHOENIX. Two years later Jason returned to Virginia Polytechnic Institute and State University to begin his work on a Master of Science in Mechanical Engineering. Both years of graduate school were spent working in the Vibration and Acoustics Laboratories (VAL) under the direction of Dr. Chris R. Fuller. In August of 1999 Jason began work with Cummins Engine Company working as a Mechanical Development Engineer.